# Toward a Loophole-Free Bell Inequality Violation with Barium Ions

Carolyn Auchter

A dissertation
submitted in partial fulfillment of the
requirements for the degree of

Doctor of Philosophy

University of Washington

2016

Reading Committee:

Boris B. Blinov, Chair

Subhadeep Gupta

Xiaodong Xu

Program Authorized to Offer Degree:
Physics

University of Washington

**Abstract**

Toward a Loophole-Free Bell Inequality Violation with Barium Ions

Carolyn Auchter

Chair of the Supervisory Committee:
Professor Boris B. Blinov
Physics

The successful generation of ion-photon entanglement with a singly-trapped Barium ion and the photon it spontaneously emits is reported along with the current progress and technical details for extending this work to a loophole-free test of Bell's Inequality. The achieved ion-photon entanglement fidelity is .84(1) and a violation of the CHSH Bell Signal is shown to be greater than $8\sigma$. The utilization of a novel trap type and a pulsed laser for excitation is discussed for improvement of the rate of heralded ion-ion entanglement. A side project measuring the branching fraction of the $5D_{5/2}$ level in $^{138}Ba^{+}$ is also discussed.

# TABLE OF CONTENTS

# LIST OF FIGURES

# LIST OF TABLES

# ABBREVIATIONS

AOM: Acousto-Optic Modulator. An RF device in which light is Bragg scattered off of acoustic standing waves in a crystal in order to change the beam direction and frequency.

APD: Avalanche Photodiode. A semiconductor photon-counting device in which a single photon results in a high current through avalanche multiplication. They can have greater quantum efficiency, but also a greater total leakage current than PMTs.

ARP: Adiabatic Rapid Passage. A process through which population is transferred between states of a system with an avoided crossing by adiabatically varying a Hamiltonian that couples the two states.

BBO: Barium Borate ($BaB_2O_4$). A nonlinear optical crystal with birefringence that can be phase-matched for second harmonic generation.

CCD: Charge Coupled Device. A camera made from an array of photosensitive diodes which shift charge in order to capture images.

CHSH: Clauser-Horne-Shimony-Holt. A form of the Bell Inequality derived by said authors in which the statistics of the coincidences for a pair of measurements each made on a pair of particles is constrained.

DAC: Digital to Analog Converter. Takes an input digital signal and outputs an analog voltage proportional to the input value.

DDS: Direct Digital Synthesizer. An RF synthesizer operated by a DAC that can create programmed waveforms using a fixed frequency clock input.

ECDL: External Cavity Diode Laser. A laser in which an external cavity is added to reduce linewidth. This is typically formed with a diffraction grating to provide frequency control.

EMCCD: Electron Multiplied Charge-Coupled Device. A CCD in which charges produced by light are amplified.

FSR: Free Spectral Range. The frequency between longitudinal modes of an optical cavity. Equal to the speed of light divided by twice the cavity length.

FWHM: Full Width Half Maximum. A width measurement of a peak equal to the width between the heights at half the maximum on either side of the peak.

PBS: Polarizing Beam Splitter. An optical element which uses birefringent materials to split light into beams of orthogonal polarizations.

PDH: Pound-Drever-Hall. A laser locking technique in which the laser is phase modulated and the reflected signal from the cavity provides an error signal.

PMT: Photo-Multiplier Tube. A photo-sensitive device which uses the photoelectric effect to produce a free electron which cascades and thus amplifies into a measurable current signal.

PPLN: Periodically Poled Lithium Niobate. A crystal used for SHG in nonlinear optics. The crystal is periodically flipped which allows for a second harmonic wavelength matching the poling period to constructively interfere and thus increase in intensity.

RF: Radio Frequency. The part of the electromagnetic spectrum from 3 kHz to 300 GHz ranging from wavelengths of 1 mm to 100 km.

SHG: Second Harmonic Generation. A nonlinear optical process in which light is generated at twice the frequency of the input light.

TI:SAPPH: Titanium-doped Sapphire. An $Al_2O_3$ crystal doped with $Ti^{3+}$ ions which have a gain bandwidth from 600 nm to 1000 nm.

UHV: Ultra High Vacuum. A vacuum with pressures less than $10^{-9}$ Torr.

UV: Ultraviolet. The part of the electromagnetic spectrum just higher in frequency than visible light ranging from wavelengths of 400 nm to 10 nm.

VCO: Voltage Controlled Oscillator. A device which converts voltage to frequency whose output signal frequency is proportional to an input DC voltage.

# ACKNOWLEDGEMENTS

Firstly, I would like to thank Professor Boris Blinov for being such a great advisor and mentor in the lab. His advice was invaluable for my work, and I greatly appreciate his putting up with my writing process. My gratitude also extends to the other members of my reading committee, Professors Deep Gupta and Xiaodong Xu, and my supervisory committee, Professors Steven Sharpe and Peter Pauzauskie, for their comments and enthusiastic interest in my research.

Important thanks also go to the graduate students in Boris's group who were great labmates and always had helpful ideas and advice when I needed it. I am especially thankful to Thomas Noel with whom I worked closely in the lab and who was a great mentor to me when I first began experimental work. Thank you to Chen-Kuan Chou, John Wright, Matthew Hoffman, Spencer Williams, and Tomasz Sakrejda for their assistance in lab and friendship.

I am indebted to Catherine Provost, the Physics Program advisor, who was always there for me with advice about physics and life. I can't say enough how much I appreciate her open door and willingness to listen.

My wonderful friend, fellow physics student, and mentor, Tim Winchester was an important font of advice and information for me whenever I faced difficult decisions. His friendship, advice, and discussion of mutual struggles were irreplaceable.

Finally, everything I am today and all that I have accomplished, I owe to my parents, Tom and Edith Auchter. Their unwavering love, support, and advice has been and will continue to be a guiding force in my life. I am profoundly grateful to them for being such wonderful examples of generous, hardworking, inquisitive, and warmhearted people.

# Chapter 1

# IS QUANTUM MECHANICS A COMPLETE DESCRIPTION OF REALITY?

*[I can't accept quantum mechanics because] I like to think the moon is there even if I am not looking at it.*

- Albert Einstein

During the 19th and beginning of the 20th century, many experimental observations were made which could not be explained by classical physics. The theory of Quantum Mechanics was an incredible breakthrough developed by many of the most influential physicists of our time to explain and predict these effects. Its implications were revolutionary and still present many interesting questions today. While it quickly came to be widely accepted, it was not without debate as to its success as a descriptor of Nature.

## *1.1 Einstein-Podolsky-Rosen Paradox*

The development of Quantum Mechanics to explain physical phenomena in the early 1900s elicited many questions regarding its description of Nature. Uncomfortable with the inherent indeterminism of the theory, Einstein, Podolsky, and Rosen most famously challenged the completeness of the theory in a 1935 paper commonly referred to as the EPR Paradox [14]. The authors asserted that a complete description of reality must contain elements corresponding to every physical observable that allow one to predict with certainty the value

of that observable. Because the physical observables associated with non-commuting operators cannot be measured or known at the same instance in time, either the description could not be complete or the physical quantities of such operators could not exist simultaneously. Through a thought experiment assuming that Quantum Mechanics was complete, the authors arrived at the result that those physical quantities should exist simultaneously. Thus they posited that there must be some hidden variables unknown to experimenters that completely determine the state of the system.

The authors proceed with their thought experiment by assuming two interacting systems, I and II, both with known states before such interaction begins, whose interaction lasts from t=0 to t=T. The resultant two system state is what is now termed an entangled state, that is, one "can then calculate with the help of Schrodinger's equation the state of the combined system I + II at any subsequent time; in particular, for any $t > T$. Let us designate the corresponding wave function by $\Psi$. We cannot, however, calculate the state in which either one of the two systems is left after the interaction." [14].

While the authors used momentum and position operators, let us use the spin-1/2 operators in explaining their argument. It may be useful for the reader to recall that in a spin-1/2 system, the x, y, or z-component of the spin of a particle can take on only two values, $\pm\hbar/2$. Thus in the z-basis, the spin operators are as follows

$$S_z = \frac{\hbar}{2}\begin{bmatrix} 1 & 0 \\ 0 & -1 \end{bmatrix}, \quad S_x = \frac{\hbar}{2}\begin{bmatrix} 0 & 1 \\ 1 & 0 \end{bmatrix}, \quad S_y = \frac{\hbar}{2}\begin{bmatrix} 0 & -i \\ i & 0 \end{bmatrix} \tag{1.1}$$

and $|\pm_z\rangle$ are the states corresponding to a spin in the z-direction of $\pm\hbar/2$ respectively. With some algebra, one may find that $|\pm_x\rangle = \frac{1}{\sqrt{2}}(|+_z\rangle \pm |-_z\rangle)$. So, taking the following two-system state in the z-basis:

$$\Psi = \frac{1}{\sqrt{2}}(|+_z\rangle_1|-_z\rangle_2 + |-_z\rangle_1|+_z\rangle_2) \tag{1.2}$$

the state would be written as follows in the x-basis:

$$\Psi = \frac{1}{\sqrt{2}}(|+_x\rangle_1|+_x\rangle_2 - |-_x\rangle_1|-_x\rangle_2) \tag{1.3}$$

If one were to measure the operator $S_{1z}$ and obtain $+\frac{\hbar}{2}$, this would imply that the second particle was in the state $|-_z\rangle_2$. Similarly, if one were to measure the operator $S_{1x}$ and obtain $+\frac{\hbar}{2}$, this would imply that the second particle was in the state $|+_x\rangle_2$. The authors reasoned that since the particles were not interacting after time T, any measurement on system 1 could not cause any real change in system 2. Thus the states $|-_z\rangle_2$ and $|+_x\rangle_2$ would be assigned to the same reality. Hence, even though $S_{1z}$ and $S_{1x}$ are non-commuting operators, the physical observables pertaining to those operators exist simultaneously. This apparent contradiction led the authors to conclude that Quantum Mechanics could not be a complete description of Nature. The authors did concede that there was a possible flaw with their criterion for reality, however asserted that any definition of reality causing the observable of the second system to depend on measurement upon the first system with which it is not interacting is absurd: "No reasonable definition of reality could be expected to permit this." [14]. Einstein, Podolsky, and Rosen believed that a more fundamental local hidden variable theory must exist with additional predictive power.

### *1.2 Bell Inequality*

For almost thirty years, the EPR Paradox remained unchallenged experimentally. However in 1964, physicist John Bell wrote a paper demonstrating the existence of an experimental test that could refute all such local hidden variable theories in one fell swoop: "It is the requirement of locality, or more precisely that the result of a measurement on one system be unaffected by operations on a distant system with which it has interacted in the past, that creates the essential difficulty." [2]. Bell proved that any local hidden variable theory must obey an inequality that would be violated by certain highly entangled quantum states. The states that maximally violated that inequality and which were used by Bell in his proof have

come to be known as the Bell states:

$$|\Phi^+\rangle = \frac{1}{\sqrt{2}}(|+\rangle_1|+\rangle_2 + |-\rangle_1|-\rangle_2) \tag{1.4}$$

$$|\Phi^-\rangle = \frac{1}{\sqrt{2}}(|+\rangle_1|+\rangle_2 - |-\rangle_1|-\rangle_2) \tag{1.5}$$

$$|\Psi^+\rangle = \frac{1}{\sqrt{2}}(|+\rangle_1|-\rangle_2 + |-\rangle_1|+\rangle_2) \tag{1.6}$$

$$|\Psi^-\rangle = \frac{1}{\sqrt{2}}(|+\rangle_1|-\rangle_2 - |-\rangle_1|+\rangle_2) \tag{1.7}$$

Beginning with a spin singlet state 1.7, Bell endeavored to show that the expectation value of the product of spin measurements in random directions on each particle derived using a hidden variable theory would not be equivalent to the quantum mechanical expectation value. He concluded that the assumption made by EPR, that the measurement of the second system could not depend on a measurement of the first system, was incompatible with the predictions of Quantum Mechanics. Moreover such influence had to occur instantaneously with the first measurement.

### *1.3 CHSH Inequality*

In 1969, physicists Clauser, Horne, Shimony, and Holt (CHSH) generalized Bell's result beyond its application to only spin singlet states to any spin state. [11]. They considered a statistical ensemble of correlated pairs, of which each particle was measured by a separate measurement apparatus, $\mathrm{I}_a$ or $\mathrm{II}_b$, with adjustable parameters $a$ and $b$ respectively. The possible results of the measurements, represented by $A(a)$ and $B(b)$, are +1 and -1, as one would expect from the normalized results of a spin-1/2 measurement. Assuming local realism (*i.e.* there exist some hidden variables denoted by $\lambda$ which determine the distribution of the particles among the measurable values), the results can be determined by $A(a, \lambda)$ and $B(b, \lambda)$. A probability distribution $\rho(\lambda)$ characterizes the ensemble as a whole. As the ensemble is generated independently of the measurement parameters, $\rho(\lambda)$ is assumed to be

independent of $a$ and $b$. Likewise, since the apparatuses may be remote from one another, the measurement result of the first apparatus is assumed independent of the parameter setting of the second and vice versa.

One can define a correlation function, the average of the product of the two particle measurements for every pair in the ensemble, as follows:

$$P(a,b) = \int_{\Lambda} A(a,\lambda)B(b,\lambda)\rho(\lambda)d\lambda \tag{1.8}$$

where $\Lambda$ is the total $\lambda$ space. Thus, due to the triangle inequality,

$$\begin{aligned} |P(a,b) - P(a,c)| &= |\int_{\Lambda} \{A(a,\lambda)B(b,\lambda) - A(a,\lambda)B(c,\lambda)\}d\lambda| \\ &\leq \int_{\Lambda} |A(a,\lambda)B(b,\lambda) - A(a,\lambda)B(c,\lambda)|d\lambda \\ &= \int_{\Lambda} |A(a,\lambda)B(b,\lambda) - A(a,\lambda)B^2(b,\lambda)B(c,\lambda)|d\lambda \\ &= \int_{\Lambda} |A(a,\lambda)B(b,\lambda)|(1 - B(b,\lambda)B(c,\lambda))d\lambda \\ &= \int_{\Lambda} (1 - B(b,\lambda)B(c,\lambda))d\lambda \\ &= 1 - \int_{\Lambda} B(b,\lambda)B(c,\lambda)d\lambda \end{aligned} \tag{1.9}$$

since all measurements have values of $\pm 1$ and the probability distribution is normalized.

Next the authors assume that $P(b',b) = 1 - \delta$ for some $b'$ and $b$, where $0 \leq \delta \leq 1$. This avoids the restriction in Bell's derivation that the particles are perfectly correlated. The space of hidden variables $\Lambda$ may be divided into regions based on correlation, $\Lambda_+$, or

anticorrelation, $\Lambda_-$, such that $\Lambda_\pm = \{\lambda | A(b',\lambda) = \pm B(b,\lambda)\}$. Then,

$$\begin{aligned}
P(b',b) &= \int_\Lambda A(b',\lambda)B(b,\lambda)\rho(\lambda)d\lambda \\
&= \int_{\Lambda_+} A(b',\lambda)B(b,\lambda)\rho(\lambda)d\lambda - \int_{\Lambda_-} A(b',\lambda)B(b,\lambda)\rho(\lambda)d\lambda + 2\int_{\Lambda_-} A(b',\lambda)B(b,\lambda)\rho(\lambda)d\lambda \\
&= \int_{\Lambda_+} \rho(\lambda)d\lambda - \int_{\Lambda_-} -\rho(\lambda)d\lambda + 2\int_{\Lambda_-} -\rho(\lambda)d\lambda \\
&= \int_{\Lambda_+} \rho(\lambda)d\lambda + \int_{\Lambda_-} \rho(\lambda)d\lambda - 2\int_{\Lambda_-} \rho(\lambda)d\lambda \\
&= \int_{\Lambda} \rho(\lambda)d\lambda - 2\int_{\Lambda_-} \rho(\lambda)d\lambda \\
&= 1 - 2\int_{\Lambda_-} \rho(\lambda)d\lambda
\end{aligned} \tag{1.10}$$

Thus

$$\int_{\Lambda_-} \rho(\lambda)d\lambda = \frac{\delta}{2} \tag{1.11}$$

Next, one may manipulate part of the result from Eq. 1.9, to find,

$$\begin{aligned}
\int_\Lambda B(b,\lambda)B(c,\lambda)d\lambda &= \int_{\Lambda_+} B(b,\lambda)B(c,\lambda)d\lambda + \int_{\Lambda_-} B(b,\lambda)B(c,\lambda)d\lambda \\
&= \int_{\Lambda_+} A(b',\lambda)B(c,\lambda)\rho(\lambda)d\lambda + \int_{\Lambda_-} -A(b',\lambda)B(c,\lambda)\rho(\lambda)d\lambda \\
&= \int_{\Lambda} A(b',\lambda)B(c,\lambda)\rho(\lambda)d\lambda - 2\int_{\Lambda_-} A(b',\lambda)B(c,\lambda)\rho(\lambda)d\lambda \\
&= P(b',c) - 2\int_{\Lambda_-} A(b',\lambda)B(c,\lambda)\rho(\lambda)d\lambda \\
&\leq P(b',c) - 2\int_{\Lambda_-} |A(b',\lambda)B(c,\lambda)|\rho(\lambda)d\lambda \\
&= P(b',c) - 2\int_{\Lambda_-} \rho(\lambda)d\lambda \\
&= P(b',c) - \delta
\end{aligned} \tag{1.12}$$

Thus, combining Eqs. 1.9-1.12 one finds the CHSH inequality,

$$|P(a,b)-P(a,c)| \leq 1-P(b',c)+\delta = 1-P(b',c)+1-P(b',b) = 2-P(b',b)-P(b',c) \quad (1.13)$$

or

$$S(a,b';b,c) \equiv |P(a,b)-P(a,c)| + P(b',b) + P(b',c) \leq 2 \quad (1.14)$$

for correlations between measurements, each set at two different parameters, on a pair of particles in any local hidden variable theory.

We can derive that this inequality is violated for certain quantum mechanical states. The correlation function $P(a,b)$ may be defined in terms of an expectation value of the product of the two measurements on each particle in the pair. That is,

$$P(a,b) = \langle \Psi_{1,2} | A \cdot B | \Psi_{1,2} \rangle \quad (1.15)$$

Consider again one of the Bell States, $\Psi^+$, described by Eqs. 1.2 and 1.6. Let $A$ and $B$ be spin measurements rotated from $S_z$ by the angles $\theta = a$ and $\theta = b$ respectively. Eq. 1.15 becomes

$$P(a,b) = \langle \Psi^+ | U_1^\dagger(a) S_{1z} U_1(a) U_2^\dagger(b) S_{2z} U_2(b) | \Psi^+ \rangle = -\cos(a+b) \quad (1.16)$$

where $U_i(\theta)$ is a unitary rotation operator. Thus, the Bell Signal for $\Psi^+$ is

$$S_{\Psi^+}(a,b';b,c) = |-\cos(a+b)+\cos(a+c)| - \cos(b'+b) - \cos(b'+c) \quad (1.17)$$

Setting $a = 0$, the Bell Signal for $\Psi^+$ is maximized when $b' = \pi/2$, $b = \pi/4$, and $c = 3\pi/4$ such that $S_{\Psi^+}(0,\pi/2;\pi/4,3\pi/4) = 2\sqrt{2}$, clearly violating the limit (Eq. 1.14) set for local realistic hidden variable theories.

### *1.4 Loopholes and a Loophole-free Test*

Since their development, many experiments in numerous physical systems have confirmed that nature violates the Bell and CHSH Inequalities. [58, 43, 17, 30, 56, 1, 23, 57]. Many have been subject though to at least one so called loophole. There are two major loopholes that may be closed by experimental tests involving ions. To date, both major loopholes have only been closed in a photon system [18, 47] and NV centers in diamond [24].

The first loophole is the detection, or fair-sampling, loophole. Because detection and measurement of quantum particles may not be 100 percent efficient, it is possible that the correlations observed may mimic results predicted by Quantum Mechanics due to some unknown interaction with the measurement devices. Another way of stating this is because one does not measure the entire sample of events due to detection inefficiency, the portion measured may not be representative of the sample as a whole and be skewed for some unknown reason. Since ions can reach very high detection efficiency levels ($\geq$ .95), an experiment with two entangled ions is capable of beating the fair-sampling loophole.

The second loophole is the communication, or locality, loophole. The EPR assumption of locality, that measurement of the first particle will not affect the state of the second particle, can be achieved by prohibiting any possible light-speed communication between the respective measurements. Thus if the particles are separated by distances longer than that determined by the measurement duration, the locality loophole will be closed.

To achieve such a distance with a pair of entangled ions in order to perform a loophole-free test of Bell's inequalities, Simon and Irvine proposed an experiment involving a heralded remote entanglement swapping scheme in 2003 [48]. There are three experimental steps:

1. An ion and photon pair are entangled at each measurement site, separated by several kilometers.

2. The photons are collected and transmitted to a beam splitter where joint detection of the two photons realizes a partial Bell state analysis.

3. Measurement of the ion states confirms entanglement and demonstrates a violation of Bell's inequalities.

The first and third step are discussed in greater detail for our system in Chapters 8 and 9. Briefly, the first step is achieved by initializing and exciting the ion to a known excited state from which there are decay paths to two degenerate metastable or stable states. The emitted photon will thus be entangled with the final state of the ion. Take for example, the resultant entangled ion-photon state to be

$$\Psi_{ion-photon} = \frac{1}{\sqrt{2}}(|s_1, p_1\rangle + |s_2, p_2\rangle) \tag{1.18}$$

where $s_1$ and $s_2$ are the final states of the ion and $p_1$ and $p_2$ are the polarizations of the emitted photon. The total state of both entangled ion-photon pairs may be written as

$$\Psi = \frac{1}{2}(|s_1, p_1\rangle + |s_2, p_2\rangle)_I(|s_1, p_1\rangle + |s_2, p_2\rangle)_{II} \tag{1.19}$$

where I indicates the state of the first ion-photon pair system and II indicates the state of the second ion-photon system. This state may be written in the Bell bases for the ion pair and the photon pair as

$$\Psi = \frac{1}{2}(\Phi^+_{ion-ion}\Phi^+_{photon-photon}+\Phi^-_{ion-ion}\Phi^-_{photon-photon}+\Psi^+_{ion-ion}\Psi^+_{photon-photon}+\Psi^-_{ion-ion}\Psi^-_{photon-photon}) \tag{1.20}$$

where

$$\Phi^+_{ion-ion} = \frac{1}{\sqrt{2}}(|s_1, s_1\rangle + |s_2, s_2\rangle) \tag{1.21}$$

$$\Phi^+_{photon-photon} = \frac{1}{\sqrt{2}}(|p_1, p_1\rangle + |p_2, p_2\rangle) \tag{1.22}$$

and similarly for the remaining Bell States. This form will be useful for the analysis done in the second step.

A diagram illustrating the second step appears in Fig. 1.1. When two photons are incident on separate input ports of a 50/50 beam splitter, coincident detections at the separate output ports are possible if the photons are both transmitted or both reflected. Due to the extra phase each photon acquires on reflection, the photons will only be emitted from each output port if they are initially in an antisymmetric spatial state. As photons are bosons, this implies the polarization state, entangled with each ion, must also be in an antisymmetric state, or $\Psi^-_{photon-photon}$. In this manner, a coincident detection heralds the creation of the antisymmetric $\Psi^-_{ion-ion}$ Bell state for the ion pair. Measurement of the ion state is achieved with the shelving techniques and state rotations described in Chapter 6.

There are also several requirements regarding measurement that must be met to ensure the closure of the locality loophole:

1. The choice of ion measurement basis must be chosen randomly and no information about that choice should be able to affect a similar choice at the second site through a speed of light transmission.

2. The choice of ion measurement basis must not be able to affect the ion measurement at the second site through a speed of light transmission.

3. The choice of ion measurement basis must not be able to affect the joint detection of the photons through a speed of light transmission.

These requirements are illustrated and discussed in a space-time diagram in Fig. 1.2

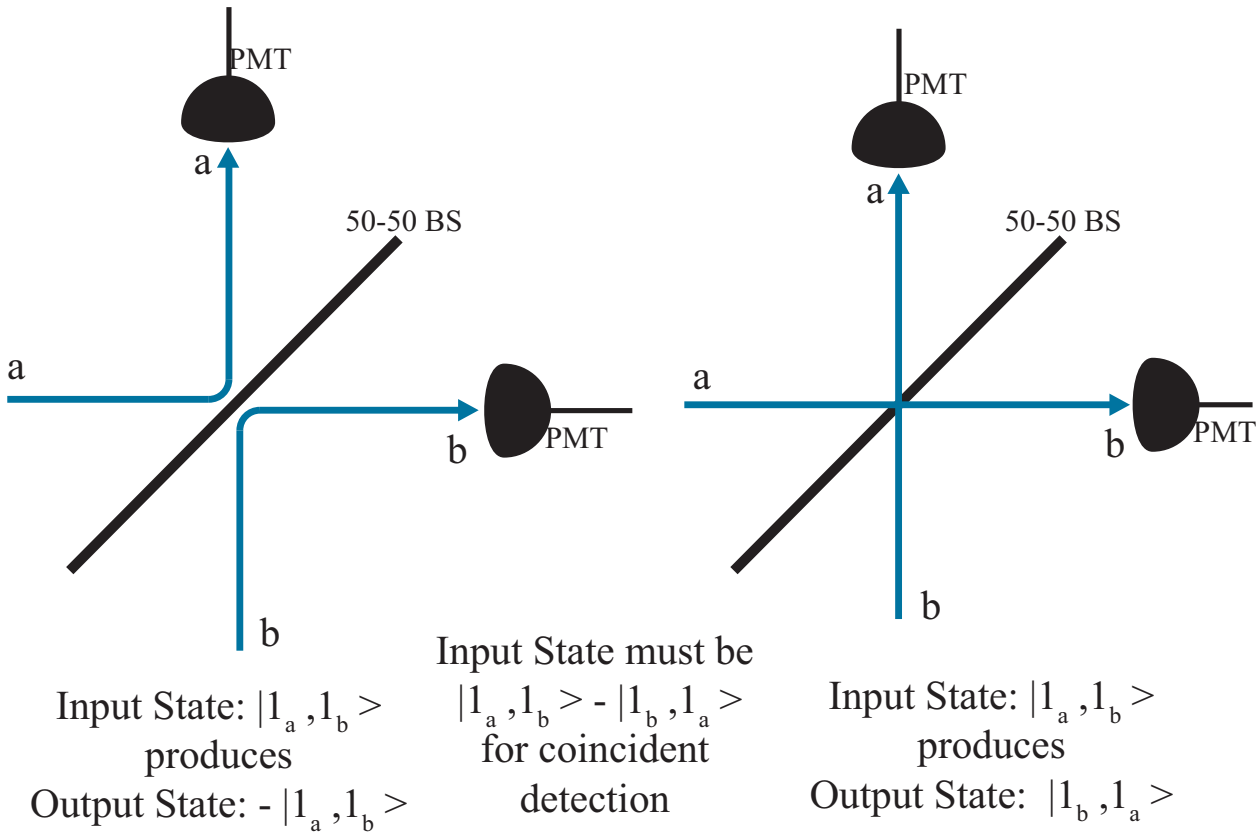


Figure 1.1: Two photons, one incident on each input port, will produce two photons, one at each output port, with an extra phase of $\pi$ when reflected as shown on the left. Two photons, one incident on each input port, will produce two photons, one at each output port, without the extra phase as shown on the right. Thus a spatially antisymmetric input state results in a coincident detection: $\frac{1}{\sqrt{2}}(|1_a, 1_b\rangle - |1_b, 1_a\rangle) \rightarrow \frac{1}{\sqrt{2}}\frac{1}{2}((-|1_a, 1_b\rangle + |1_b, 1_a\rangle) - (-|1_b, 1_a\rangle + |1_a, 1_b\rangle)) = -\frac{1}{\sqrt{2}}(|1_a, 1_b\rangle - |1_b, 1_a\rangle)$, whereas a spatially symmetric input state will interfere destructively, thus resulting in no coincident detection: $\frac{1}{\sqrt{2}}(|1_a, 1_b\rangle + |1_b, 1_a\rangle) \rightarrow \frac{1}{\sqrt{2}}\frac{1}{2}((-|1_a, 1_b\rangle + |1_b, 1_a\rangle) + (-|1_b, 1_a\rangle + |1_a, 1_b\rangle)) = 0$.

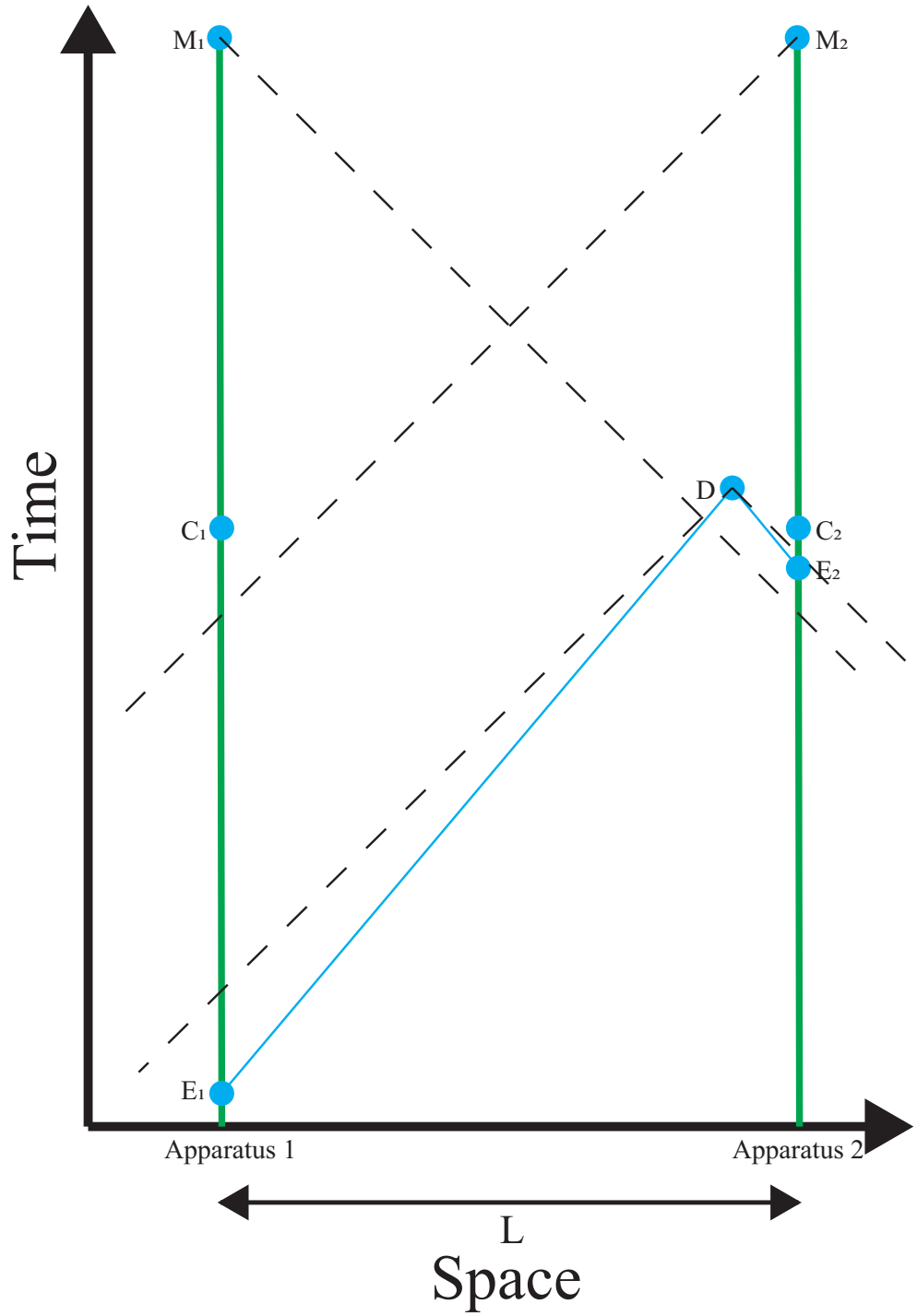


Figure 1.2: A space-time diagram depicting the world lines of the two apparatus and the ion-photon entanglement events ($E_1$, $E_2$), the choice of ion measurement bases ($C_1$, $C_2$), the joint photon detection heralding entanglement of the ions (D), and the measurement of each ion ($M_1$, $M_2$). As can be seen from the diagram, $C_1$ and $C_2$ lie outside the backwards light cones of D and $M_2$ and $M_1$ respectively as required to close the locality loophole. L is the distance between the two measurement sites.

Chapter 2

# WHAT DETERMINES THE ENERGY STRUCTURE OF AN ATOM AND HOW DOES IT INTERACT WITH EXTERNAL FIELDS?

*A careful analysis of the process of observation in atomic physics has shown that the subatomic particles have no meaning as isolated entities, but can only be understood as interconnections between the preparation of an experiment and the subsequent measurement.*

- Erwin Schrödinger

In order to design and implement an experimental test of the form discussed in Ch. 1, one must understand the atomic structure and how to manipulate an ion using external fields in order to achieve the desired measurements. This chapter will detail those parts of atomic theory important to such an understanding.

## *2.1 Atomic Structure*

To determine atomic structure, one can begin by examining the hydrogen atom. Due to the simple Coulomb interaction between a single proton and a single electron, the Schrödinger equation may be solved analytically in order to determine a total wavefunction consisting of

radial and angular parts.

$$\{\frac{-\hbar^2}{2m_e}\nabla^2 + V(r)\}\psi = E\psi \quad ; \quad V(r) = \frac{-e^2}{4\pi\epsilon_0 r} \tag{2.1}$$

$$\psi(r,\theta,\phi) = R_{n,l}(r)Y_{l,m}(\theta,\phi) \tag{2.2}$$

$$E = -\frac{(e^2/4\pi\epsilon_0)^2 m_e}{2\hbar^2}\frac{1}{n^2} \tag{2.3}$$

where $\hbar$ is the reduced Planck constant, $m_e$ is the mass of the electron, $e$ is the electron charge, and $\epsilon_0$ is the permittivity of free space. Due to the spherical symmetry of the Coulomb potential, the energy levels only depend on the principal quantum number $n$. The radial and angular wavefunctions are of the form

$$R_{n,l}(r) = \sqrt{\left(\frac{2}{na_0}\right)^3 \frac{(n-l-1)!}{2n[(n+l)!]}} e^{-\frac{r}{na_0}} \left(\frac{2r}{na_0}\right)^l L^{2l+1}_{n-l-1}\left(\frac{2r}{na_0}\right) \tag{2.4}$$

$$Y_{l,m}(\theta,\phi) = \sqrt{\frac{(2l+1)}{4\pi}\frac{(l-m)!}{(l+m)!}} P_l^m(\cos\theta)e^{im\phi} \tag{2.5}$$

where $L^{2l+1}_{n-l-1}$ is a generalized Laguerre polynomial of degree $n-l-1$, $P_l^m$ is an associate Legendre polynomial, $a_0$ is the Bohr radius, and $n$, $l$, and $m$ are the quantum numbers corresponding to energy level, orbital angular momentum, and its component along the z-axis.

For multi-electron atoms or ions, such as $^{138}Ba^+$, the Schrödinger equation cannot be solved analytically, but with approximations, one can achieve a good picture of what occurs at the atomic level. The $^{138}Ba^+$ ion has a single valence electron, making it simple to describe the ion as a single unpaired electron outside a core of closed electronic sub-shells. Unlike the single electron in hydrogen however, the angular wavefunction for the valence electron of $^{138}Ba^+$ experiences shifts in the energy level due to shielding of the nucleus to different extents for different orbitals by the core of closed sub-shells. It is clear from viewing several

different orbitals in Fig. 2.1 that this is the case as some orbitals have a greater probability density close to nucleus and thus are less shielded from the nuclear charge by the inner core of electrons.

In addition to the energy shifts due to electron shielding of orbitals, the single valence electron has spin, $s$, which results in additional shifts due to spin-orbit coupling. This is known as the fine structure of the atom. Because the valence electron is moving through a radial electric field, relativity implies that the electron experiences an effective magnetic field proportional to the angular momentum. This is because the magnetic field is proportional to the cross product of the electron's velocity with the radial electric field. The interaction of the magnetic field with the electron's intrinsic magnetic moment due to its spin thus gives the Hamiltonian:

$$H_{s-o} = (g_s - 1)\frac{\hbar^2}{2m_e^2c^2}(\frac{1}{r}\frac{\partial V}{\partial r})\ \mathbf{s}\cdot\mathbf{l} \tag{2.6}$$

where $g_s$ is the electron spin g-factor, $\hbar$ is the reduced Planck constant, $m_e$ is the mass of the electron, $c$ is the speed of light, and $\mathbf{s}$ and $\mathbf{l}$ are the spin and angular momentum operators respectively.

In order to determine how an interaction that has the form of $\mathbf{s}\cdot\mathbf{l}$ alters the structure, one can introduce the total angular momentum as the sum of the orbital and spin angular momenta:

$$\mathbf{j} = \mathbf{l} + \mathbf{s} \tag{2.7}$$

where $j$ takes values from $l + s$ to $|l - s|$ in integer steps. By squaring and rearranging Eq. 2.7, one finds:

$$\mathbf{s}\cdot\mathbf{l} = \frac{1}{2}(\mathbf{j}^2 - \mathbf{l}^2 - \mathbf{s}^2) \tag{2.8}$$

Thus the energy eigenstates of the hamiltonian (Eq. 2.6) are those of $\mathbf{j}^2$, $\mathbf{l}^2$, and $\mathbf{s}^2$, which are labeled by $j$, $l$, and $s$, and whose energies are:

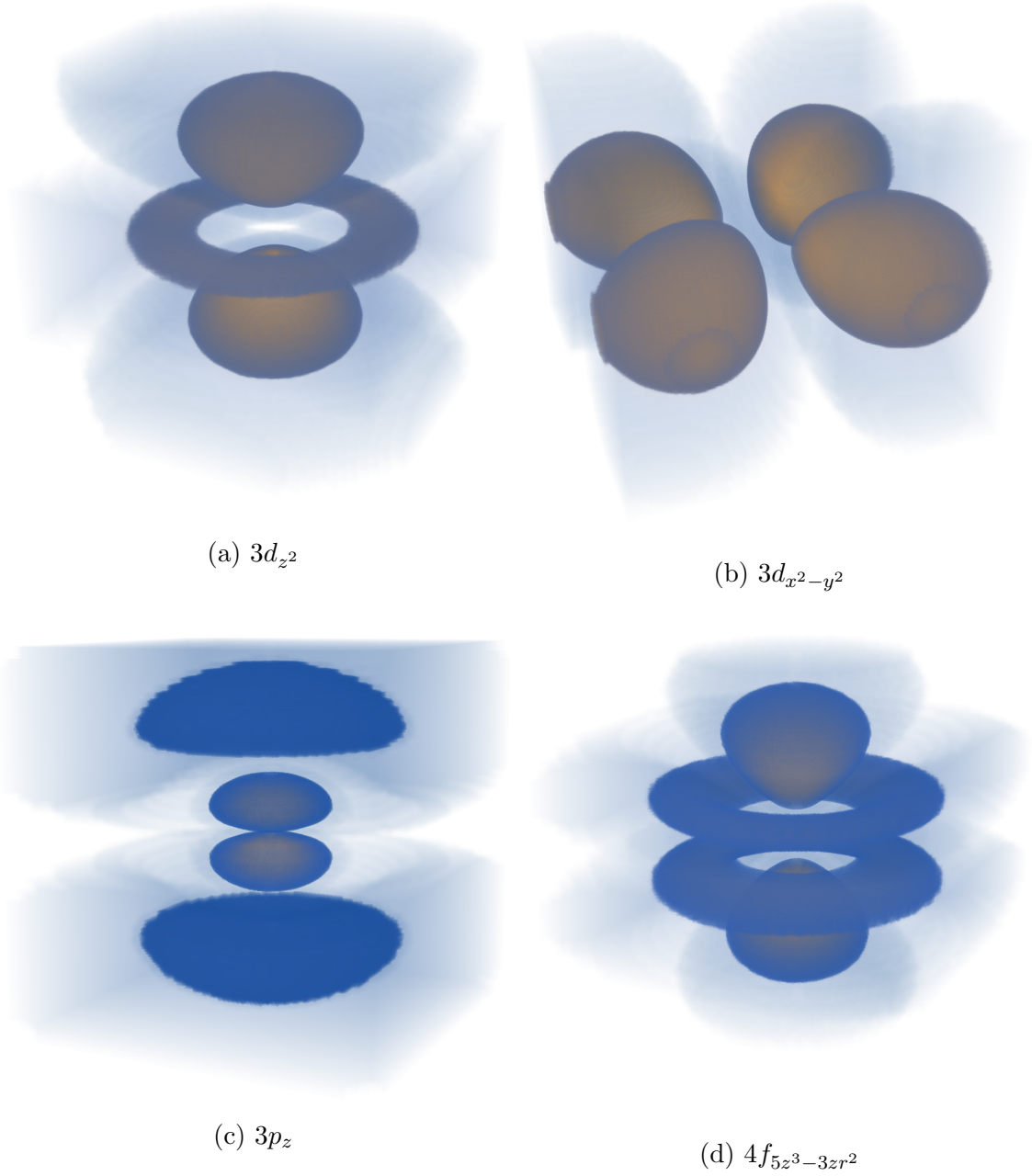

(a) $3d_{z^2}$

(b) $3d_{x^2-y^2}$

(c) $3p_z$

(d) $4f_{5z^3-3zr^2}$

Figure 2.1: Four different angular wavefunctions of the hydrogen atom. One may observe the different extent to which the electron probability density is distributed around the nucleus. For an atom or ion with a single valence electron outside an inner core of closed electronic sub-shells, those angular wavefunctions with greater electron probability density close to the nucleus will have lower energies. Note that the vertical scale is compressed by a factor of 1.5 and the entire diagram of the $4f_{5z^3-3zr^2}$ is scaled down by a factor of 2

$$E_{s-o} \propto \frac{1}{2}\{j(j+1) - l(l+1) - s(s+1)\} \tag{2.9}$$

Because eigenstates can be labeled by $j$, $l$, and $s$, one can introduce a method of state labeling using term symbols of the form $n^{2s+1}\mathrm{L}_j$ where $n$ is the principal quantum number. Since $s = \frac{1}{2}$ for our $^{138}\mathrm{Ba}^+$ ion, this is generally dropped to make the symbol $n\mathrm{L}_j$ such as $6\mathrm{S}_{1/2}$, the ground state of $^{138}\mathrm{Ba}^+$. In addition to electron spin, many atoms also have nuclear spin $\mathbf{I}$. Similarly to how electron spin produces fine structure, the nuclear spin produces hyperfine structure. As $^{138}\mathrm{Ba}^+$ does not have nuclear spin, we will not concern ourselves with this derivation. The structure of $^{138}\mathrm{Ba}^+$ along with the relevant energy splittings from the $6\mathrm{S}_{1/2}$ ground state are depicted in Fig. 2.2. As one will see, the breaking of degeneracy of the hydrogenic energy levels is highly useful for manipulation and detection of the ion state.

## *2.2 The Zeeman Effect*

As above, splitting the degeneracy of the energy levels is quite useful for the manipulation and detection of the ion state. For these purposes, it is of further use to separate the $2j+1$ degenerate $m_j$ states for given $j$, $l$, and $s$ ($m_j$, similarly to $m_l$ and $m_s$, ranges from $-j$ to $j$ in integer steps). In order to separate these degenerate states, the ion may be placed in a small uniform magnetic field. The ion has a magnetic moment proportional to the total angular momentum, $\mathbf{j}$. The interaction of this magnetic moment with an external magnetic field results in the Hamiltonian

$$H_{ZE} = -\boldsymbol{\mu}\cdot\mathbf{B} = -\mu_B g_j \mathbf{j}\cdot\mathbf{B} = -\mu_B g_j B j_z \tag{2.10}$$

taking $\mathbf{B} = B\hat{\mathbf{z}}$ specifying the quantization axis and where $\mu_B$ is the Bohr magneton and $g_j$ is the Landé $g$-factor. As long as $E_{ZE} \ll E_{s-o}$, this interaction can be treated as a perturbation to the spin-orbit levels. Thus, $E_{ZE} = -\mu_B g_j B m_j$. The energy shift versus magnetic field is plotted in Fig. 2.3 for the $6\mathrm{S}_{1/2}$ ground state and the $5\mathrm{D}_{5/2}$ excited state of $^{138}\mathrm{Ba}^+$.

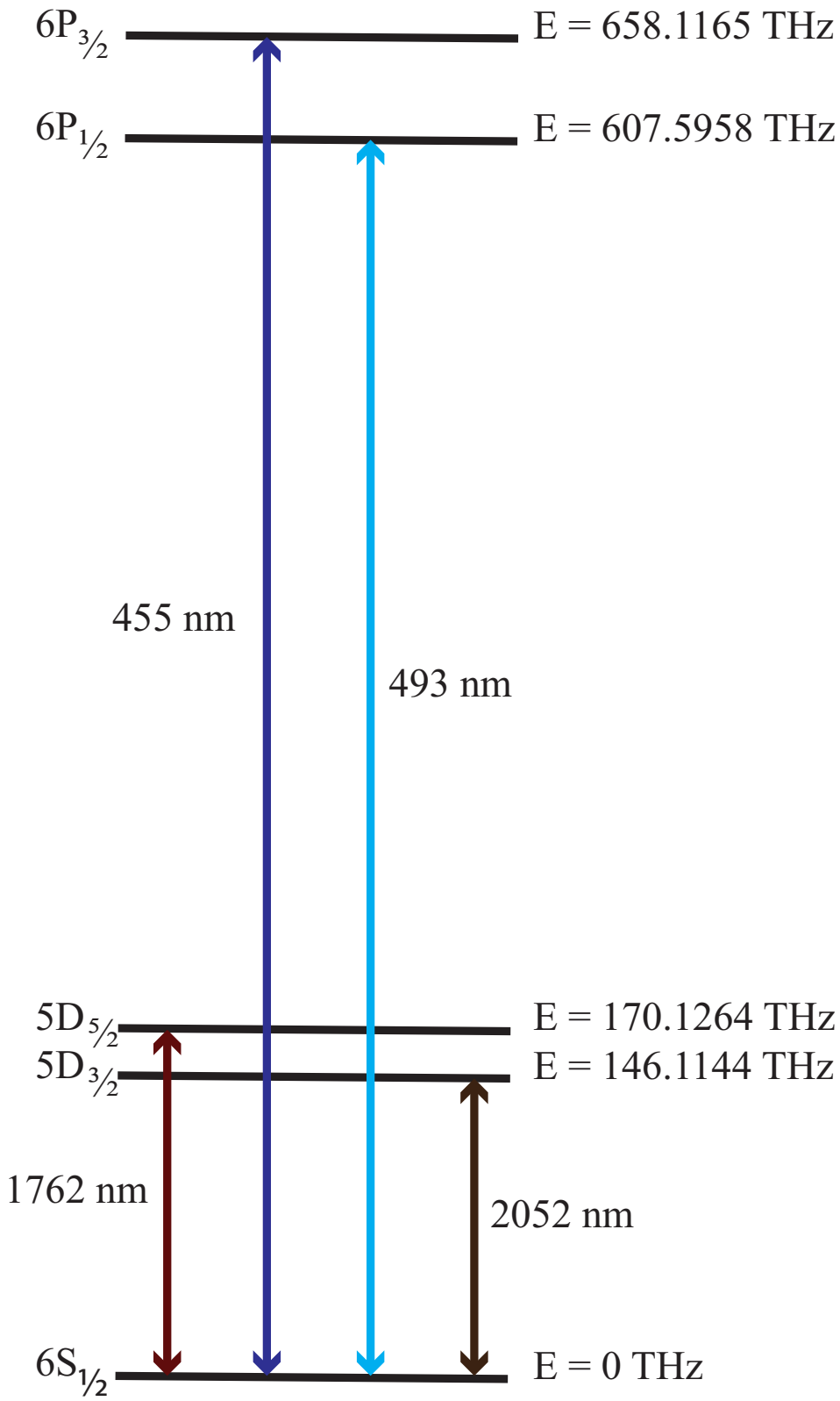


Figure 2.2: The structure of $^{138}Ba^{+}$ with energy differences in units of THz and transition wavelengths from the $6S_{1/2}$ ground state.

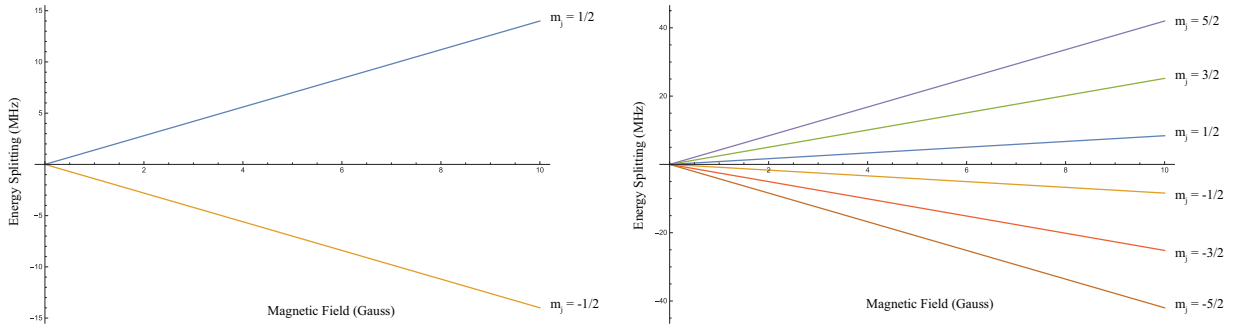


(a) $6S_{1/2}$ (b) $5D_{5/2}$

Figure 2.3: The frequency splitting for the $6S_{1/2}$ ground state for each projection of the total angular momentum on the quantization axis, $m_j$, is shown on the left, and the frequency splitting for the $5D_{5/2}$ excited state is shown on the right. For the $6S_{1/2}$ ground state, $g_j \approx 2$, and for the $5D_{5/2}$ excited state, $g_j \approx 1.2$. Note that the vertical scales differ.

## *2.3 Interactions with Oscillating Electric and Magnetic Fields*

Now that one understands how to determine the basic atomic level structure, it is useful to determine how interactions with oscillating fields affect transitions between two of such states. The Hamiltonian is now described by an interaction part, $H_I$, in addition to the unperturbed hamiltonian $H_0$ that determines the energy eigenstates of the atom:

$$H = H_0 + H_I \tag{2.11}$$

For transitions between two states, we can determine how the coefficients in a superposition of those two states change in time due to the interaction part of the Hamiltonian. Take

$$\Psi(t) = c_1(t)\psi_1 e^{-iE_1 t/\hbar} + c_2(t)\psi_2 e^{-iE_2 t/\hbar} = c_1 e^{-i\omega_1 t}|1\rangle + c_2 e^{-i\omega_2 t}|2\rangle \tag{2.12}$$

where

$$|c_1|^2 + |c_2|^2 = 1 \tag{2.13}$$

due to normalization of the state, and

$$\begin{aligned} H_0\psi_1 &= E_1\psi_1 \\ H_0\psi_2 &= E_2\psi_2 \end{aligned} \tag{2.14}$$

The interaction Hamiltonian may be described with an oscillating electric or magnetic field. Let us begin with the simple picture of an oscillating electric field of electromagnetic radiation linearly polarized along the x-axis interacting with the electric dipole ($e\mathbf{r}$) of an atom:

$$H_I(t) = e\mathbf{r}\cdot\mathbf{E}_0\cos(\omega t) = eE_0\cos(\omega t)\mathbf{r}\cdot\hat{\mathbf{x}} = eE_0 x\cos(\omega t) \tag{2.15}$$

where the magnitude $E_0$ of the electric field is roughly constant over the extent of the atomic wavefunction since the wavelength of the radiation is much greater than the size of the atom. Substituting Eq. 2.12 into the time-dependent Schödinger equation, one finds,

$$\begin{aligned} i\hbar\dot{c}_1|1\rangle e^{-i\omega_1 t} + i\hbar\dot{c}_2|2\rangle e^{-i\omega_2 t} &= \sum|n\rangle\langle n|x|1\rangle eE_0\cos(\omega t)c_1e^{-i\omega_1 t} + \sum|n\rangle\langle n|x|2\rangle eE_0\cos(\omega t)c_2e^{-i\omega_2 t} \\ &= |2\rangle\langle 2|x|1\rangle eE_0\cos(\omega t)c_1e^{-i\omega_1 t} + |1\rangle\langle 1|x|2\rangle eE_0\cos(\omega t)c_2e^{-i\omega_2 t} \end{aligned} \tag{2.16}$$

since $\langle n|x|n\rangle = 0$ due to symmetry. From this, we find equations for amplitudes $c_1$ and $c_2$:

$$\begin{aligned} i\dot{c}_1 &= \Omega\cos(\omega t)e^{-i\omega_0 t}c_2 = \frac{\Omega}{2}(e^{i(\omega-\omega_0)t} + e^{-i(\omega+\omega_0)t})c_2 \\ i\dot{c}_2 &= \Omega^*\cos(\omega t)e^{i\omega_0 t}c_1 = \frac{\Omega^*}{2}(e^{i(\omega+\omega_0)t} + e^{-i(\omega-\omega_0)t})c_1 \end{aligned} \tag{2.17}$$

where the Rabi frequency is $\Omega = \frac{eE_0\langle 1|x|2\rangle}{\hbar}$ and $\omega_0 = \omega_2 - \omega_1$. The rotating-wave approximation tells us that we can drop the term with $(\omega+\omega_0)t$ since it oscillates very fast and thus will average to zero over our interaction time. Thus Eq. 2.17 becomes,

$$\begin{aligned} i\dot{c}_1 &= \frac{\Omega}{2}e^{i(\omega-\omega_0)t}c_2 \\ i\dot{c}_2 &= \frac{\Omega^*}{2}e^{-i(\omega-\omega_0)t}c_1 \end{aligned} \tag{2.18}$$

Taking a time derivative of Eq. 2.18, one finds

$$\begin{aligned} \ddot{c}_1 - (\omega - \omega_0)\dot{c}_1 + \frac{|\Omega|^2}{4}c_1 = 0 \\ \ddot{c}_2 + (\omega - \omega_0)\dot{c}_2 + \frac{|\Omega|^2}{4}c_2 = 0 \end{aligned} \tag{2.19}$$

Taking the entire population to be in the ground state at $t = 0$, or $c_1(0) = 1$ and $c_2(0) = 0$, the solution to Eq. 2.19 gives the probability of being in each state as a function of time:

$$\begin{aligned} |c_1(t)|^2 &= \frac{\Omega^2}{\Omega^2 + (\omega - \omega_0)^2} \cos^2 \frac{\sqrt{\Omega^2 + (\omega - \omega_0)^2}t}{2} = \frac{\Omega^2}{\Omega^2 + \delta^2} \cos^2 \frac{\sqrt{\Omega^2 + \delta^2}t}{2} \\ |c_2(t)|^2 &= \frac{\Omega^2}{\Omega^2 + (\omega - \omega_0)^2} \sin^2 \frac{\sqrt{\Omega^2 + (\omega - \omega_0)^2}t}{2} = \frac{\Omega^2}{\Omega^2 + \delta^2} \sin^2 \frac{\sqrt{\Omega^2 + \delta^2}t}{2} \end{aligned} \tag{2.20}$$

where the detuning of the frequency of the electromagnetic radiation from the transition frequency is $\delta = \omega - \omega_0$. As seen from Eq. 2.20, the maximal transition amplitude depends on the detuning, and the population transfer oscillates in time at a rate proportional to the strength of the field. Figure 2.4 compares population transfer between the states for different detunings and Rabi frequencies over time. Fig. 2.5 shows the probability of population transfer versus detuning for the $\pi$-time, the shortest time for complete state transfer with zero detuning.

### *2.3.1 Transition Selection Rules: Effects of Polarization*

As discussed above, we saw that for an interaction between electromagnetic radiation and the electric dipole of an atom the Rabi frequency was proportional to the dipole matrix element $\langle 1|\mathbf{r}\cdot\hat{\mathbf{e}}_{rad}|2\rangle$ where $\hat{\mathbf{e}}_{rad}$ is the polarization direction of the interacting radiation. It is useful to briefly understand how the polarization direction of the radiation affects which transitions are permitted. Written in integral form, this transition matrix element is

$$\langle 1|\mathbf{r}\cdot\hat{\mathbf{e}}_{rad}|2\rangle = \int_0^\infty R_{n1,l1}(r) r R_{n2,l2}(r) r^2 dr \int_0^{2\pi}\int_0^{\pi} Y^*_{l1,m1}(\theta,\phi)\hat{\mathbf{r}}\cdot\hat{\mathbf{e}}_{rad} Y_{l2,m2}(\theta,\phi)\sin\theta d\theta d\phi \tag{2.21}$$

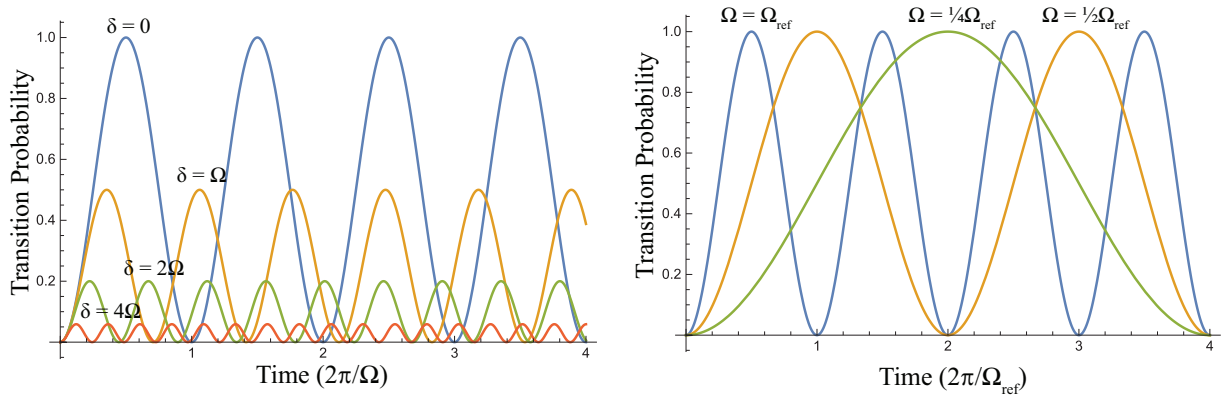


Figure 2.4: The transition probability versus time is shown for several different detunings on the left. On the right, the transition probability versus time is shown for different magnitude Rabi Frequencies corresponding to more or less laser power.

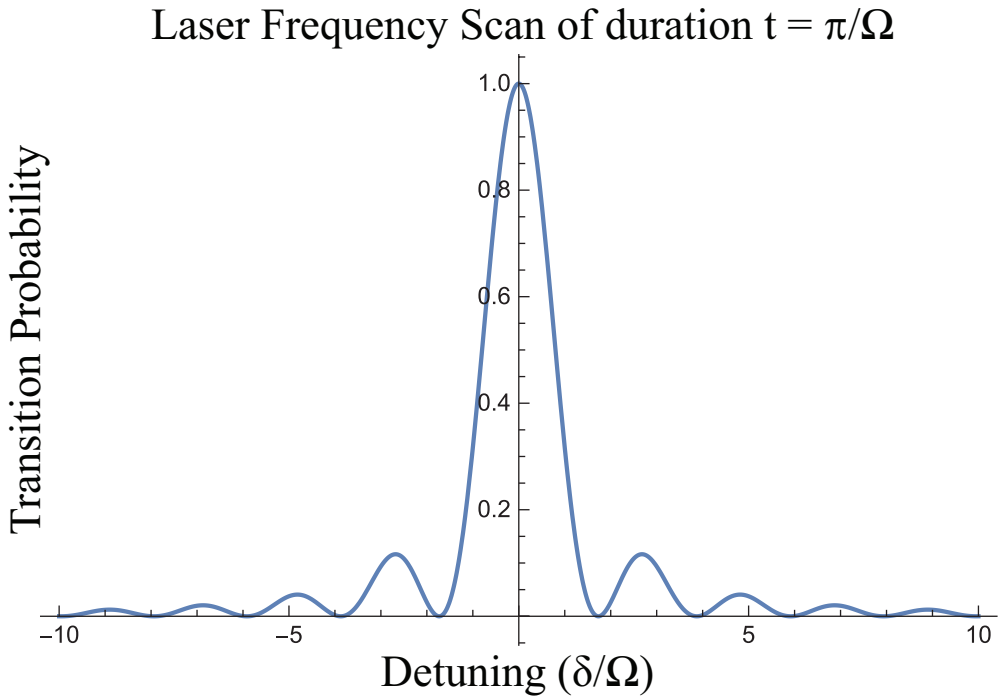


Figure 2.5: For a given interaction time, here the $\pi$-time, as the frequency is scanned from from red detuning to blue detuning, one is able to find the resonance frequency at the maximum transition probability (with the precaution that as the set interaction time increases past the $\pi$-time, the maximum transition probability for zero detuning will decrease toward zero and increase again in a periodic manner).

The directions of the dipole and the polarization can be written in terms of the $Y_{l,m}$ angular wavefunctions and the basis vectors associated with $\pi$- and $\sigma$-polarized radiation:

$$\hat{\mathbf{r}} = \sin\theta\cos\phi\hat{\mathbf{x}} + \sin\theta\sin\phi\hat{\mathbf{y}} + \cos\theta\hat{\mathbf{z}} \propto Y_{1,-1}\frac{\hat{\mathbf{x}} + i\hat{\mathbf{y}}}{\sqrt{2}} - Y_{1,1}\frac{\hat{\mathbf{x}} - i\hat{\mathbf{y}}}{\sqrt{2}} + Y_{1,0}\hat{\mathbf{z}}$$

$$\hat{\mathbf{e}}_{rad} = A_{\sigma^+}\frac{\hat{\mathbf{x}} + i\hat{\mathbf{y}}}{\sqrt{2}} - A_{\sigma^-}\frac{\hat{\mathbf{x}} - i\hat{\mathbf{y}}}{\sqrt{2}} + A_{\pi}\hat{\mathbf{z}} \tag{2.22}$$

Thus,

$$\mathbf{r}\cdot\hat{\mathbf{e}}_{rad} \propto A_{\sigma^+}Y_{1,-1} + A_{\sigma^-}Y_{1,1} + A_{\pi}Y_{1,0} \tag{2.23}$$

For $\pi$-polarized radiation, the angular integral from the transition matrix element becomes

$$I \propto \int_0^{2\pi}\int_0^{\pi} Y^*_{l1,m1}(\theta,\phi)A_{\pi}Y_{1,0}Y_{l2,m2}(\theta,\phi)\sin\theta d\theta d\phi \tag{2.24}$$

where the azimuthal portion of the integral is

$$\begin{aligned} I &\propto \int_0^{2\pi} e^{i(m2-m1)\phi}d\phi = 0 \quad \text{if} \quad m1 \neq m2 \\ &\propto \int_0^{2\pi} d\phi = 2\pi \qquad\qquad \text{if} \quad m1 = m2 \end{aligned} \tag{2.25}$$

Thus, when $\pi$-polarized radiation is incident on the atom, the magnetic quantum number, $m$, will remain the same for the transition, that is $\Delta m = 0$.

For $\sigma$-polarized radiation, the angular integral from the transition matrix element becomes

$$I \propto \int_0^{2\pi}\int_0^{\pi} Y^*_{l1,m1}(\theta,\phi)A_{\sigma^{\pm}}Y_{1,\pm1}Y_{l2,m2}(\theta,\phi)\sin\theta d\theta d\phi \tag{2.26}$$

where the azimuthal portion of the integral is

$$\begin{aligned} I &\propto \int_0^{2\pi} e^{i(m2-m1\pm1)\phi} d\phi = 0 \quad \text{if} \quad m1 \neq m2 \pm 1 \\ &\propto \int_0^{2\pi} d\phi = 2\pi \qquad\qquad\qquad\quad \text{if} \quad m1 = m2 \pm 1 \end{aligned} \tag{2.27}$$

Thus, when $\sigma$-polarized radiation is incident on the atom, the magnetic quantum number, $m$, will increase or decrease by 1 in the transition for $\sigma^+$-polarized or $\sigma^-$-polarized radiation respectively, that is $\Delta m = +1$ or $\Delta m = -1$ respectively. Calculating the entire transition matrix integral will determine the selection rules that apply to $l$ for dipole versus quadrupole or other order transitions, however these will not be derived here. It is worth noting though, that for an electric dipole transition $\Delta l = \pm 1$, for a magnetic dipole transition $\Delta l = 0$ and $\Delta n = 0$, and for an electric quadrupole transition $\Delta l = 0, \pm 2$ (in an electric quadrupole it is also possible for $\Delta m = \pm 2$ in addition to those allowed transitions allowed for a dipole).

# Chapter 3

# HOW DO WE TRAP IONS?

*There are many examples in physics showing that higher precision revealed new phenomena, inspired new ideas, or confirmed or dethroned well-established theories.*

- Wolfgang Paul

In order to utilize the atomic structure described in Chapter 2 to perform the experiment outlined in Chapter 1, there must be a method for localizing a single ion free from interactions with other particles and fields so that it can easily be measured and manipulated. Unfortunately, Earnshaw's Theorem tells us that a charged particle acted on by electrostatic forces alone cannot rest in stable equilibrium. This follows simply from Gauss's law for a particle in free space where $\nabla \cdot \mathbf{E} = 0$. Since $\mathbf{E} = \nabla\phi$, then $\nabla^2\phi = \frac{\partial^2\phi}{\partial x^2} + \frac{\partial^2\phi}{\partial y^2} + \frac{\partial^2\phi}{\partial z^2} = 0$. In order for this to be true, at least one of the second derivatives of the electric potential must be negative, and thus the equilibrium is unstable in that direction (if all the second derivatives were zero, the potential would be constant and thus have no confining or equilibrium restoring force). In the 1950s, Hans Dehmelt and Wolfgang Paul built the first ion traps, the Penning (named for physicist Frans Michel Penning whose vacuum gauge inspired Dehmelt) and Paul traps respectively. The traps used a combination of magnetic and or electric fields. As the experiments to be described in the results sections of this dissertation utilized Paul traps, this discussion will be confined to the operation of those traps.

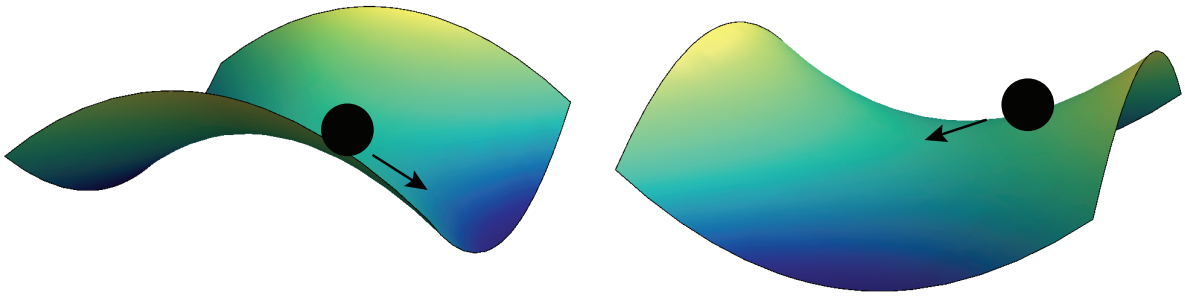

Figure 3.1: Ordinarily the ball would roll down the sides away from the center of the saddle. However, if the saddle were flapping or rotating instead of being static, the sides would flip between concave up and concave down thus pushing the ball back and forth about the center of the saddle.

### *3.1 The Paul Trap*

The Paul trap utilizes a quadrupole electric potential that oscillates at radio-frequency in order to produce a time-averaged harmonic potential in three dimensions

$$\Phi(x, y, z) = \frac{1}{2} m(\omega_x^2 x^2 + \omega_y^2 y^2 + \omega_z^2 z^2) \tag{3.1}$$

where $m$ is the mass of the ion and $\omega_x$, $\omega_y$, and $\omega_z$ are known as the secular frequencies in the $x$, $y$, and $z$ directions. One can understand qualitatively how a Paul trap confines an ion by imagining it as a ball moving on a saddle-shaped surface as shown in Fig. 3.1. For a ball subject to the force of gravity, the gravitational potential would be defined by the surface. Take for example here a symmetric saddle corresponding to a quadrupole potential:

$$V = x^2 - y^2 \tag{3.2}$$

Ordinarily in such a static potential, the ball would tend to roll off the sides of the saddle. However, if the potential were either flapping or rotating, the negative gradient in one direction tending to push the ball away from the center would now switch back and forth between

positive and negative gradients, thus alternating between pushing the ball away from the center and pushing the ball back toward the center. The ball thus undergoes some sort of oscillatory motion about the center of the saddle. For a more quantitative treatment of this effect, we may begin with an in-depth look at the first form of the Paul trap made from a ring electrode and two endcaps as shown in Fig. 3.2.

Since the equipotential lines of the quadrupole potential are hyperbolas, the trap utilizes hyperbolic electrodes in order to set the boundary conditions of the potential. A potential $V = U_0 + V_0 \cos(\Omega t)$ is applied between the the ring electrode and endcap electrodes. Knowing that the electrostatic potential must satisfy Laplace's equation $\nabla^2 \phi = 0$ and the boundary conditions, this gives rise to the quadrupole potential

$$\phi = \phi_0 + (U_0 + V_0 \cos(\Omega t))(\frac{x^2 + y^2 - 2z^2}{r_0^2 + 2z_0^2}) \tag{3.3}$$

where $r_0^2 = 2z_0^2$, $r_0$ is the radius of the ring electrode, and $2z_0$ is the distance between the endcaps.

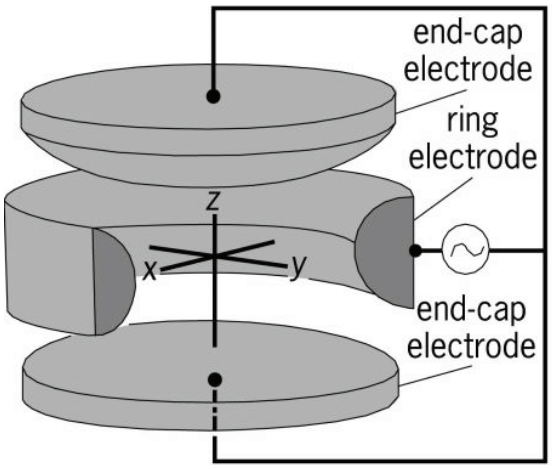


Figure 3.2: Paul trap with hyperbolic ring and endcap electrodes where $r_0$ is the radius of the ring electrode, and $2z_0$ is the distance between the endcaps. A potential is applied across the electrodes with both DC and AC components.

We can find the equations of motion for the ion from the gradient of the electric potential.

$$m\frac{d^2\mathbf{r}}{dt^2} = \mathbf{F} = -e\mathbf{E} = -e\nabla\phi \tag{3.4}$$

The equations of motion are as follows

$$\begin{aligned} m\frac{d^2x}{dt^2} &= -2e\frac{(U_0 + V_0\cos(\Omega t))}{r_0^2 + 2z_0^2}x \\ m\frac{d^2y}{dt^2} &= -2e\frac{(U_0 + V_0\cos(\Omega t))}{r_0^2 + 2z_0^2}y \\ m\frac{d^2z}{dt^2} &= 4e\frac{(U_0 + V_0\cos(\Omega t))}{r_0^2 + 2z_0^2}z \end{aligned} \tag{3.5}$$

Making the substitution $t' = \frac{\Omega t}{2}$, such that $\frac{d}{dt'} = \frac{2}{\Omega}\frac{d}{dt}$, Eq. 3.5 becomes

$$\begin{aligned} \frac{d^2x}{dt'^2} &= -8e\frac{(U_0 + V_0\cos(2t'))}{m\Omega^2(r_0^2 + 2z_0^2)}x \\ \frac{d^2y}{dt'^2} &= -8e\frac{(U_0 + V_0\cos(2t'))}{m\Omega^2(r_0^2 + 2z_0^2)}y \\ \frac{d^2z}{dt'^2} &= 16e\frac{(U_0 + V_0\cos(2t'))}{m\Omega^2(r_0^2 + 2z_0^2)}z \end{aligned} \tag{3.6}$$

These look like the Matthieu equation

$$\frac{d^2x}{dt'^2} + (a_x + 2q_x\cos(2t'))x = 0 \tag{3.7}$$

with

$$a_x = a_y = \frac{8eU_0}{m\Omega^2(r_0^2 + 2z_0^2)} = -\frac{1}{2}a_z \quad \text{and} \quad q_x = q_y = \frac{4eV_0}{m\Omega^2(r_0^2 + 2z_0^2)} = -\frac{1}{2}q_z \tag{3.8}$$

When $a_x < q_x^2 \ll 1$, solutions to the Matthieu equation may be expanded in terms of $a_x$ and $q_x$. The leading order solution is of the form

$$x(t) = Acos(\omega_x t + \phi)(1 + \frac{q_x}{2}\cos(\Omega t)) \tag{3.9}$$

where

$$\omega_x = \sqrt{q_x^2/2 + a_x}(\Omega/2) \tag{3.10}$$

and $A$ and $\phi$ are set by the initial position of the ion. As can be seen from Eq. 3.9, the ion will move harmonically about the center of the trap in the x-direction at the secular frequency $\omega_x$. This motion is also perturbed by fast periodic motion of small amplitude (since $q_x^2 \ll 1$) at the RF driving frequency $\Omega$. This is known as the micromotion. A graph of the x-position of the ion in the trap versus time is shown in Fig. 3.3.

If a static background electric field with magnitude $E_0$ in the x-direction is present, then Eq. 3.7 becomes

$$\frac{d^2x}{dt'^2} + (a_x + 2q_x\cos(2t'))x = \frac{eE_0}{m} \tag{3.11}$$

which has solution

$$x(t) = Acos(\omega_x t + \phi)(1 + \frac{q_x}{2}\cos(\Omega t)) + \frac{eE_0}{m\omega_x^2} + \frac{\sqrt{2}eE_0}{m\omega_x\Omega}\cos(\Omega t) \tag{3.12}$$

As seen from Eq. 3.12, the extra terms in the solution correspond to an offset from the RF node at the center of the trap and excess micromotion. This unwanted effect can be corrected by the introduction of compensation electrodes into the trap which can counteract any constant background electric fields by applying a DC voltage difference. It is important to do this as the excess micromotion will have several adverse effects such as reducing ion trapping lifetime and broadening atomic transitions. The ion motion when subject to a background field is also shown in Fig. 3.3 in comparison.

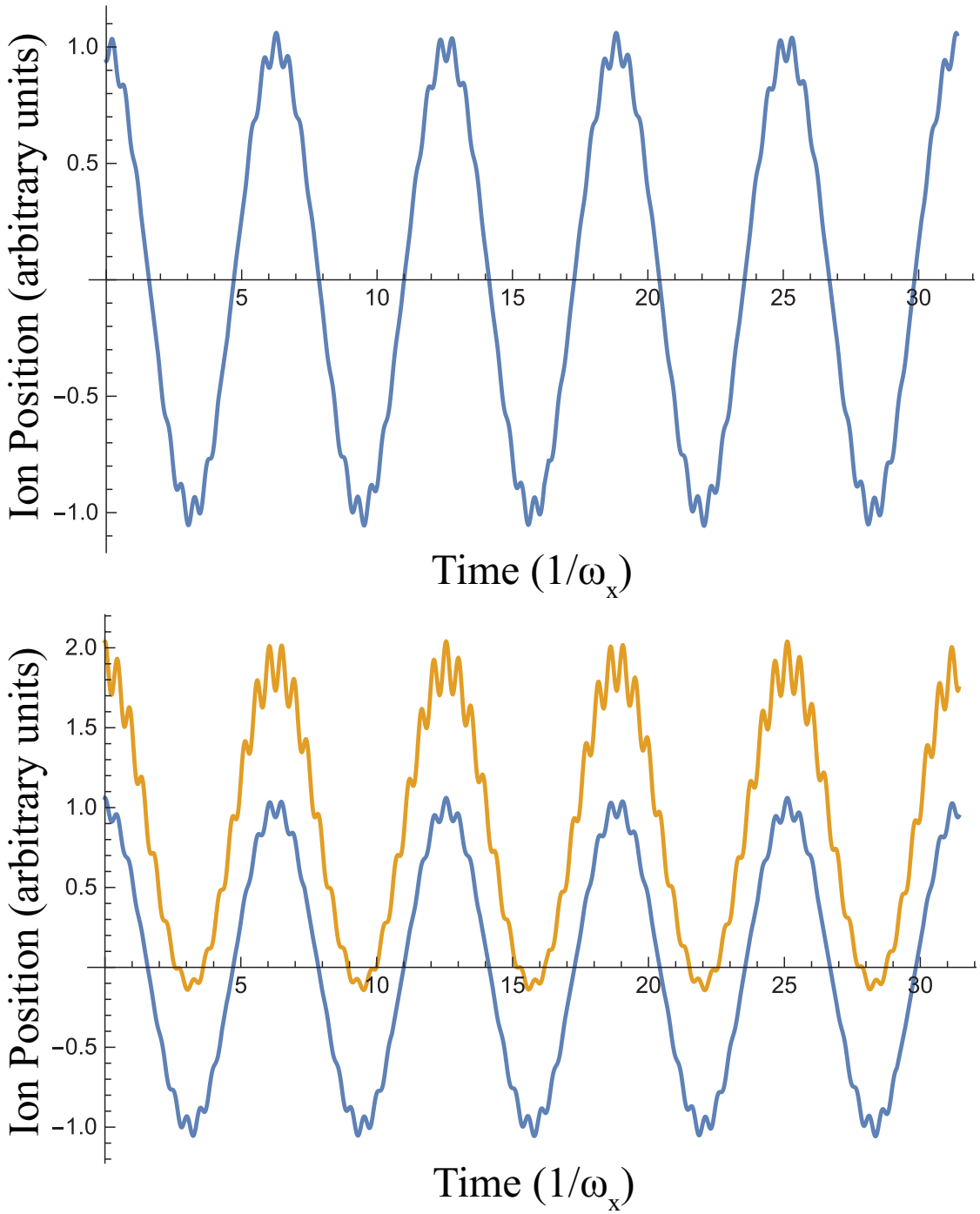


Figure 3.3: The top figure shows the motion in the x-direction of an ion in the trap. The large motion occurs at the secular frequency, while the small perturbations known as micromotion occur at the RF frequency of the applied AC voltage. The bottom figure shows the motion of an ion when a constant background electric field is present. As can be observed from the comparison with the first function, the background field causes the ion to shift away from the null position of the quadrupole potential, and excess micromotion occurs.

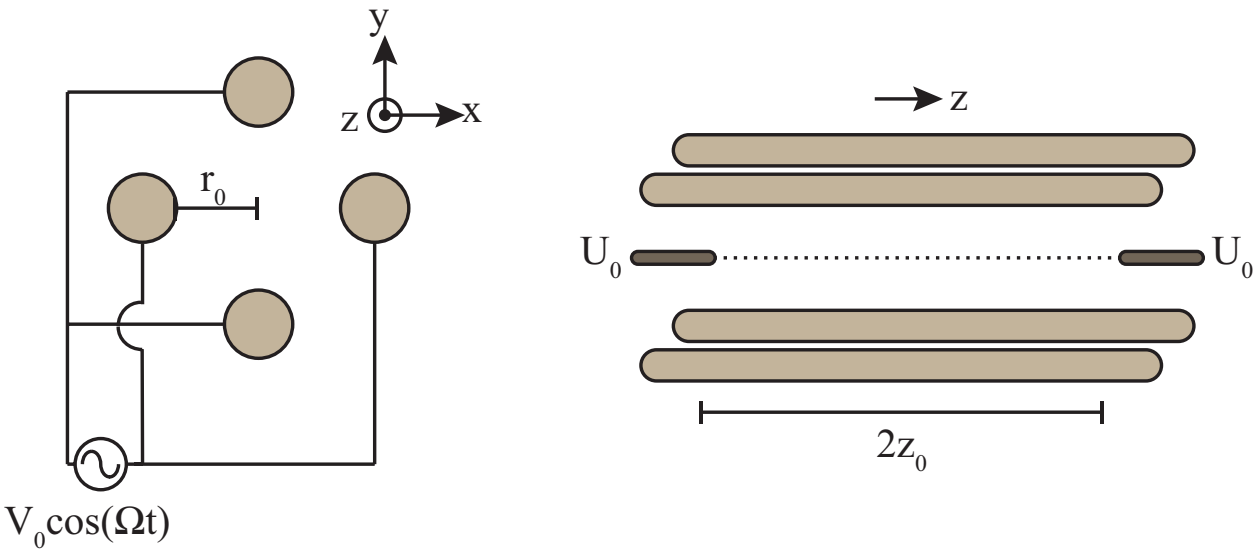


Figure 3.4: On the left is a cross-section of a linear Paul trap. Instead of a ring electrode, the linear Paul trap uses four rods extended along the z-axis of the trap to confine an ion radially. The rods diagonally across from one another are connected and an AC voltage is applied between the pairs. The endcap electrodes shown in the side view on the right are dc-biased in order to confine the ion axially. This trap configuration allows for ion chains as it is possible to make the radial confinement much stronger than the axial confinement.

### *3.1.1 Linear Paul Traps*

The linear Paul trap is a mutation from the original Paul trap which works in a similar fashion. The ring is replaced by four rods parallel to the z-axis. These four rods provide confinement in the radial direction by producing an oscillating quadrupole electric field. The rods opposite one another in the xz-plane are connected and the rods opposite one another in the yz-plane are also connected. An AC voltage $V = V_0 \cos(\Omega t)$ is applied between the pairs of rods for radial confinement whilst the endcap electrodes are DC-biased in order to create a harmonic confinement in the axial direction. The linear Paul trap is shown in Fig. 3.4.

### *3.2 Doppler Cooling*

In order to perform experiments on trapped ions, it is also useful to cool the ion down as its spatial extent when first trapped is a larger portion of the trap volume than desirable for performing precision experiments. This is achieved using Doppler cooling as first proposed by [60] and [22]. In short, photons carry momentum which is transferred to and from an ion when the photon is absorbed or emitted. Since photon emission is spherically symmetric for large numbers of photons, overall emission will not change the momentum of the ion. The question then becomes, can the setup be arranged so that ions absorb more photons traveling in a direction that will slow the ion through recoil velocity, i.e. opposite the direction of motion of the ion? The use of the Doppler effect is key in this regard. One knows from the Doppler effect that for an observer moving toward a light source, the wavelength will appear compressed resulting in the observed blue-shift of the light. This effect can be leveraged to cool an ion by focusing onto the ion light that is red-shifted from the energy transitions of that ion. Those photons traveling opposite the direction of the ion will be blue-shifted back toward resonance and thus more likely to be absorbed than any photons traveling in the same direction as the ion. The net effect of this results in a drag force on the ion.

For ion trapping, it is important that the laser or lasers providing the Doppler cooling are aligned such that the photons have a component of momentum in all three directions of symmetry of the trap. This ensures that the ion experiences a drag force and is cooled in all three dimensions of its motion.

# Chapter 4

# ION TRAPS

Two different traps were used for the experiments performed in this work. The first was similar to the standard four-rod linear Paul trap described in Chapter 3 while the second was designed based on a symmetry-preserving mutation of the ring trap also described there. The two different traps are described below.

## *4.1 Blade Trap*

The Blade Trap shown in Fig. 4.1 was designed by a prior graduate student, Tom Noel. In order to make the electrodes closer to the center of the trap whilst not limiting optical access for addressing the ion with lasers or light collection along the imaging axis, it was designed with blade tips. This allowed for a tighter trap since there is an inverse relationship between the secular frequency and the distance separating the ion from the electrodes as described by Eqs. 3.10 and 3.8 in Chapter 3. The four blades provided the oscillating quadrupole electric field confining the ion in the radial direction while two dc-biased endcaps provided harmonic confinement in the axial direction. Insulating spacers held all the electrodes and endcaps together and also allowed for the incorporation of micromotion compensation electrodes in the radial directions.

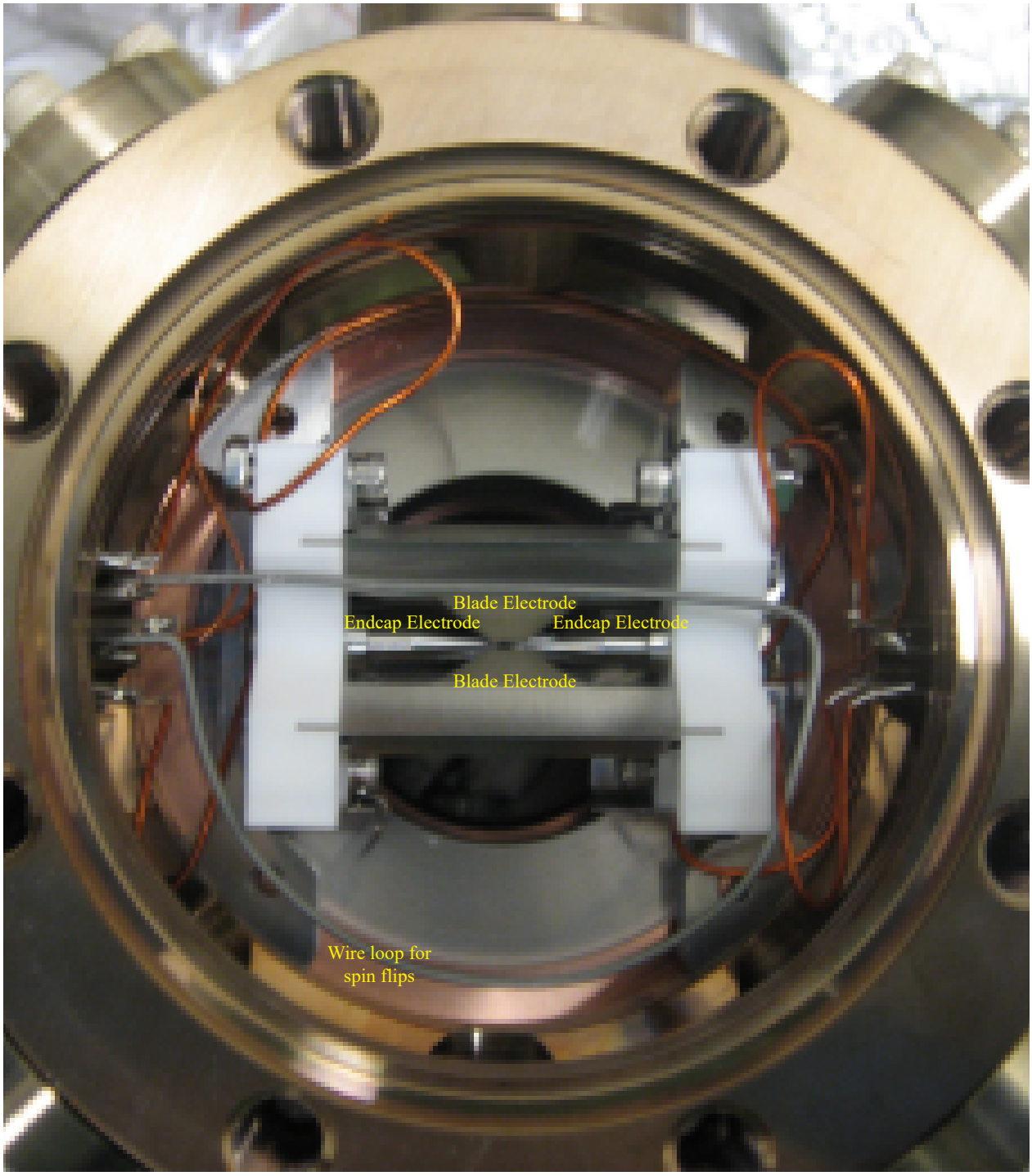


Figure 4.1: A picture of the blade trap inside the spherical octagon chamber. The two of the four blade electrodes which are visible, the endcap electrodes, and the wire loop for driving spin flips are labeled.

The RF voltage was coupled onto the blade electrodes through a vacuum feed-through from a quarter-wave helical resonator with $Q \approx 400$ connected to an HP8640 signal generator. The output of the HP8640 is amplified and matched to the frequency of the resonator which further amplifies the signal and matches to the impedance of the trap. The end-cap and compensation electrodes are connected to DC voltage sources through a separate feed-through.

The trap is placed in a spherical octagon chamber and pumped down to UHV. The combined action of a 20 l/s ion pump and periodic flashes of a titanium filament in a titanium sublimation pump maintain the pressure in the vacuum chamber below the $7 \times 10^{-12}$ Torr minimum readable pressure of the Varian senTorr BA2C gauge controller with a Varian UHV-24p ionization gauge installed in the chamber. The feed-throughs mentioned *supra* occupy two of the eight sides of the chamber. The other six provide optical access for the various laser beams utilized to cool and address the ion. A view port mounted to a recessed flange on top of the chamber provides access for photon collection. The external glass surface is only 1.3 cm above the ion position thus allowing for maximization of the solid angle of light collection.

A dedicated tungsten wire loop was incorporated in the vicinity of the trap inside the vacuum chamber and was used to generate a tunable RF magnetic field in order to drive magnetic dipole transitions between the Zeeman sublevels for the necessary ion qubit rotations. An RF synthesizer (based on a direct digital synthesis (DDS9910) chip) generated a stable sinusoidal voltage which was amplified and dropped over a 50 ohm RF resistor for impedance matching, producing an oscillating current in the loop. This setup allowed for ion qubit rotations with a tunable phase as described in Chapter 6.

The source of barium ions is provided by a barium "oven" consisting of shaved metallic barium pieces in an alumina tube with a tungsten wire coiled around it. The wire ends are

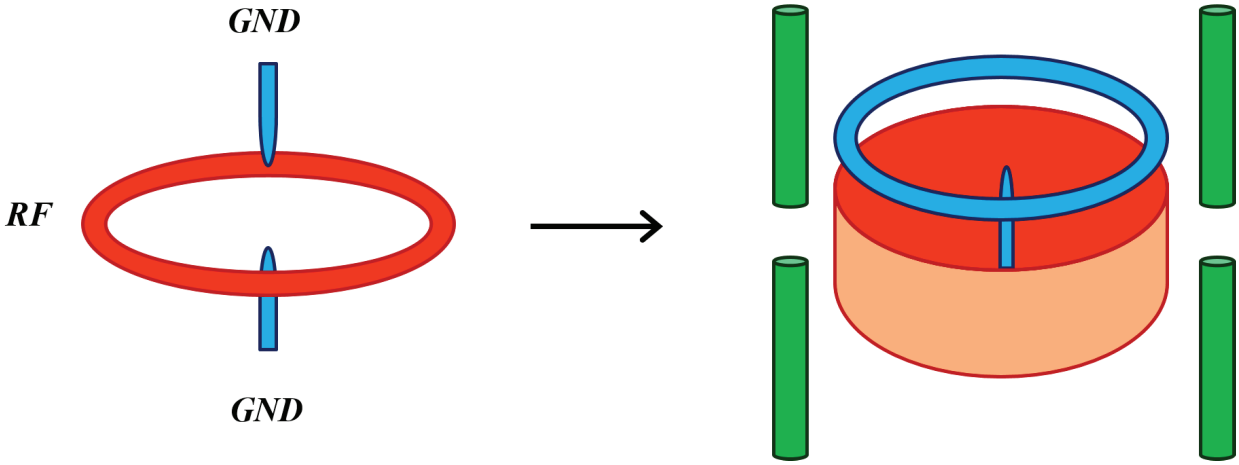


Figure 4.2: The ring trap may be deformed while maintaining its symmetry into the parabolic mirror trap. The ring electrode is deformed into the parabolic mirror electrode and one of the end cap electrodes is deformed into a ring. Four compensation electrodes shown in green are added to correct for background fields.

connected to another feed-through. When a current is passed through the tungsten wire, it heats the barium in the tube causing a barium flux to pass through the trap volume.

### *4.2 Parabolic Mirror Trap*

The parabolic mirror trap shown in Fig. 4.3 is contained in a vacuum system and coupled to voltage sources through feed-throughs similarly to the blade trap. The idea for the design of the parabolic mirror trap comes from deforming the electrodes of the ring trap while maintaining its symmetry. The ring electrode becomes the parabolic mirror electrode while the endcap electrodes become the needle and top plate electrodes as shown in Fig. 4.2. In this way the desired trapping potential is maintained while introducing an integrated optical surface for a greatly increased light collection efficiency. In the traps used here the needle and top plate are grounded while the parabolic mirror is connected to the RF voltage through a vacuum feed-through. The needle is connected to a linear actuator which allows it to be moved axially. This enables ions to be loaded into the trap above the top of the mirror surface so that it remains clean of any barium flux. Once an ion is trapped, the linear

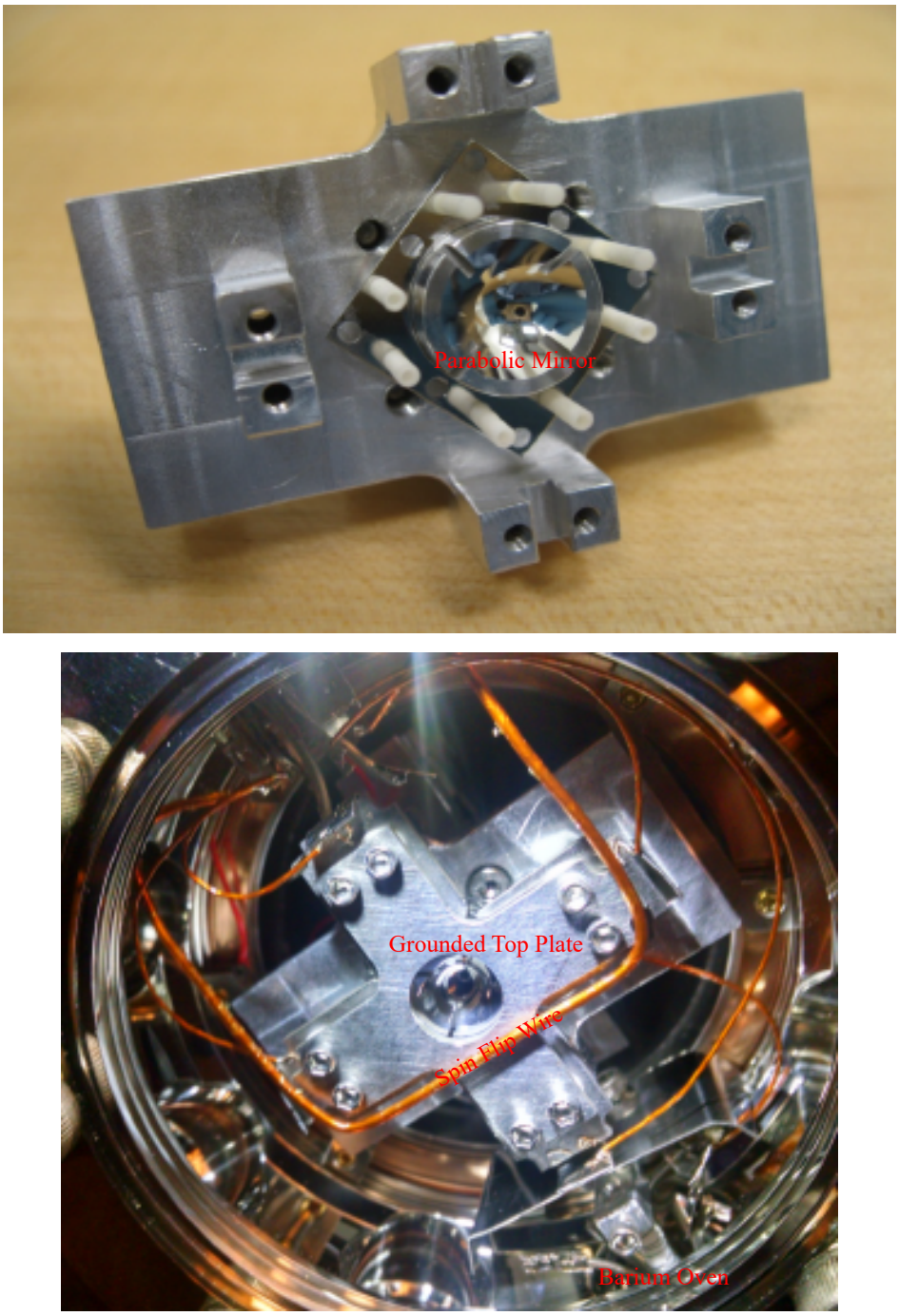


Figure 4.3: On the top is a picture of the parabolic mirror before it was installed into the UHV chamber. A picture of the parabolic mirror trap inside the spherical octagon chamber is shown in the bottom image. The grounded top plate, the parabolic mirror electrode, the wire loop for driving spin flips, and the barium "oven" are labeled. The hole in the center of the mirror from which the grounded needle electrode protrudes and the cuts in the mirror for laser access are also visible.

actuator can bring the ion to the position of the focus of the mirror. The parabolic mirror allows for photon collection of over 40% of the solid angle and also collimates the fluorescence when the ion is situated at the focus of the mirror. Thus far, we have achieved 10% fiber coupling efficiency, for total light collection by the fiber of 4%.

To eventually demonstrate ion-ion entanglement utilizing the scheme discussed in Chapter 1, a second parabolic mirror trap is necessary for the second ion. While building the second trap, I took the opportunity to incorporate several improvements. In order to improve the collimation of the light collected from the ion thereby increasing the maximum fiber coupling efficiency, radial control of the needle position is needed so that the null of the trapping potential and the focus of the mirror coincide. This thereby minimizes any excess micromotion occurring when the ion is located at the focus of the mirror. I tested Thorlabs Co-Fired Piezoelectric Actuators to pressures below the readable pressure of the Varian senTorr BA2C gauge controller, and having found them to be operable under UHV, I designed and machined a part to hold two piezos against the needle that could change its radial position within the trap in each radial dimension. The part was designed so that the 150 V piezos with maximum displacement of 17.4 $\mu$m could be placed as far from the tip of the needle as the physical geometry of the vacuum joints would allow in order to maximize the movable distance of the needle tip. Each piezo was connected to feed-throughs in order to supply the 0 V to 150 V necessary to attain the maximum range of motion. While assembling the trap, 75 V was applied to each piezo and their positions were adjusted by set screws in order to roughly position the needle along the central axis of the parabolic mirror. The positioning of the needle along the central axis of the mirror was judged by viewing reflections off of the needle tip and making incremental adjustments of the piezo positions with the set screws. Once this was complete, the remainder of the trap was assembled and baked down to UHV. The piezos have since been demonstrated to move the needle tip 60 to 70 $\mu$m in each radial direction. A schematic of the trap with the added control is shown in Fig. 4.4.

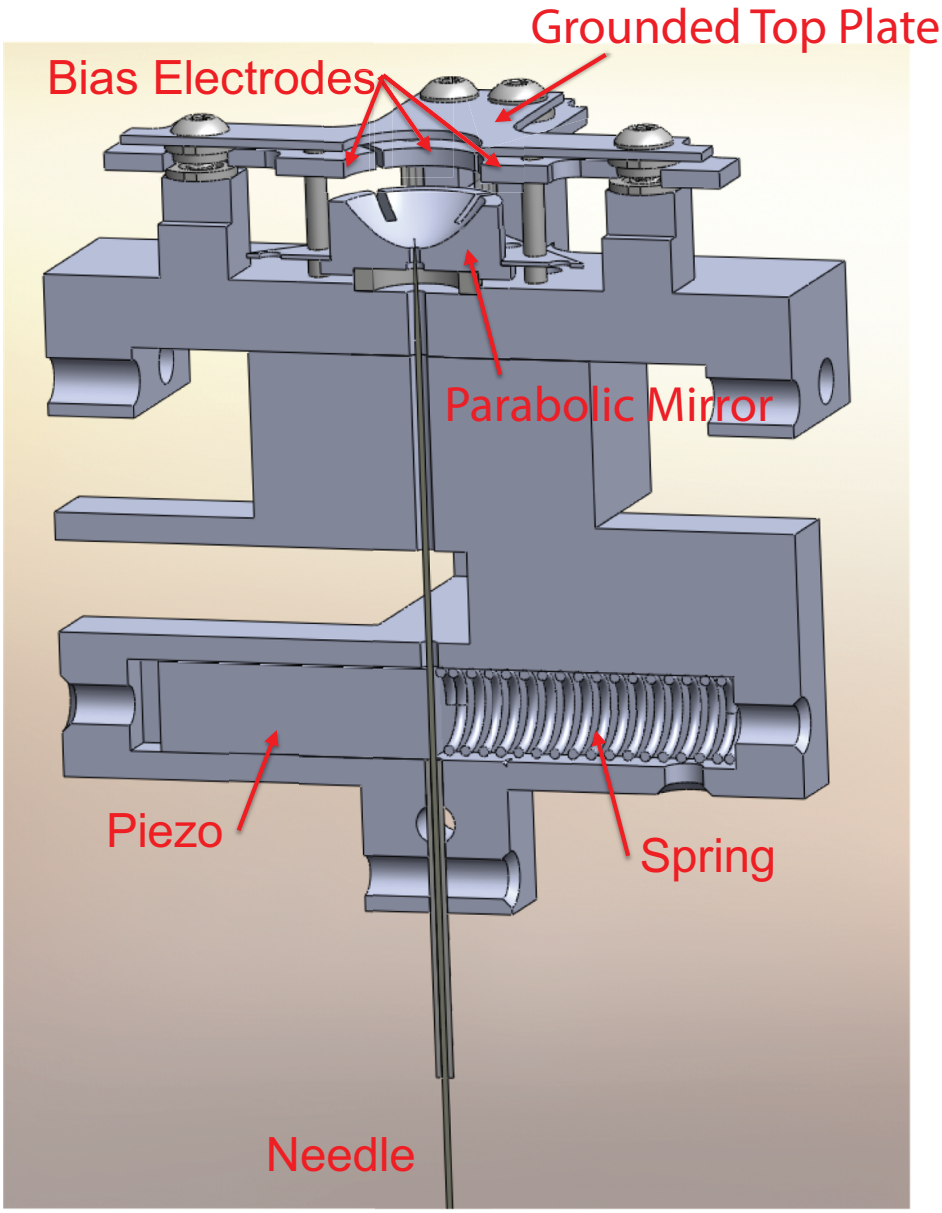


Figure 4.4: A cross section of the parabolic mirror trap attached to the part designed to hold piezos for control of the radial position of the needle is shown above. The piezos were mounted opposite springs so that the needle would rest against the surface of the piezo. By tuning the voltage applied to the piezo, the position of the needle can be controlled in the two radial dimensions. The parabolic mirror, top plate, needle, and compensation electrodes are all labeled.

Another improvement was made based on observations within the blade trap of large background counts from the ultrafast laser due to internal reflections off the viewports. Custom vacuum flanges were designed so that the viewports could be tilted by 30° in order to reduce these reflections. The flanges were designed to be as short as possible while still allowing the clamping hardware to fit. Thus the lens focusing the ultrafast pulses on the ion is able to remain closer to the trap sacrificing less focusing power.

A copper wire loop was also included inside the vacuum chamber as it was noted from experiments performed in the blade trap that heating of the tungsten wire used to drive magnetic dipole transitions between the Zeeman sublevels would heat the ion out of the trap. This limited the power that could be applied and thus limited the minimum $\pi$-time resulting in increased sensitivity to magnetic field fluctuation. The lower resistance of copper compared to tungsten helps to ameliorate this issue.

# Chapter 5

# ELECTRONIC AND LASER SYSTEMS USED FOR ION MANIPULATIONS

## *5.1 Laser Setup*

This chapter introduces all the laser systems necessary for the experiments performed in this work. Before one is able to perform any experiments with $^{138}Ba^{+}$, it is necessary to ionize the neutral barium flux from the barium "oven" described in Chapter 4. Ionization is achieved using two lasers at 791 nm and 337 nm. The home-built ECDL in Littrow configuration at 791 nm excites an intermediate transition and a pulsed nitrogen laser at 337 nm laser completes the ionization of the barium atom. The frequency of the 791 nm laser is stabilized by a side-of-the-fringe lock to a temperature-stabilized optical cavity with a linewidth close to 100MHz. This particular scheme for ionization allows for isotope selectivity since the linewidth of the 791 transition in neutral barium is much narrower than the isotope shift. Thus we are able to select for $^{138}Ba^{+}$ by tuning the frequency of the 791 laser.

Once trapped, the ion in the blade trap is cooled on the $6S_{1/2}$ to $6P_{1/2}$ transition with a 493 nm laser derived by frequency doubling a home-built 986 nm ECDL in Littrow configuration in a waveguide PPLN crystal. A home-built ECDL in Littrow configuration at 650 nm is used to repump from the long-lived $5D_{3/2}$ state (lifetime $\approx$ 80 s [20]) to which the $6P_{1/2}$ state may decay with a 25% likelihood. The 493 nm and 650 nm lasers are combined via a dichroic mirror and coupled into a single mode fiber for transmission into the trap. For the blade trap setup these lasers are also locked to temperature stabilized optical cavities while in the parabolic mirror trap setup they are locked to the desired frequency by a HighFinesse WS7 wavelength meter.

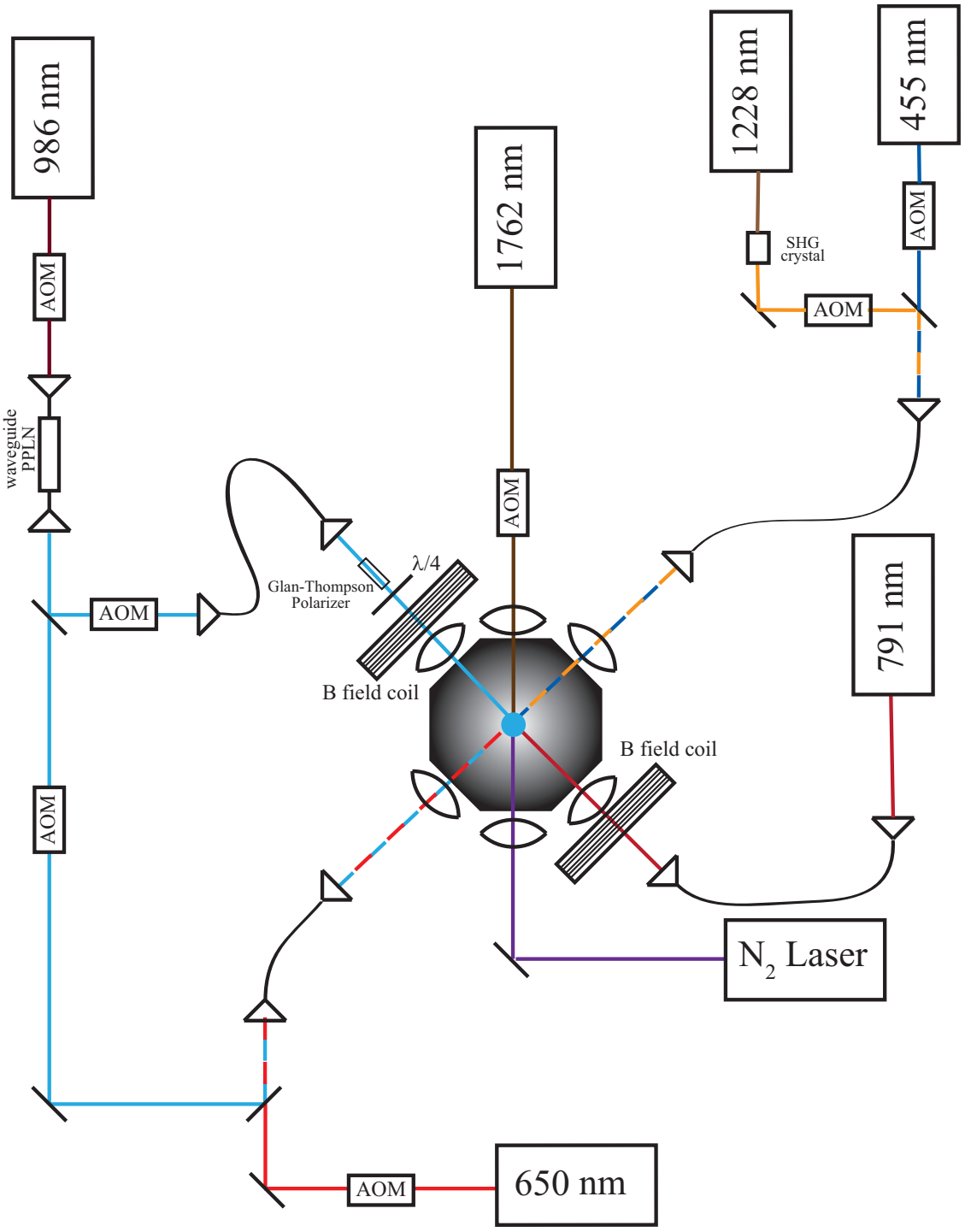


Figure 5.1: B field coils provide a quantization axis along which the optical pumping beam is aligned. Each laser is locked to a temperature stabilized optical cavity (pickoffs to cavities not shown here). All AOMs shown are used for switching, so while the deflection is not shown, the first diffracted order is sent to the ion and the zeroth order is blocked.

In order to optically pump the ion (as described in Chapter 6), the 493 nm beam is split and sent through a polarizer and $\lambda/4$ waveplate to create circularly polarized light. A 455 nm laser and a 614 nm laser are also utilized to address the $6P_{3/2}$ excited state. The 455 nm laser is another home-built ECDL in Littrow configuration, and the 614 nm light was derived by frequency doubling a 1228 ECDL in Littrow configuration. The cooling lasers and shelving laser are switched on and off in the trap through use of AOMs. Conversion efficiency to the first diffracted order is maximized and it propagates through to the ion when the AOM is on while the zeroth order is blocked.

A fiber laser at 1762 nm is utilized for ion state detection. The fiber laser is locked to a Zerodur spaced optical cavity by the PDH technique. The resulting narrow linewidth on the order of 100 Hz allows for selective coherent transitions from a single ground state Zeeman sublevel to a single Zeeman sublevel of the $5D_{5/2}$ long-lived (lifetime $\approx 30$ s) excited state.

A diagram of the laser systems for the blade trap is shown in Fig. 5.1. A diagram showing lasers addressing the ion in the parabolic mirror trap is shown in Fig. 5.2.

### *5.1.1 Ti:Sapphire Ultrafast Laser*

It is essential to the scheme used to generate ion-photon entanglement for the long-range ion-ion entanglement experiment that the ion is only excited once. Due to the short lifetimes of the $6P$ levels ($\tau \sim$ ns), it is advantageous to excite the ion with ultrafast pulses. For these purposes, a modified Coherent Mira 900-F is pumped with 10 W of 532 nm light from a Lighthouse Photonics Sprout laser. This produces about 400 mW of mode-locked 910 nm light. The output pulse width was measured by an autocorrelator to be $\Delta t \sim 600$ fs, and the repetition rate is approximately 76 MHz (twice the length of the cavity divided by the speed of light).

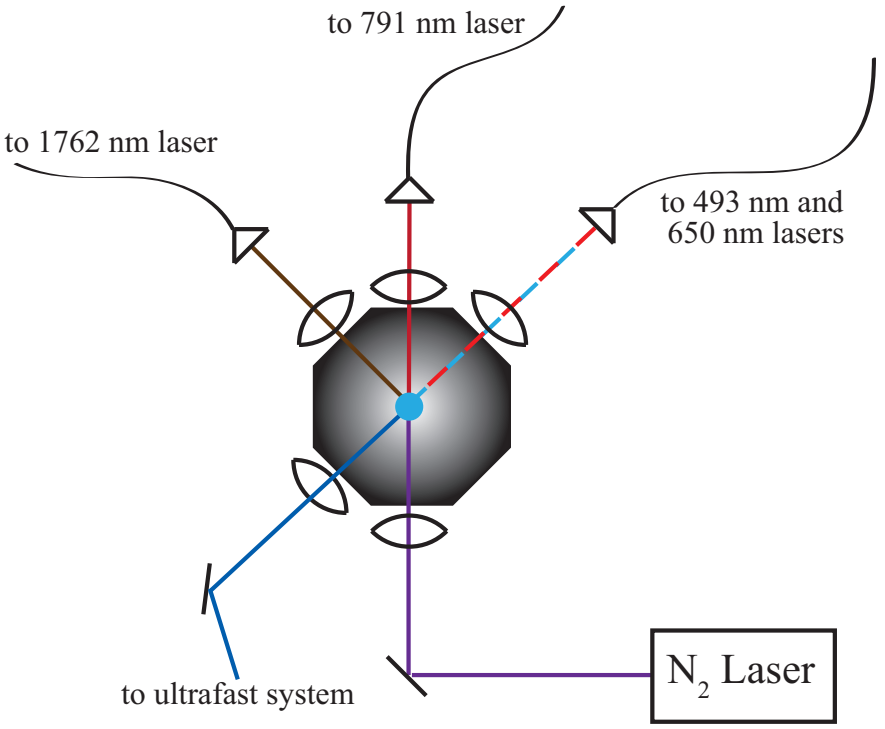


FRONT VIEW

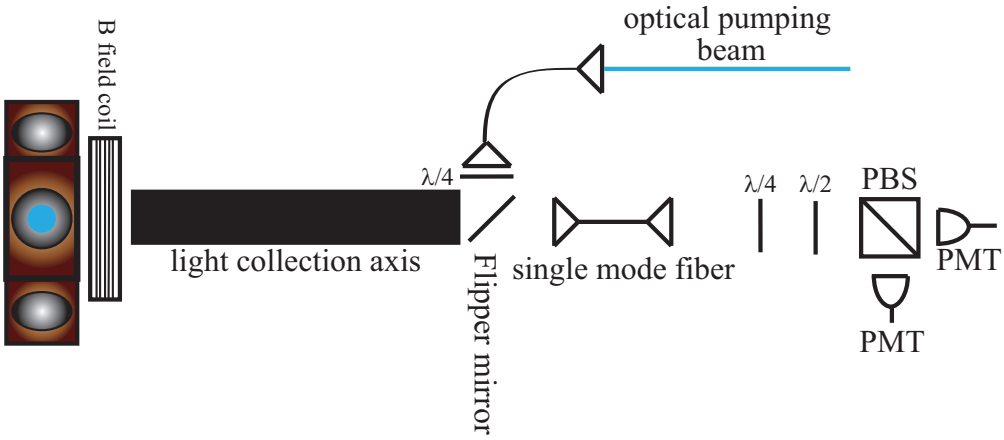


SIDE VIEW

Figure 5.2: Front and side views of the the parabolic mirror trap showing lasers addressing the ion. A B field coil provide a quantization axis along which the optical pumping beam is aligned. The cooling lasers are locked to the desired frequencies by a HighFinesse WS7 wavelength meter.

In order to pick single pulses to send through to the trap, the light is sent through a Pockels cell which is triggered by a tunable hp pulse generator triggered by an AND gate with inputs consisting of the pulse train signal from a photodiode and single-shot pulses from a DAQ card. The photodiode signal is amplified to a TTL-compatible level with a UA733 video amplifer, a MAX933 high-speed comparator and a DS1040-A15 single-shot pulse generator with 5 ns pulse width. The dead time of the DS1040-A15 misses every other pulse, halving the repetition rate of the pulse chain single sent to the AND gate. When needed, single-shot pulses are sent from a DAQ card. The output from the tunable hp pulse generator is sent to a ConOptics Model 25D Amplifier with a rise/fall time of 8 ns and a maximum voltage of 175 to operate the Model 360-80 LTA Modulator Pockels cell. After the light passes through the Pockels cell, it is frequency doubled to 455 nm through a critically phase-matched BBO crystal. The 455 nm light is separated from the 910 nm light by a prism, and finally the light is passed through an AOM triggered by a high speed switch in order to further filter the pulses directly adjacent to the picked pulse. This has resulted in a measured 40% single pulse excitation of a trapped $^{138}Ba^{+}$ ion. A diagram of the pulse picking and doubling elements is shown in Fig. 5.3.

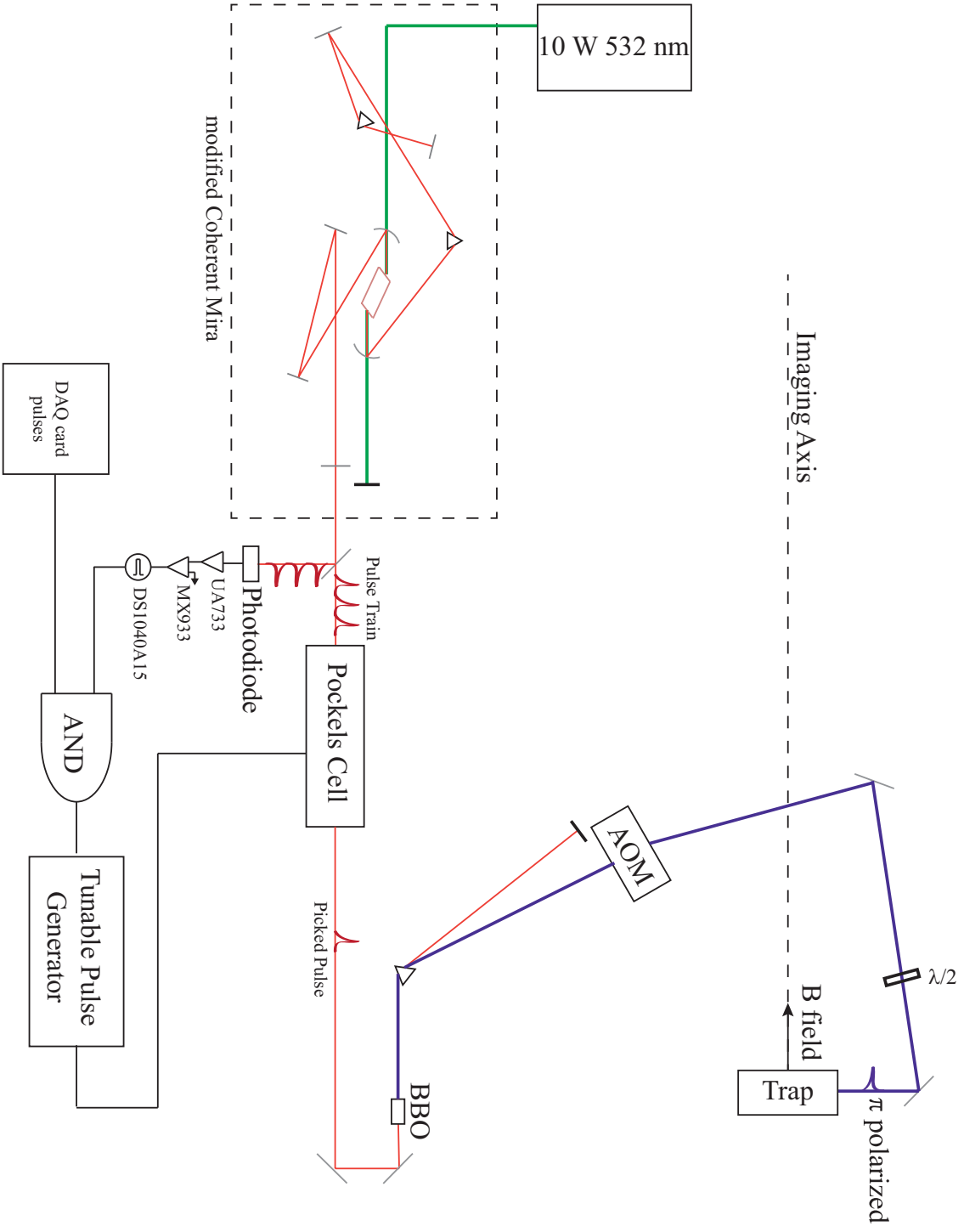


Figure 5.3: Schematic diagram of the ultrafast laser setup. 10 W of 532 nm light from a Lighthouse Photonics Sprout laser pumps a Coherent Mira 900-F. The output at 910 nm is passed through a Pockels cell triggered by the pulse train in order to pick single pulses. The resulting pulse is frequency doubled to 455 nm by a BBO and further filtered by an AOM before being focused into the trap. The light is well polarized and a $\lambda/2$ waveplate is utilized to create $\pi$-polarized pulses entering the trap perpendicular to the quantization axis.

# Chapter 6

# STATE INITIALIZATION AND MEASUREMENT TECHNIQUES

This chapter summarizes the methods utilized for ion state initialization, excitation, and measurement, and photon collection and measurement. Both laser addressing and applied RF magnetic fields are used to achieve these tasks with the ion, and an imaging axis is set up in order to collect and measure photons.

## *6.1 State Transitions*

It is useful for experimenting to be able to drive the ion into a known initial state and to perform coherent state rotations. Initialization is achieved using optical pumping while state rotations may be performed using Rabi rotations or Adiabatic Rapid Passage.

### *6.1.1 Optical Pumping*

As discussed in Chapter 2, left and right circularly polarized light will only drive transitions with $\Delta m_j = +1 \quad \text{or} - 1$. This can be used to address all states in the cooling cycle except for one. In such a situation, the ion will absorb and emit photons until it decays to the unaddressed state where it remains. In the experiments performed in this work, an applied magnetic field $B \approx 2.4$ gauss provided a quantization axis, and a circularly polarized beam of 493 nm light aligned parallel to the quantization axis was used for optical pumping to either of the two Zeeman sublevels of the $6S_{1/2}$ ground state. This is the first step in the sequence for ion initialization. A diagram depicting optical pumping to the $6S_{1/2}$ ($m_J = -\frac{1}{2}$) ground state sublevel is shown in Fig. 6.1. The fidelity with which an ion is pumped to the unaddressed state may be reduced if the polarization is not purely $\sigma^+$ or $\sigma^-$. Thus it is

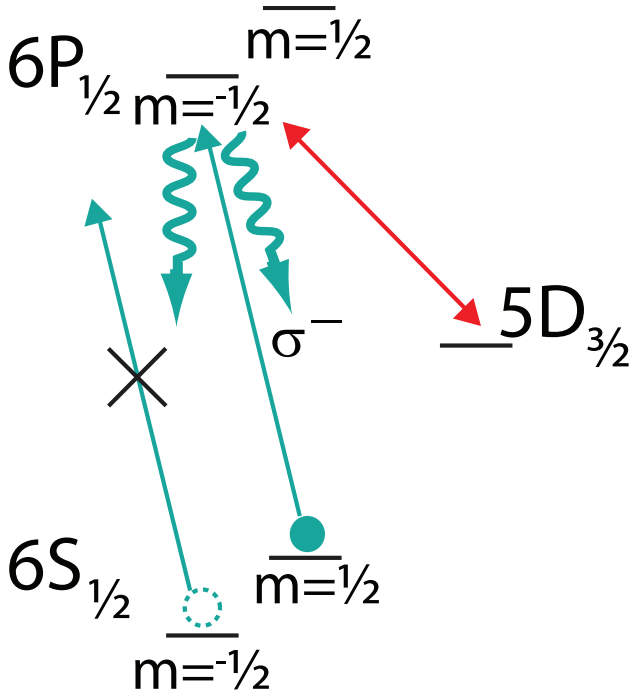


Figure 6.1: Optical Pumping to the $6S_{1/2}$ ($m_J = -\frac{1}{2}$) ground state sublevel is shown above. Since the $6S_{1/2}$ ($m_J = -\frac{1}{2}$) sublevel cannot make a $\Delta m = -1$ transition, it is not addressed by the cooling lasers and the ion population will be driven to that state.

important for the optical pumping beam to be colinear with the quantization axis so that any $\pi$-polarized component is minimized and for the polarization to either purely $\sigma^+$ or $\sigma^-$, not a linear combination of both.

### *6.1.2 Rabi Rotations*

Once the ion is known to be in one of the two Zeeman sublevels of the $6S_{1/2}$ ground state, the ion state may be rotated using an RF magnetic field resonant with the Zeeman splitting. A dedicated wire loop in the vicinity of the trap inside the vacuum chamber is used to generate the tunable RF magnetic field in order to drive magnetic dipole transitions between the Zeeman sublevels for the necessary ion state rotations. An RF synthesizer (based on a direct digital synthesis (DDS9910) chip) generates a stable sinusoidal voltage which is

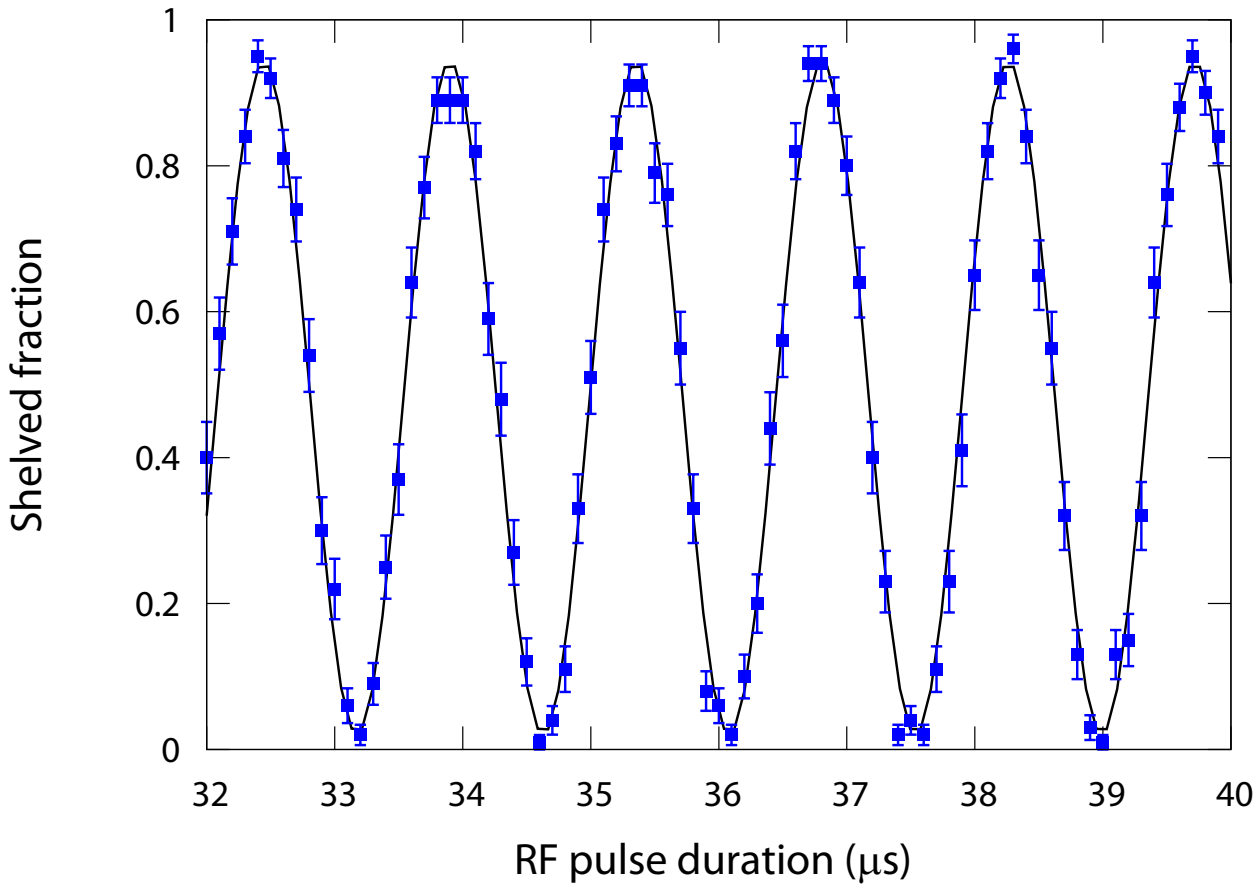


Figure 6.2: Example of Zeeman qubit rotations of the ground state. After initialization to a single Zeeman sublevel of the ground state, the RF signal is applied for the indicated time followed by $\approx 97\%$ efficient transfer of the $m_J = -\frac{1}{2}$ ground state to the $5D_{5/2}$ level. Thus, a shelving efficiency near 1 corresponds to the ion in the $m_J = -\frac{1}{2}$ ground state, while a shelving efficiency near 0 corresponds to the ion in the $m_J = +\frac{1}{2}$ ground state.

amplified and dropped over a 50 ohm RF resistor for impedance matching, producing an oscillating current in the loop. This setup allowed for ion state rotations with a tunable phase. An example of ground state Rabi oscillations is shown in Fig. 6.2. The reduction in contrast is due to imperfect optical pumping ($\approx 98\%$) and shelving efficiency ($\approx 97\%$).

Having achieved state initialization, the experiment may proceed through excitation to the measurement phase. Prior to detection, the RF magnetic field produced by the wire loop may

be used to rotate the ion state. This has the same effect as a rotation of the measurement basis. Ionic qubit state detection is accomplished by the use of a stabilized 1762 nm fiber laser to drive the "shelving" transition from the $6S_{1/2}$ ($m_J = -\frac{1}{2}$) ground state sublevel to the $5D_{5/2}$ ($m_J = -\frac{5}{2}$) metastable sublevel (lifetime $\approx$ 30 s). This may be achieved in one of two manners: (1) Rabi rotations as discussed in Chapter 2 or (2) adiabatic rapid passage [37]. Once excited to the $5D_{5/2}$ shelved state, the ion is removed from the cooling cycle and will appear "dark" while the cooling lasers are incident on the ion, whereas an unshelved ion will be "bright."

### *6.2 Imaging Setup*

Along the imaging axis in the blade trap, spontaneously emitted photons are collected through an $f/2.8$ lens while other wavelengths are extinguished by a 493 nm interference filter. The light is imaged onto a pinhole in order to spatially filter any light scattered off the trap electrodes. This is then re-imaged onto a PMT and EMCCD camera after passing through a beam splitter. An image of ions on an EMCCD camera is shown in Fig. 6.3. Photon collection occurred along a direction perpendicular to the quantization axis in the blade trap and parallel to the quantization axis in the parabolic mirror trap. The transitions of note in the experiments described in this work, $\sigma^+$, $\sigma^-$, and $\pi$, are emitted into the dipole radiation patterns $|\sigma^-\rangle = \frac{e^{+i\phi}}{\sqrt{2}}(\cos(\theta)|\hat{\theta}\rangle + i|\hat{\phi}\rangle)$, $|\sigma^-\rangle = \frac{e^{-i\phi}}{\sqrt{2}}(\cos(\theta)|\hat{\theta}\rangle - i|\hat{\phi}\rangle)$, and $|\pi\rangle = -\sin(\theta)|\hat{\theta}\rangle$ respectively. Thus, perpendicular to the quantization axis, i.e. $\theta = \frac{\pi}{2}$, $\pi$ polarized light is orthogonal to $\sigma^+$ and $\sigma^-$ polarized light which are linear. A $\lambda/2$ waveplate along the imaging axis allows for rotations of the photonic qubit. After passing through a polarizing beamsplitter (PBS), the photons are detected at one of two photomultiplier tubes (PMTs) each with quantum efficiency $\eta \approx 0.2$ (the second replacing the EMCCD camera mentioned *supra* which is only used for diagnostic purposes).

The parabolic mirror trap also uses an EMCCD camera to assist in the alignment of the optics and to directly image the ions. For the experimental work to be performed with this

trap however, the collimated light reflected from the parabolic mirror when the ion is at the focus is passed through a 455 nm interference filter to extinguish any other wavelengths and fiber coupled into a single mode fiber. The output of the fiber is passed through a $\lambda/4$ waveplate in order to convert the circularly polarized light into linearly polarized light. This is followed by a $\lambda/2$ waveplate which allows for rotations of the photonic qubit and a PBS and PMTs as above. The effects of polarization mixing due to the large angle of collection is discussed in Chapter 9.

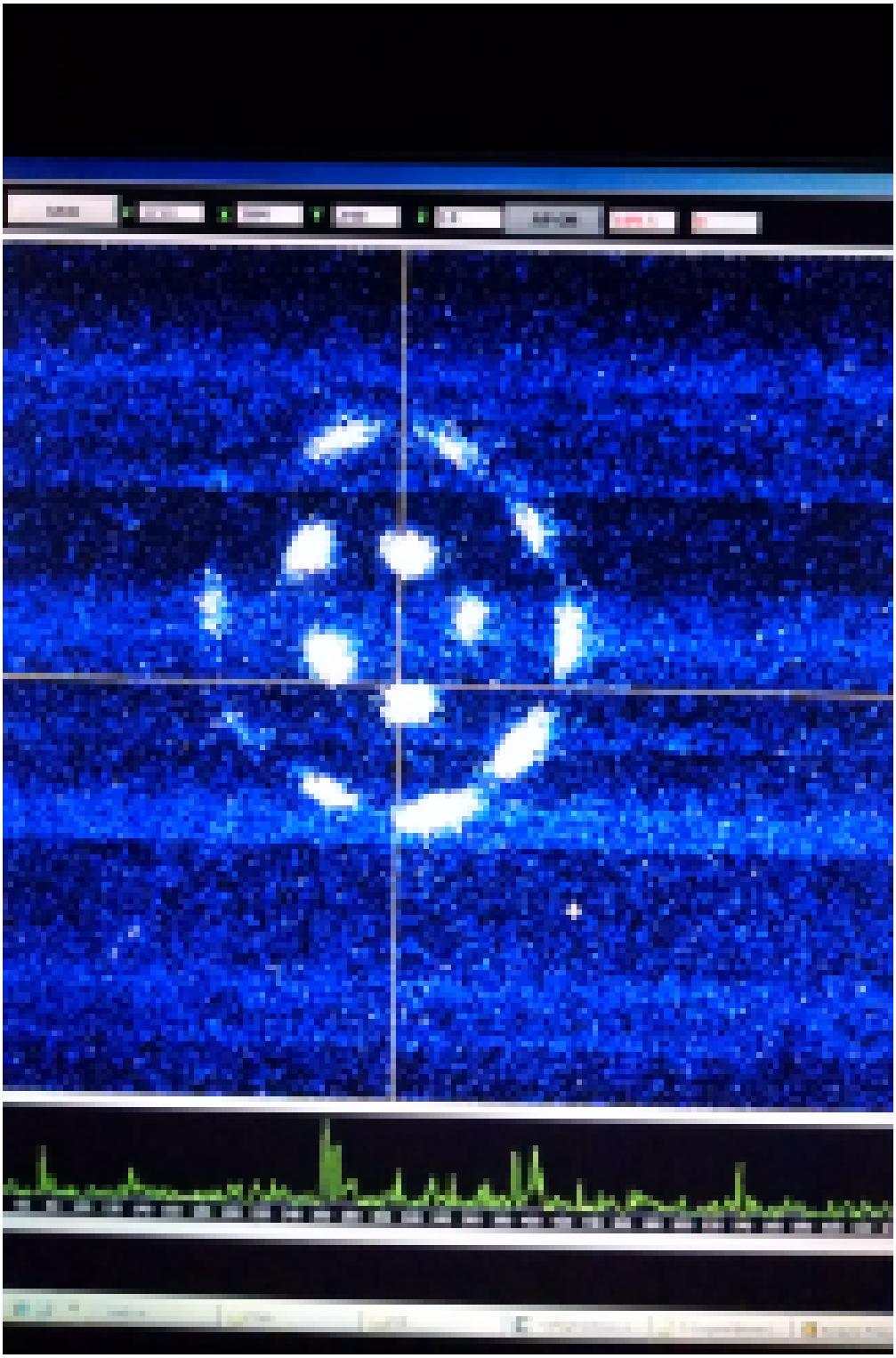

Figure 6.3: Image from an EMCCD camera of a cooled crystal of ions in the parabolic mirror trap. One can note the radial symmetry of the ion positions due to the radial symmetry of the trapping potential.

# Chapter 7

# Ba-138 $D_{5/2}$ BRANCHING RATIO AND LIFETIME MEASUREMENT

*It was a once-in-a-lifetime moment. I really can't explain it. It was crazy.*

- Anonymous

Trapped ions provide a useful physical system for a variety of experimental applications including quantum computation [34, 3], precision measurement [38, 21], and frequency standards [41]. These applications leverage the environmental isolation and long trap lifetimes provided by trapped ions to obtain long interrogation times and relatively systematic-error free methodologies. A deep and thorough understanding of atomic theory is necessary for the development and analysis of trapped ion and other atomic physics experiments. This understanding is cemented by the comparison of precisely measured atomic parameters with those calculated from atomic theory. Such comparisons provide checks on the accuracy of the atomic wavefunctions involved in theoretical calculations. Excited state lifetimes and branching fractions are readily measured and allow direct comparison with calculation results [16, 40, 36, 26]. Branching fractions of relatively short-lived metastable levels have previously been measured, for example the $^2D_{5/2}$ level of $Yb^+$ ($\tau \sim 7$ ms) [53]. Here I present a measurement of the branching fractions for decay of the much longer-lived $5D_{5/2}$ level of $Ba^+$ ($\tau \sim 30$ s). The long lifetime of the metastable state in barium introduces additional systematic effects that must be carefully considered and controlled. A discussion of these systematic effects follows the presentation of the results later in this chapter.

### *7.1 Experimental Procedure*

A single $^{138}Ba^{+}$ ion was confined in the linear Paul trap described in Chapter 4. The branching ratio of interest depicted with the relevant level structure and transitions of a $^{138}Ba^{+}$ ion are displayed in Fig. 7.1. The ion was Doppler cooled primarily on the $6S_{1/2}$

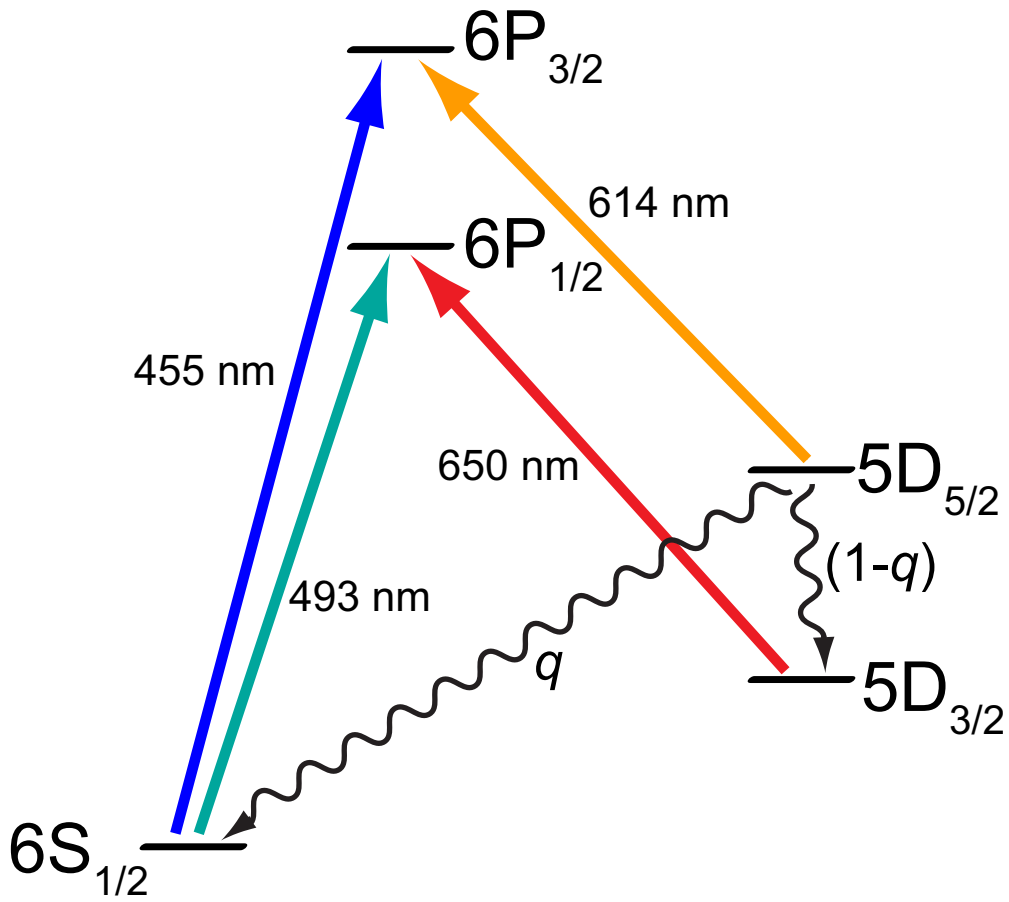


Figure 7.1: Relevant energy levels of $^{138}Ba^{+}$. Doppler cooling is done on the $6S_{1/2}$ to $6P_{1/2}$ transition with 493 nm light while 650 nm light is present to repump the $5D_{3/2}$ level. A laser at 455 nm allows us to shelve the ion in the long-lived $5D_{5/2}$ level by driving transitions between the $6S_{1/2}$ and $6P_{3/2}$ levels. A shelved ion can be returned to the cooling cycle by applying light at 614 nm. The two decay paths from the $5D_{5/2}$ level are shown. The measurement of the branching fraction to the ground state, $q$, from that level is the subject of this article.

to $6P_{1/2}$ transition with 493 nm light and 650 nm was used to repump from the long-lived $5D_{3/2}$ level ($\tau \approx 80$ s [61]) to which the $6P_{1/2}$ level decays roughly one quarter of the time. In order to excite the ion to the $5D_{5/2}$ level, a 455 nm laser was used to drive the $6S_{1/2}$ to $6P_{3/2}$ transition. Since the $5D_{5/2}$ level is long-lived and disjoint from the cooling cycle, an ion occupying that level is said to be "shelved," and the level itself is sometimes referred to as the "shelved state." The $6P_{3/2}$ level branches upon decay into the $5D_{5/2}$, $5D_{3/2}$, and $6S_{1/2}$ levels with probabilities 0.215, 0.029, and 0.756, respectively [27]. This means that in the presence of 455 nm and 650 nm light the ion will be reliably optically pumped into the shelved state. Note that, in the presence of 455 nm light alone, an ion initially in the ground state will be shelved about 89% of the time, with the remaining population transferred to the $5D_{3/2}$ level. Light at 614 nm was used to deshelve the ion, when necessary, by driving the $5D_{5/2}$ to $6P_{3/2}$ transition, which returns the ion to the cooling cycle. Mechanical shutters were used on all lasers to ensure that only the desired wavelengths of light were interacting with the ion at any given time during the experimental cycle.

The experimental cycle for the measurement of the branching fractions of the $5D_{5/2}$ level consisted of five major steps: cooling, shelving, wait for decay, re-shelving, and state detection. First, the ion was Doppler cooled for 75 ms. Next the ion was shelved to the $5D_{5/2}$ level with 65 ms of 455 nm light while the 650 nm light remained on to repump any decays to the $5D_{3/2}$ level. All light was then extinguished for a duration of 2 s, allowing the ion to decay in a few percent of the trials. Then the 455 nm beam was exposed for 30 ms in order to re-shelve any decay to the $6S_{1/2}$ ground state. Finally state detection was performed by turning on the cooling lasers, with an ion having decayed to the $5D_{3/2}$ level appearing "bright" and an ion having decayed to the $6S_{1/2}$ ground state and been reshelved or not having decayed appearing "dark." Fig. 7.2 shows a histogram of fluorescence counts with clearly distinguished bright and dark distributions. Bright and dark state discrimination was $> 99.9\%$. If the ion was found to be in the $5D_{5/2}$ level upon detection, then a deshelving pulse of 614 nm light was applied before restarting the cycle. A waveform sequence detailing the timing of the application of each laser is shown in Fig. 7.3.

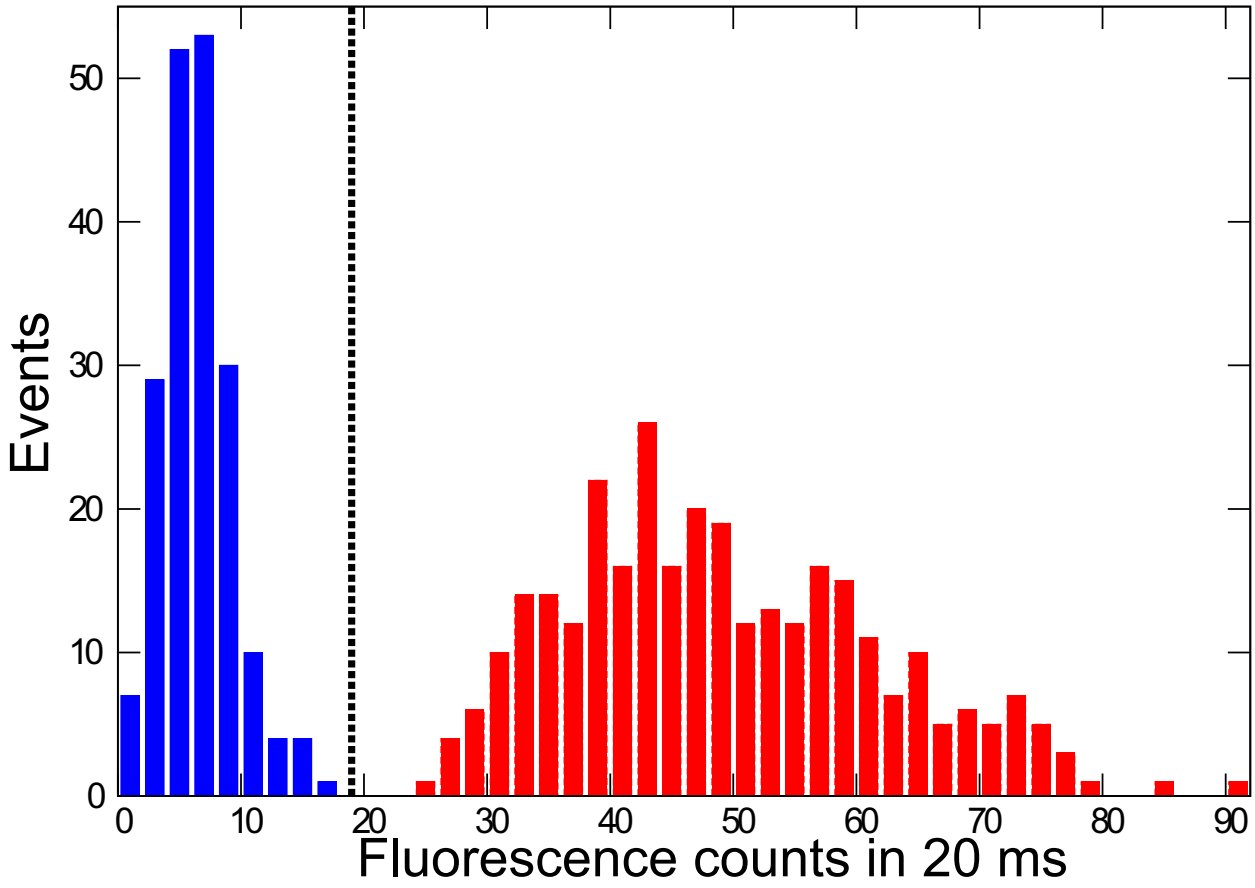


Figure 7.2: Histogram of the fluorescence counts recorded in the 500 runs comprising the 30 s wait time data point of the $5D_{5/2}$ lifetime measurement to be described later in this report. The histogram is presented here as an example demonstrating the high quality of the discrimination between the bright and dark ion states. This particular data was chosen because the number of events in the bright and dark peaks are roughly equal, making it easy to interpret visually without need for rescaling or other manipulation. The vertical dashed line shows a threshold below (equal to or above) which the run is categorized as dark (bright). Since the background (from laser scatter, room light, and PMT dark counts) does not vary significantly, the dark peak fits well to a Poisson distribution. Modeling the bright counts is complicated by drift in the cooling laser frequency over the long duration of the data acquisition. This implies that the bright distribution draws from a sum of Poisson distributions with a variety of means. Independently of how this fitting was done in detail, the probability for a false dark event (ion in the cooling cycle measured to have fluorescence below threshold) was invariably found to be $< 10^{-3}$ and the probability for a false bright event was even lower.

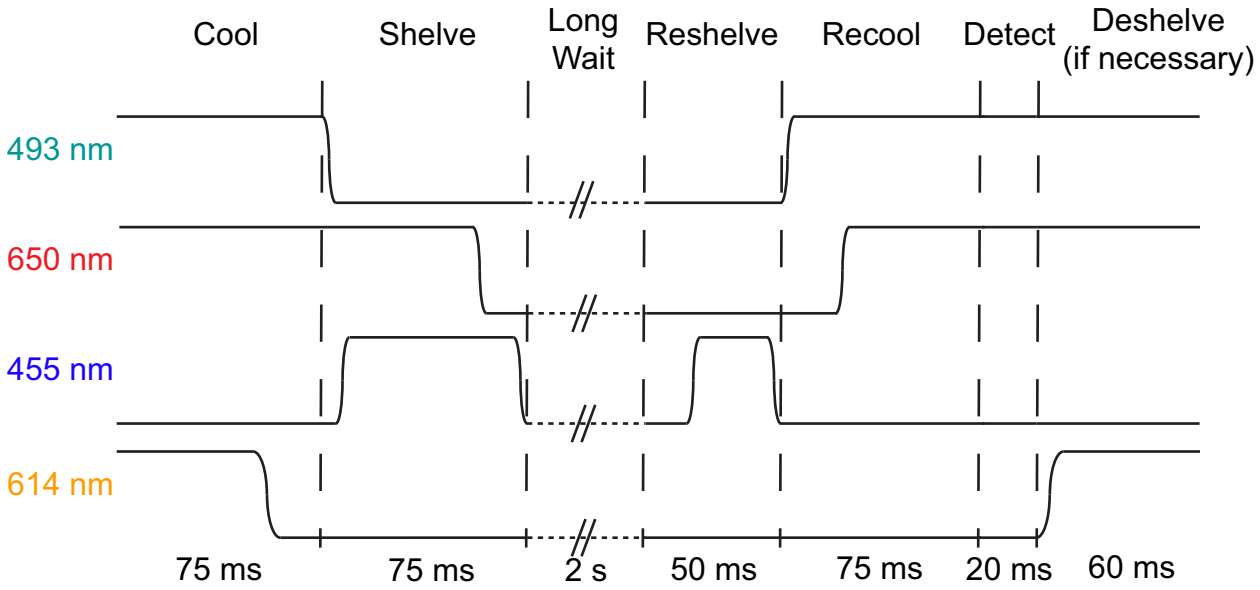


Figure 7.3: Timing sequence for application of each of the four lasers. The ion is being exposed to a given laser when the corresponding trace in the diagram is high. The duration of application of each laser is largely determined by the slow response times of the mechanical shutters and the desire to have absolute confidence in the ordering of the sequence. The operations involved are reliably completed in much shorter times than are used. The experimental cycle is detailed in the main text. Briefly, the cycle consisted of Doppler cooling, shelving with 455 nm and 650 nm light, a 2 s wait for decays from the $5D_{5/2}$ level, re-shelving of the decays to ground state with 455 nm light, detection of the resulting ion fluorescence state, and deshelving when necessary.

## *7.2 Results*

The branching fraction measurement comprised 13,000 experimental cycles like those discussed in the previous section. The probability that the ion was in the $5D_{5/2}$ level at the end of the procedure, $P_{\text{dark}}$, depends on the initial shelving efficiency, $P_{\text{sh}}$, the probability of decay from the $5D_{5/2}$ level during the wait time, $P_{\text{dec}}$, the re-shelving efficiency, $P_{\text{re-sh}}$, the branching fraction for decay into the $6S_{1/2}$ level, $q$, and the probability of a sequential decay from $5D_{5/2}$ to $5D_{3/2}$ to $6S_{1/2}$ during the wait time, $P_{\text{seq-dec}}$. Following the experimental cycle, the ion will be found to be dark in three ways: (1) the ion was shelved and subsequently did not decay $P_{\text{sh}}(1 - P_{\text{dec}})$, (2) the ion was shelved, subsequently decayed to the

ground state, and was re-shelved $P_{\text{sh}}P_{\text{dec}}qP_{\text{re-sh}}$, and (3) the ion was shelved, subsequently decayed to the $5D_{3/2}$ level, subsequently decayed to the ground state, and was reshelved $P_{\text{sh}}P_{\text{dec}}(1-q)P_{\text{seq-dec}}P_{\text{re-sh}}$. Adding these together, we find $P_{\text{dark}}$ to be

$$\begin{aligned} P_{\text{dark}} &= P_{\text{sh}}(1-P_{\text{dec}}) + P_{\text{sh}}\ P_{\text{dec}}\ q\ P_{\text{re-sh}} \\ &\quad + P_{\text{sh}}\ P_{\text{dec}}(1-q)P_{\text{seq-dec}}\ P_{\text{re-sh}}. \end{aligned} \tag{7.1}$$

Solving this equation for $q$ shows how the branching fraction depends on all the quantities to be measured,

$$q = \frac{P_{\text{dark}} - P_{\text{sh}}\left[1 - P_{\text{dec}}(1 - P_{\text{re-sh}}\ P_{\text{seq-dec}})\right]}{P_{\text{sh}}\ P_{\text{dec}}\ P_{\text{re-sh}}(1 - P_{\text{seq-dec}})}. \tag{7.2}$$

In order to extract the branching fractions from the data, we must independently measure each of these probabilities. To measure $P_{\text{sh}}$ and $P_{\text{re-sh}}$, we interleaved measurements of the shelving efficiency of an ion initially in the ground state both with the 650 nm laser unshuttered and shuttered with every 100 branching fraction cycles. Based on these measurements we observed no evidence of variation in the shelving efficiency which allowed us to consolidate all the data taken into a single set. These measurements yield the values of $P_{\text{sh}}$ and $P_{\text{re-sh}}$ to be 0.999 49(42) and 0.888 7(16), respectively. We also independently measured the fraction of the time the ion decayed from the $5D_{5/2}$ level during the 2 s wait time by using the same procedure outlined in the previous section, but without the re-shelving pulse. This measurement finds $P_{\text{dec}} = 0.0654(22)$ and also provided the first data point in the $5D_{5/2}$ lifetime measurement discussed below. The probability of the sequential decay, $P_{\text{seq-dec}}$, is small enough that an estimate based on the lifetime of the $5D_{3/2}$ level suffices to address the effect. We estimate that on average the decays to the $5D_{3/2}$ level reside there for one second before the fluorescence state is measured, which, using the level's 79.8 s lifetime [61], implies that $P_{\text{seq-dec}} = 0.012(6)$. We additionally correct for a slight bias toward "bright" counts due to decays of the shelved ion that occur during the 75 ms of cooling before detection, resulting in an average of slightly less than three extra "bright" counts per 1000 cycles. After this correction, we find the shelved fraction to be $P_{\text{dark}} = 0.9836(12)$. Putting all these

measurements together, we find the branching fraction for decay of the $5D_{5/2}$ level to the $6S_{1/2}$ level to be $q = 0.850(25)$ where the error is statistical, based on propagation of the binomial errors in all the measurements discussed above.

The analysis above makes the unjustified assumption that in the $(1 - P_{\mathrm{sh}}) = 0.05\%$ of the cycles in which the ion failed to be shelved initially, it was always found to be bright upon fluorescence detection. It is reasonable to assume that whenever the ion was not shelved before the wait time, it must have resided either in the $5D_{3/2}$ level or the ground state, but we do not have a simple means of discerning which. If (when not initially shelved) the ion always resided in the $5D_{3/2}$ level at the onset of the wait time, then the analysis from the previous paragraph is valid, since the ion would indeed be found to be bright upon detection. If, however, the ion always resided in the ground state as the wait time began, then the re-shelving pulse would have transferred the ion to the $5D_{5/2}$ level in 89% of those trials. Adjusting the analysis to assume that the ion was always in the ground state when the initial shelving pulse failed lowers the extracted value of the branching fraction to $q = 0.842(24)$. The reality is likely that when the initial shelving pulse failed, some population resided in both the $5D_{3/2}$ and $6S_{1/2}$ levels. Therefore, including this effect as a systematic uncertainty, we report the measured value of the branching fraction for the decay of the $5D_{5/2}$ level into the $6S_{1/2}$ ground state to be $q = 0.846(25)_{\mathrm{stat}}(4)_{\mathrm{sys}}$.

Both in order to extract transition rates from our branching fraction measurement and to help estimate systematic effects, we measured the lifetime of the $5D_{5/2}$ level by counting the number of decays with wait times of 2 s, 5 s, 10 s, and 30 s for 6000, 1000, 1000, and 500 experimental cycles respectively. The lifetime data is shown in Fig. 7.4, along with a line of best fit for the logarithm of the shelved fraction, $f_{\mathrm{sh}}$, versus the wait time. The only fit parameter is the lifetime $\tau = 31.1(0.9)$ s where the error is statistical.

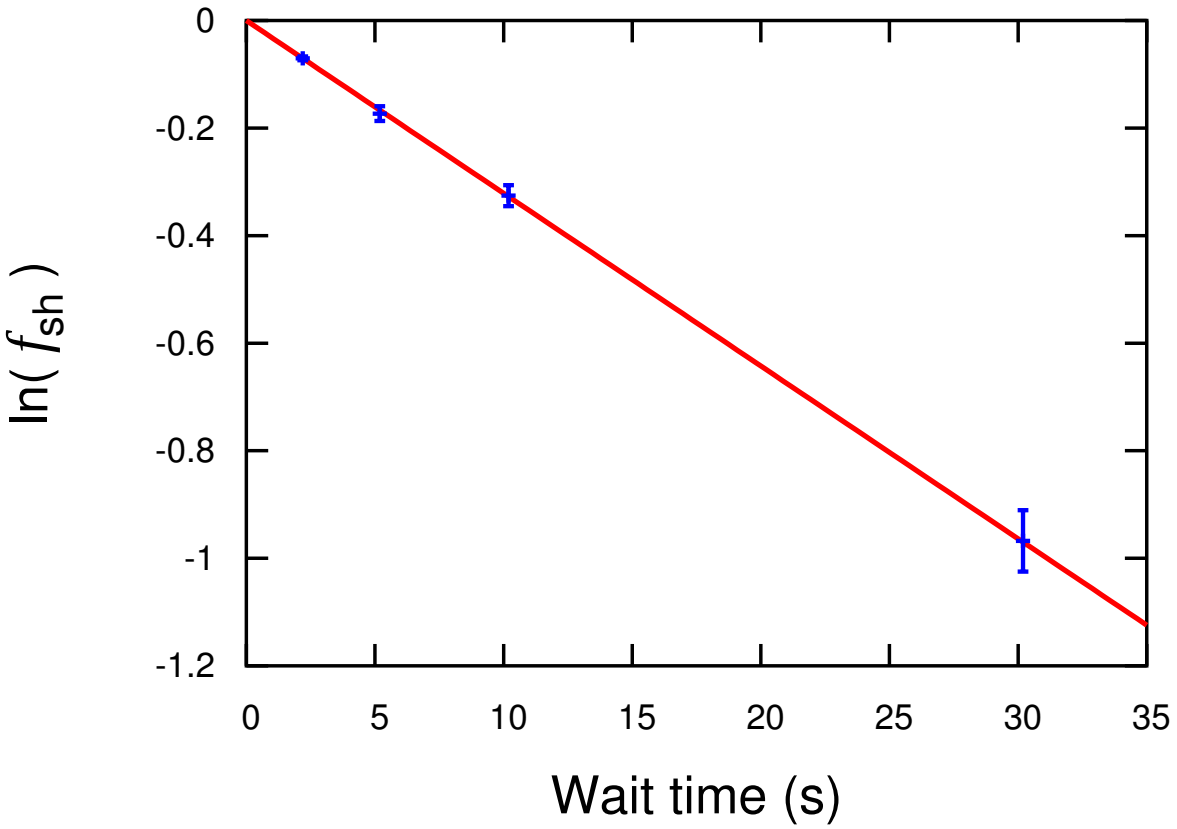


Figure 7.4: The natural logarithm of the fraction of trials in which the ion remained shelved, $f_{\mathrm{sh}}$, versus the duration that the ion spent in the $5D_{5/2}$ shelved state is plotted. The error bars on the four data points are statistical based on the binomial distribution. The red line is a linear fit through the origin with slope its only fit parameter. The fit implies the lifetime to be $\tau = 31.1(0.9)$ s.

In order to more directly compare our experimental result with theoretical predictions, we calculate transition rates from our measured lifetime and branching fraction for the decay from the $5D_{5/2}$ level into the $6S_{1/2}$ ground state. Using theoretical calculations for the relevant reduced matrix elements of the electric quadrupole (E2) and magnetic dipole (M1)

operators, we find transition rates predicted by several theorists using the following equations:

$$A_{ki}^{E2} = \frac{1}{4\pi\epsilon_0}\frac{1}{15}\frac{\omega^5}{\hbar c^5}\frac{1}{g_k}\left|S_{ki}\right|^2 \qquad \text{where } S_{ki} = \left|\langle k||\mathrm{E2}||i\rangle\right| \tag{7.3}$$

$$A_{ki}^{M1} = \frac{1}{4\pi\epsilon_0}\frac{4\omega^3}{3\hbar c^3}\frac{1}{g_k}\left|S_{ki}\right|^2 \qquad \text{where } S_{ki} = \left|\langle k||\mathrm{M1}||i\rangle\right|. \tag{7.4}$$

Here $\hbar\omega$ is the difference in energy between states $i$ and $k$, and $g_k$ is the degeneracy of the upper state, $k$ [50]. Our results and the transition rates predicted by theory are presented in Table 7.1. While the results presented here are insufficiently precise to distinguish between the selected set of theoretical calculations, an increase in precision of about a factor of three on the transition rate from the $5D_{5/2}$ level to the $6S_{1/2}$ level would suffice to begin rejecting some calculations.

The major systematic effects of experiments involving long dwell times in metastable states are effects related to the presence of background gas, leakage light, and ion heating. At our

Table 7.1: Comparison of theoretical predictions and our experimental results

| Transition | Present Work | | Previous Theory |
|---|---|---|---|
| | Relative Strength | $A_{ki}(\mathrm{s}^{-1})$ | $A_{ki}(\mathrm{s}^{-1})$ |
| $5D_{5/2} \rightarrow 6S_{1/2}$ | 0.846(25) | 0.0271(15) | 0.02692[45] |
| | | | 0.02693‡[19] |
| | | | 0.02607[20] |
| | | | 0.02800[46] |
| $5D_{5/2} \rightarrow 5D_{3/2}$ | 0.154(25) | 0.00494(83) | 0.005470[45] |
| | | | 0.005543[19] |
| | | | 0.005573[20] |
| | | | 0.005499‡[46] |

‡ These values do not appear explicitly in the references, but were deduced based on the $5D_{5/2}$ lifetimes quoted therein.

trap pressure of $< 7 \times 10^{-12}$ Torr, the quenching effect due to the presence of background gas is nearly negligible. Based on quenching rates for the $5D_{5/2}$ level found in literature [29, 61], background gas collisions at our estimated trap pressure reduce the measured lifetime by 0.1 s. Therefore we report the lifetime of the $5D_{5/2}$ level of $^{138}Ba^{+}$ to be $\tau = 31.2(0.9)$ s. The use of mechanical shutters ensured that no unwanted laser light impinged on the ion during the long dwell time. A number of mechanisms, not all of which are fully understood, contribute to heating of ions in Paul traps [55]. Thus it could be supposed that the long duration without cooling involved in each experimental cycle of the branching ratio and lifetime measurements could result in ions so hot that they would not reliably appear bright when the cooling lasers are finally exposed for detection. However, ion heating resulting in false dark readings was found to be a negligible effect. We ran 1000 cycles of an experimental sequence in which the ion spent the same duration in the absence of the cooling lasers as it did in the branching ratio measurement, but in the ground state instead of the $D_{5/2}$ level. Ion heating is not expected to depend on electronic state, so the heating in this test should faithfully reproduce the heating in the branching ratio measurement. After the duration spent in the dark, the cooling lasers were turned on and the ion was measured to be bright in every trial. Furthermore, looking at the distribution of the bright counts, we see no change in our ability to discriminate bright ions from dark ones due to heating during the long dwell time.

### *7.3 Conclusions*

In conclusion, this is the first experimental measurement of the branching fractions from the $5D_{5/2}$ level of Ba II, finding that the level decays to the ground state with probability $0.846(25)_{\mathrm{stat}}(4)_{\mathrm{sys}}$. In addition, this measurement of the $5D_{5/2}$ lifetime, $\tau = 31.2(0.9)$ s, improves on the previous best measurement, $\tau = 32.3(2.6)$ s [61], reducing the uncertainty by almost a factor of three. Together these measurements provide the first experimentally determined values for the rates of the $5D_{5/2}$ to $6S_{1/2}$ and $5D_{5/2}$ to $5D_{3/2}$ transitions. The values for those transition rates are found to be 0.0271(15) $s^{-1}$ and 0.00494(83) $s^{-1}$, respec-

tively. Good agreement between the measured values and recent theoretical predictions was found.

# Chapter 8

# Ba-138 ION-PHOTON ENTANGLEMENT

The generation of entanglement is an essential tool for the realization of scalable quantum computing and long distance quantum communication. The ability to entangle a photon for reliable long-range quantum communication and another particle with a long-term quantum memory would allow for the construction of such a scalable quantum network. Large strides have been made towards this in many different physical media. Entanglement and the means for communication have been demonstrated most recently in quantum dots [12, 15, 25], nitrogen vacancy centers in diamond [54, 35, 6], neutral atoms [59, 42], atomic ensembles [28, 8], superconducting qubits [13, 51, 5], and ions [31, 7, 52]. This chapter reports on entanglement and Bell inequality violation in a system of a photon and a $^{138}Ba^{+}$ion. This system is particularly well suited for quantum computation [33] and communication because its transitions have relatively long wavelengths making them more suitable for long-range fiber optic transmission.

In this experiment, entanglement was produced by spontaneous emission of a photon from an excited $^{138}Ba^{+}$ion with multiple decay channels similar to [7]. The two entangled qubits were the Zeeman sublevels of the $6S_{1/2}$ ground state of the ion and the emitted photon's polarization. Entanglement was verified by performing state detection on each qubit in two non-orthogonal bases.

## *8.1 Theoretical Considerations*

As discussed in Chapter 1, the famous 1935 paper by Einstein, Podolsky, and Rosen concluded that the description of reality given by the wave function in Quantum Mechanics

was not complete [14]. This was based on the observation that entangled quantum systems require nature to be nonlocal or non-real. However in 1964, John Bell demonstrated that the principles of locality and realism assumed by Einstein, Podolsky, and Rosen in their paper were inconsistent with the predictions of Quantum Mechanics [2]. The mathematical formalism he presented gave an inequality that must be obeyed by any theory satisfying local realism. Many experimental tests have shown violations of some form of the Bell inequality [58, 43, 17, 30, 56, 1, 23, 57], including closing individual loopholes separately, and some recently having simultaneously closed both of the major loopholes (the detection, or "fair sampling," loophole and the locality loophole) associated with such a measurement [18, 47, 24].

In this experiment, a violation of the Bell inequality of the form suggested by Clauser, Horne, Shimony, and Holt (CHSH) is demonstrated [11]. Experimental tests of the CHSH inequality have three requirements: (1) repeated creation of entangled pairs of qubits, (2) the ability to rotate each qubit independently through a polar angle $\theta_a$, $\theta_b$ on the Bloch sphere, and (3) state measurement of each qubit. CHSH show that all theories satisfying local realism must obey the following inequality:

$$S = |P(\theta_a, \theta_b) - P(\theta_a, \theta_{b'})| + |P(\theta_{a'}, \theta_b) + P(\theta_{a'}, \theta_{b'})| \leq 2 \tag{8.1}$$

where

$$\begin{aligned} P(\theta_a, \theta_b) = f_{00}(\theta_a, \theta_b) + f_{11}(\theta_a, \theta_b) \\ - f_{01}(\theta_a, \theta_b) - f_{10}(\theta_a, \theta_b) \end{aligned} \tag{8.2}$$

is a correlation function measurement, and $f_{\alpha\beta}(\theta_a, \theta_b)$ is the fraction of the total events in which qubits A and B are found to be in states denoted by $\alpha$ and $\beta$ respectively following rotations of the qubits by polar angles $\theta_a$ and $\theta_b$ respectively on the Bloch sphere.

As discussed in Chapter 1, Quantum Mechanics predicts that the CHSH inequality can be violated for particular entangled states and measurements. Maximum violation of $S = 2\sqrt{2}$ occurs for $\theta_{a,a'} = 0,\ \pi/2$ and $\theta_{b,b'} = \pi/4,\ 3\pi/4$ when the entangled state is one of the four Bell states found in Eqs. 1.4, 1.5, 1.6, and 1.7.

The Bell signal measured in an experiment can be reduced, however, by infidelity in the state that is produced. A measure of entanglement fidelity can be found by calculating a state's overlap with the appropriate maximally entangled Bell state [4]. Thus with respect to the particular Bell state $|\Phi^+\rangle = \frac{1}{\sqrt{2}}(|0\rangle_A|0\rangle_B + |1\rangle_A|1\rangle_B)$, the fidelity is given by the expectation value of the density matrix ($\rho$) in the Bell state:

$$F = \langle\Phi^+|\rho|\Phi^+\rangle = \frac{1}{2}(\rho_{11} + \rho_{44} + \rho_{14} + \rho_{41}) \tag{8.3}$$

where $\rho$ is given in the computational basis, $\{|00\rangle, |01\rangle, |10\rangle, |11\rangle\}$. The first two density matrix elements are just the correlation probabilities of detecting the states $|0\rangle_A$ with $|0\rangle_B$ and $|1\rangle_A$ with $|1\rangle_B$. These correlation probabilities ($\rho_{ii}$) are given by the probability of detecting qubit $B$ in the state corresponding to $i$ multiplied by the conditional probability of detecting qubit $A$ in the state corresponding to $i$ given that the state of qubit $B$ is the state corresponding to $i$. The second two elements can be determined by rotating each qubit's measurement basis by the polar angle $\frac{\pi}{2}$ on the Bloch sphere. Then $\rho' = R_{\frac{\pi}{2}}(\phi)\rho R^\dagger_{\frac{\pi}{2}}(\phi)$, where $R_{\frac{\pi}{2}}(\phi)$ is the $\frac{\pi}{2}$ polar rotation operator with relative phase $\phi$. With $\phi$ set to zero, one finds that

$$\begin{aligned} \rho_{14} + \rho_{41} &= \rho'_{11} + \rho'_{44} - \rho'_{22} - \rho'_{33} - \rho_{23} - \rho_{32} \\ &\geq \rho'_{11} + \rho'_{44} - \rho'_{22} - \rho'_{33} - 2\sqrt{\rho_{22}\rho_{33}} \end{aligned} \tag{8.4}$$

Thus we find a lower bound for the fidelity expressed in terms of the correlation probabilities in the original and rotated bases:

$$F \geq \frac{1}{2}(\rho_{11} + \rho_{44} - 2\sqrt{\rho_{22}\rho_{33}} + \rho'_{11} + \rho'_{44} - \rho'_{22} - \rho'_{33}) \tag{8.5}$$

One also finds the expected Bell signal for the angles of maximal violation from the density matrix in the unrotated and rotated bases (with the relative phase of the rotation $\phi = 0$) of:

$$S = \sqrt{2}(\rho_{11} + \rho_{44} - \rho_{22} - \rho_{33} + \rho'_{11} + \rho'_{44} - \rho'_{22} - \rho'_{33}) \tag{8.6}$$

### *8.2 Experimental Procedure*

The experimental cycle, resulting states, and the energy level diagram for $^{138}Ba^{+}$are detailed in Fig. 8.2. The experimental cycle ($\approx$ 17 kHz rep rate) consisted of four major steps. First the ion was Doppler cooled for 30 $\mu$s. Next the ion was pumped to the $6S_{1/2}$ ($m_J = -\frac{1}{2}$) ground state sublevel with 10 $\mu$s of the circularly polarized optical pumping beam. State initialization was completed by following the optical pumping with a resonant RF $\pi$-pulse to transfer the ion state to $6S_{1/2}$ ($m_J = +\frac{1}{2}$). Finally the ion was weakly excited (excitation probability $\approx$ 20%) to the $6P_{1/2}$ ($m_J = -\frac{1}{2}$) sublevel (lifetime $\approx$ 8 ns [39]) with a 20 ns exposure to the optical pumping beam. This was followed by photon- and ion-state detection. The photons were detected by the PMTs inside a detection window of 20 ns, delayed somewhat from the excitation pulse. The excitation pulse length, detection window, and its delay were optimized to reduce background counts and double excitations while maintaining a reasonable experimental rate. Following a single photon detection, the ion state was determined by a shelving pulse followed by Doppler cooling. "Dark" state detection efficiency was $\approx$ 97% limited by the shelving efficiency, and "bright" state detection efficiency was $>$ 99%. A schematic depicting the lasers addressing the ion and the imaging axis is shown in Fig. 8.1.

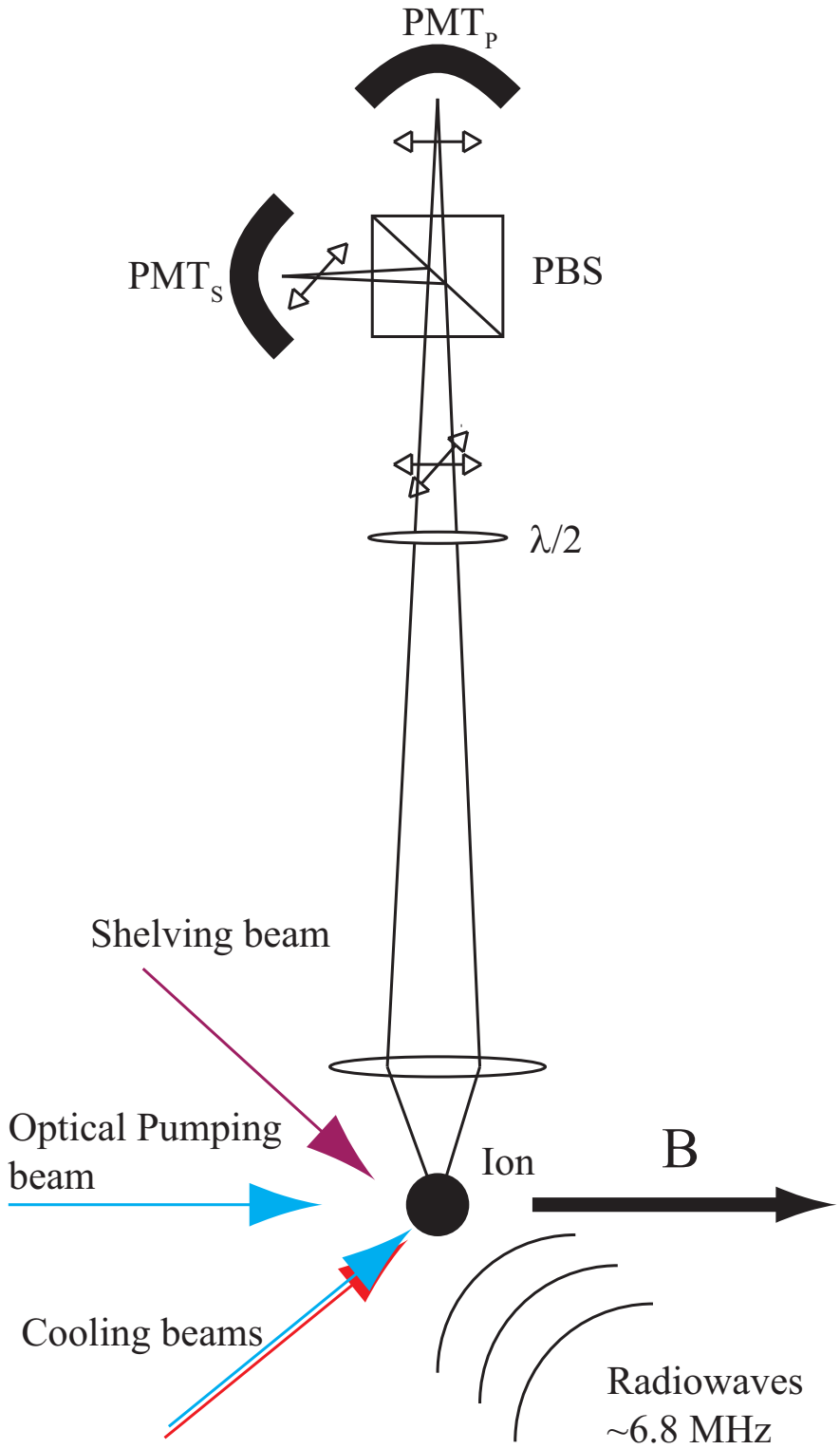


Figure 8.1: A diagram depicting the laser and imaging setup for the experiment.

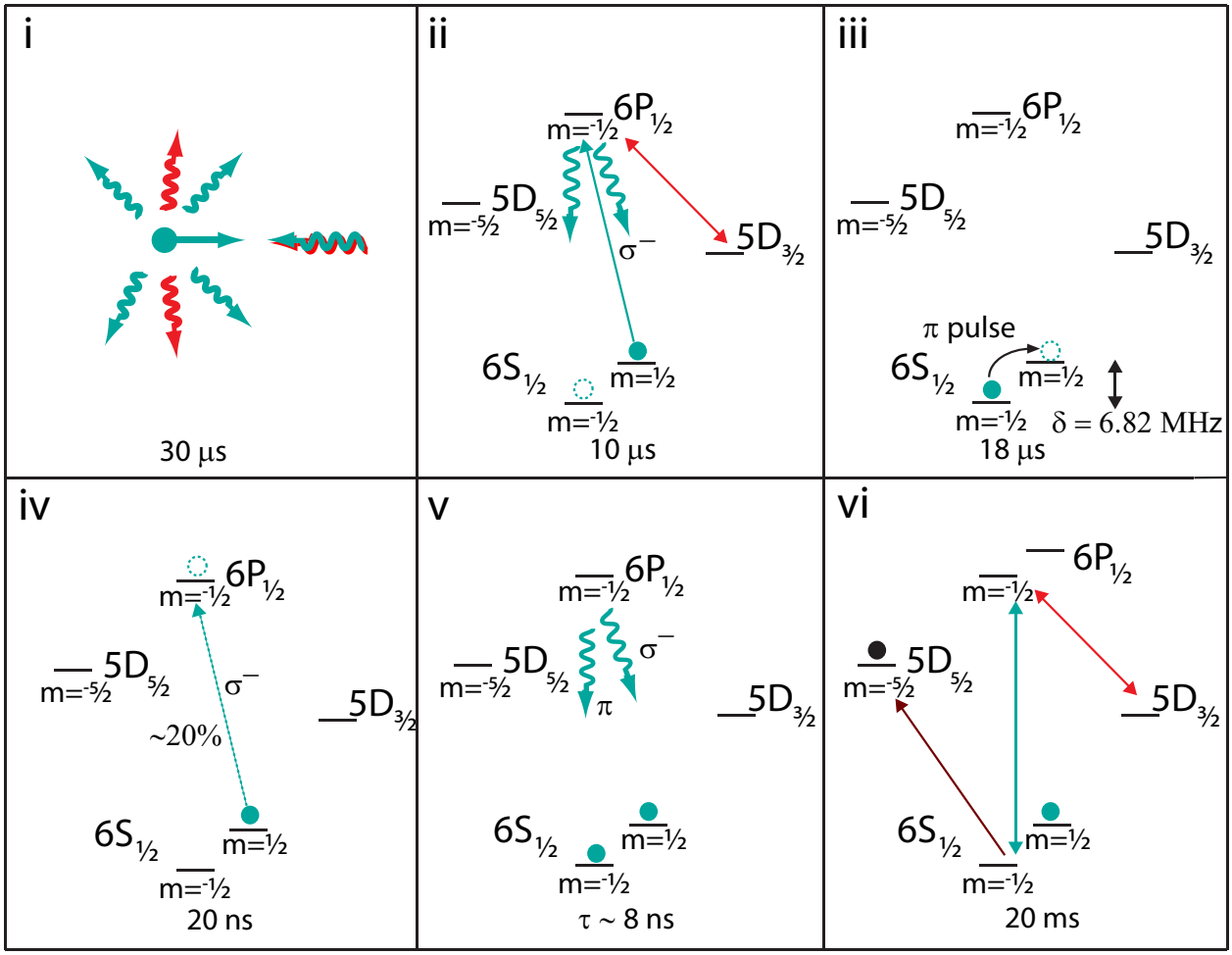


Figure 8.2: Experimental procedure: (i) the ion is Doppler cooled for 30 $\mu$s by 493 nm and 650 nm beams; (ii) state initialization is performed with 10 $\mu$s of optical pumping by a $\sigma^-$-polarized 493 nm beam followed by (iii) an 18 $\mu$s RF $\pi$-pulse resonant with the 6.82 MHz ground state separation; (iv) the ion is weakly excited with the $\sigma^-$-polarized beam; (v) the excited ion decays emitting a $\sigma^-$-polarized or $\pi$-polarized photon, resulting in the corresponding ground state sublevel, and (vi) ion detection is performed using the 1762 nm shelving beam, followed by turning on the cooling lasers.

The resultant entangled state from the spontaneous decay of the ion is $\frac{1}{\sqrt{2}}|\sigma^- \uparrow\rangle + \frac{1}{\sqrt{2}}|\pi \downarrow\rangle$ as it decays to either the $6S_{1/2}$ ($m_J = +\frac{1}{2}$) or $6S_{1/2}$ ($m_J = -\frac{1}{2}$) sublevel while emitting either a $\sigma^-$ or $\pi$ photon respectively with equal probability. However, along the imaging axis, the radiation patterns of the two polarizations differ by a factor of two. Thus the ideal measured

state is $\frac{1}{\sqrt{3}}|\sigma^- \uparrow\rangle + \sqrt{\frac{2}{3}}|\pi \downarrow\rangle$ whose overlap with a Bell state is 0.97.

We first measured the correlation between the ionic and photonic qubits by varying the photonic measurement basis with the $\lambda/2$ waveplate. Without rotating the ionic qubit, the state probabilities are proportional to $\sin^2(\frac{\theta_{photon}}{2})$ or $\cos^2(\frac{\theta_{photon}}{2})$, thus correlation fringes are produced with varying $\theta_{photon}$. At each waveplate setting, 100 runs were taken, and the conditional probabilities were plotted in Fig. 8.3 (i). At the rotation angle corresponding to maximum correlation, 1000 runs were taken for better statistics in the fidelity calculation.

Then to verify entanglement, the ionic and photonic qubits were both rotated by $\frac{\pi}{2}$ on the Bloch sphere, and the correlation was measured while varying the phase of the ionic qubit rotation, $\phi_I$. The relative phase of the ionic versus photonic qubit rotations is given by $\phi = \delta\tau + \phi_I$, where $\delta = 2\pi(6.82 \text{ MHz})$ is the ground state Zeeman splitting and $\tau$ is the time delay between emission of the photon and application of the ionic qubit rotation. If one assumes that $\delta\tau$ is constant, then varying $\phi_I$ will produce correlation fringes since the state probabilities are proportional to $1 \pm \cos\phi$. At each $\phi_I$ setting, 500 runs were taken, and the conditional probabilities were plotted in Fig. 8.3 (ii). At the maximum correlation, 2000 runs were taken for better statistics in the fidelity calculation. Following these measurements, a CHSH measurement was made with a relative phase $\phi = 0$ using those rotations resulting in a maximal violation of Eq. 8.1.

The entanglement generation rate depends on the probability of success $P$ of a single experimental run which relies on the excitation probability and the probability of detecting the spontaneously emitted photon. Given an excitation probability ($P_{exc} \approx 0.2$) along with the branching ratio to the ground state ($f = 0.75$), the quantum efficiency of the PMTs ($\eta \approx 0.2$), fraction of solid angle of light collection ($\frac{\Delta\Omega}{4\pi} \approx 0.02$), fraction of photons within PMT detection window ($f_{gate} \approx 0.8$), and the transmission losses ($T \approx 0.3$) through the imaging optics including an interference filter with 50% transmission, we expect the exper-

imental entanglement generation rate to be $R = P(17\text{ kHz}) = P_{exc} f \eta(\frac{\Delta\Omega}{4\pi}) f_{gate} T(17\text{ kHz}) = (0.2)(0.75)(0.2)(0.02)(0.8)(0.3)(17\text{ kHz}) = 2.5$ Hz which agrees well with our results.

### *8.3 Results*

The correlation fringes in the measured conditional probabilities of the photonic and ionic qubit states are plotted in Fig. 8.3. We find a maximal correlation of $P(\text{P}|\text{bright}) = 0.05 \pm 0.01$, $P(\text{P}|\text{dark}) = 0.95 \pm 0.01$, $P(\text{S}|\text{bright}) = 0.97 \pm 0.01$, and $P(\text{S}|\text{dark}) = 0.03 \pm 0.01$ for the unrotated bases and $P(\text{P}|\text{bright}) = 0.12 \pm 0.01$, $P(\text{P}|\text{dark}) = 0.88 \pm 0.01$, $P(\text{S}|\text{bright}) = 0.88 \pm 0.01$, and $P(\text{S}|\text{dark}) = 0.12 \pm 0.01$ for the rotated bases where the errors given are statistical for 1000 and 2000 successful trials, respectively. The correlations in the rotated basis are weaker largely due to timing jitter in the application of the ion state rotation. From this we use Eq. 8.5 to calculate the entanglement fidelity to be $F \geq 0.84 \pm 0.01$, which clearly exceeds the limit of $F > 0.5$ for entanglement [44].

The CHSH measurement was made using the maximally violating qubit rotation angles $\theta_{a,a'} = 0, \frac{\pi}{2}$ and $\theta_{b,b'} = \frac{\pi}{4}, \frac{3\pi}{4}$. The four correlations were measured in two ways: first using the $a, a'$ rotations for the ion qubit, and second using the $a, a'$ rotations for the photonic qubit. 2000 successful entanglement events make up each correlation measurement. From these measurements, we find a Bell signal of $S = 2.293 \pm 0.036$ for the first case and $S = 2.303 \pm 0.036$ for the second case. The errors are statistical and the Bell signal exceeds 2 by over eight standard deviations. A summary of these results is displayed in Table 8.1. Note that based on the fidelity of the entangled state, we use Eq. 8.6 to calculate an expected Bell signal to be $S = 2.373 \pm 0.027$.

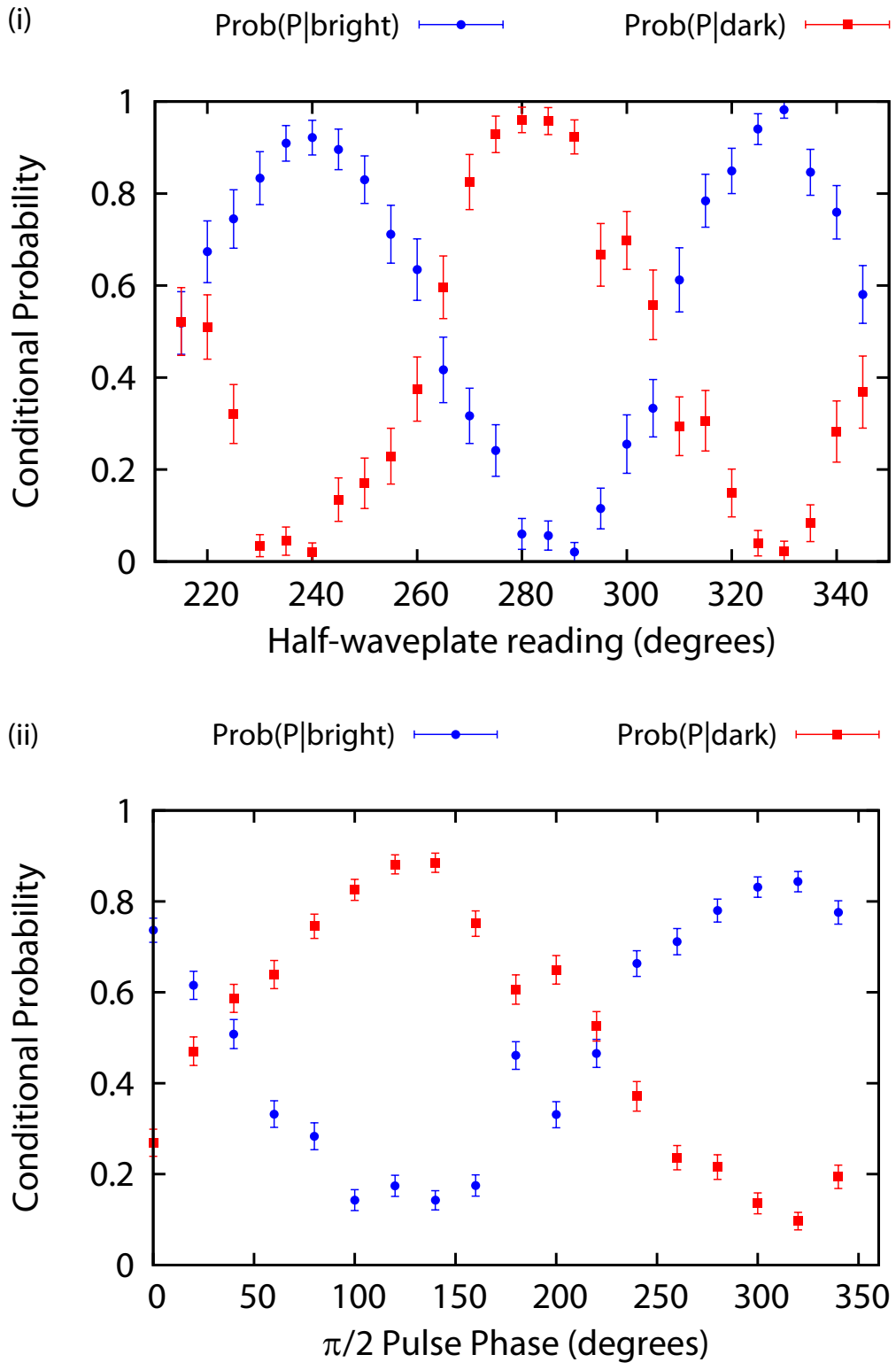


Figure 8.3: Measured conditional probabilities $P(\mathrm{P}|\mathrm{bright})$ and $P(\mathrm{P}|\mathrm{dark})$ (i) as a function of the photon qubit measurement basis angle by rotating the half-waveplate while leaving the ion qubit unrotated, and (ii) versus the ion-qubit phase, $\phi_I$, between the rotations for rotation of each qubit by a polar angle of $\frac{\pi}{2}$.

Table 8.1: Correlation function measurements and calculated Bell Signals

| $\theta_{ion}$ | $\theta_{photon}$ | $P(\theta_{ion}, \theta_{photon})$ |
|---|---|---|
| $0$ | $\frac{\pi}{4}$ | $0.549$ |
| $0$ | $\frac{3\pi}{4}$ | $-0.607$ |
| $\frac{\pi}{2}$ | $\frac{\pi}{4}$ | $0.621$ |
| $\frac{\pi}{2}$ | $\frac{3\pi}{4}$ | $0.516$ |
| | $S = 2.293 \pm 0.036$ | |
| $\frac{\pi}{4}$ | $0$ | $0.654$ |
| $\frac{3\pi}{4}$ | $0$ | $-0.579$ |
| $\frac{\pi}{4}$ | $\frac{\pi}{2}$ | $0.542$ |
| $\frac{3\pi}{4}$ | $\frac{\pi}{2}$ | $0.528$ |
| | $S = 2.303 \pm 0.036$ | |

The fidelity and Bell signal are reduced by several factors. Multiple excitations (5%), imperfect rotation of the ionic qubit due to different arrival times of photons within the 20 ns PMT detection window (3%), mixing of photon polarizations (0.5%), background and dark counts (3–5%), imperfect PBS (4%), and magnetic field fluctuations (6%). The reductions in fidelity due to multiple excitations, imperfect rotation, background counts, and imperfect PBS may be eliminated by utilizing ultrafast pulses in an ion-ion entanglement scheme like that described in Chapter 1.

# Chapter 9

# ION-PHOTON CORRELATIONS IN THE PARABOLIC MIRROR TRAP AND FUTURE DIRECTIONS

## *9.1 Entanglement Scheme Utilizing Ultrafast 455 nm Pulses*

In order to utilize the ultrafast 455 nm pulses and leverage the large solid angle of light collection of the parabolic mirror trap, a slightly different ion-photon entanglement scheme is used. Due to polarization mixing, it is optimal for the two possible polarization states of the emitted photon to be $\sigma^+$ and $\sigma^-$. To achieve this, the ion is excited from an equal superposition of the $6S_{1/2}$ ($m_J = +\frac{1}{2}$) and $6S_{1/2}$ ($m_J = -\frac{1}{2}$) sublevels with a single $\pi$-polarized 455 nm pulse. The excited state is thus an equal superposition of the $6P_{3/2}$ ($m_J = +\frac{1}{2}$) and $6P_{3/2}$ ($m_J = -\frac{1}{2}$) sublevels and has four possible decay paths to the ground state. The resultant entangled state from the spontaneous decay of the ion is

$$\Psi = \frac{1}{2}|\sigma^- \uparrow\rangle + \frac{1}{2}|\pi \uparrow\rangle + \frac{1}{2}|\sigma^+ \downarrow\rangle + \frac{1}{2}|\pi \downarrow\rangle \tag{9.1}$$

as it decays to either the $6S_{1/2}$ ($m_J = +\frac{1}{2}$) or $6S_{1/2}$ ($m_J = -\frac{1}{2}$) sublevel while emitting a $\sigma^+$, $\sigma^-$, or $\pi$ photon with equal probability for each of the four corresponding decay paths. Since the radiation pattern of $\pi$-polarized light has no overlap with the $\mathrm{TEM}_{00}$ mode along the quantization axis, the $\pi$-polarized photons can be filtered out by collecting the emitted light in a single mode fiber. The resultant entangled ion state then becomes $\frac{1}{\sqrt{2}}|\sigma^- \uparrow\rangle + \frac{1}{\sqrt{2}}|\sigma^+ \downarrow\rangle$. This scheme is illustrated in Fig. 9.1.

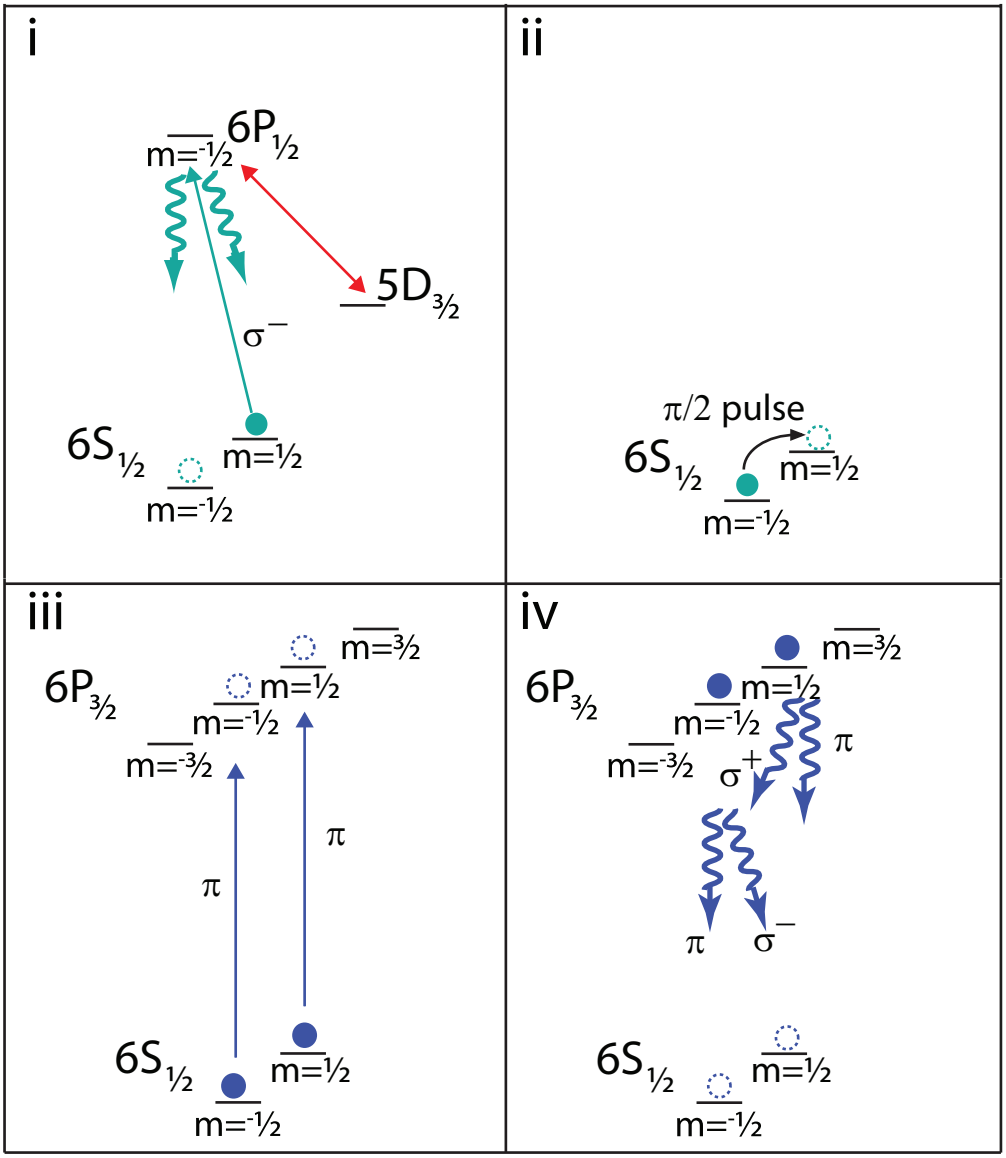


Figure 9.1: The ion is initialized by optical pumping (step i), followed by a $\pi/2$ pulse (step ii) to create an equal superposition of the ground state sublevels. The ion is excited by a single $\pi$-polarized ultrafast pulse (step iii). Finally the spontaneous emission of a photon in one of the four possible decay paths (step iv) creates the state $\Psi = \frac{1}{2}|\sigma^- \uparrow\rangle + \frac{1}{2}|\pi \uparrow\rangle + \frac{1}{2}|\sigma^+ \downarrow\rangle + \frac{1}{2}|\pi \downarrow\rangle$. The $\pi$-polarization may be filtered out by coupling the light into a single mode fiber resulting in the entangled state $\frac{1}{\sqrt{2}}|\sigma^- \uparrow\rangle + \frac{1}{\sqrt{2}}|\sigma^+ \downarrow\rangle$.

### *9.2 Effects of Polarization Mixing on Fidelity*

To determine the feasibility of demonstrating a loophole free Bell Inequality violation with this entanglement scheme, it is essential to determine the effects of the polarization mixing due to the large solid angle of light collection on the fidelity of the entangled state. I will begin by assuming that for the density matrix elements in Eq. 8.5, theoretically $\rho_{11} = \rho_{44} = \rho'_{11} = \rho'_{44}$ and $\rho_{22} = \rho_{33} = \rho'_{22} = \rho'_{33}$ with perfect rotation for an equal superposition state as we have here. Thus Eq. 8.5 can be simplified to $F \geq 2(\rho_{11} - \rho_{22}) = 2(P(\uparrow)P(\mathrm{S}|\uparrow) - P(\downarrow)P(\mathrm{S}|\downarrow))$. From Eq. 9.1, $P(\uparrow) = P(\downarrow) = \frac{1}{2}$, thus

$$F \geq P(\mathrm{S}|\uparrow) - P(\mathrm{S}|\downarrow) \tag{9.2}$$

.

To determine $P(\mathrm{S}|\uparrow)$ and $P(\mathrm{S}|\downarrow)$, I will use Jones calculus formalism. Each of the polarization vectors in spherical coordinates is as follows:

$$|\sigma^+\rangle = \frac{e^{i\phi}}{\sqrt{2}}(\cos\theta|\hat{\theta}\rangle + i|\hat{\phi}\rangle) \tag{9.3}$$

$$|\pi\rangle = -\sin\theta|\hat{\theta}\rangle \tag{9.4}$$

$$|\sigma^-\rangle = \frac{e^{-i\phi}}{\sqrt{2}}(\cos\theta|\hat{\theta}\rangle - i|\hat{\phi}\rangle) \tag{9.5}$$

Assuming that ion is positioned at the focus of the parabolic mirror, upon reflection any light polarized in the spherical $\hat{\theta}$-direction and $\hat{\phi}$-direction will be polarized in the cylindrical $\hat{\mathbf{r}}$-direction and $\hat{\theta}$-direction respectively. This is depicted in figure 9.2. For the purposes of the Jones calculus, I convert the polarization vectors from Eqs. 9.3-9.5 to rectangular coordinates and find the normalized polarization vectors to be:

$$|\sigma^+\rangle = \frac{e^{i\phi}}{\sqrt{1+\cos^2\theta}}((\cos\theta\cos\phi - i\sin\phi)|\hat{\mathbf{x}}\rangle + (\cos\theta\sin\phi + i\cos\phi)|\hat{\mathbf{y}}\rangle) \tag{9.6}$$

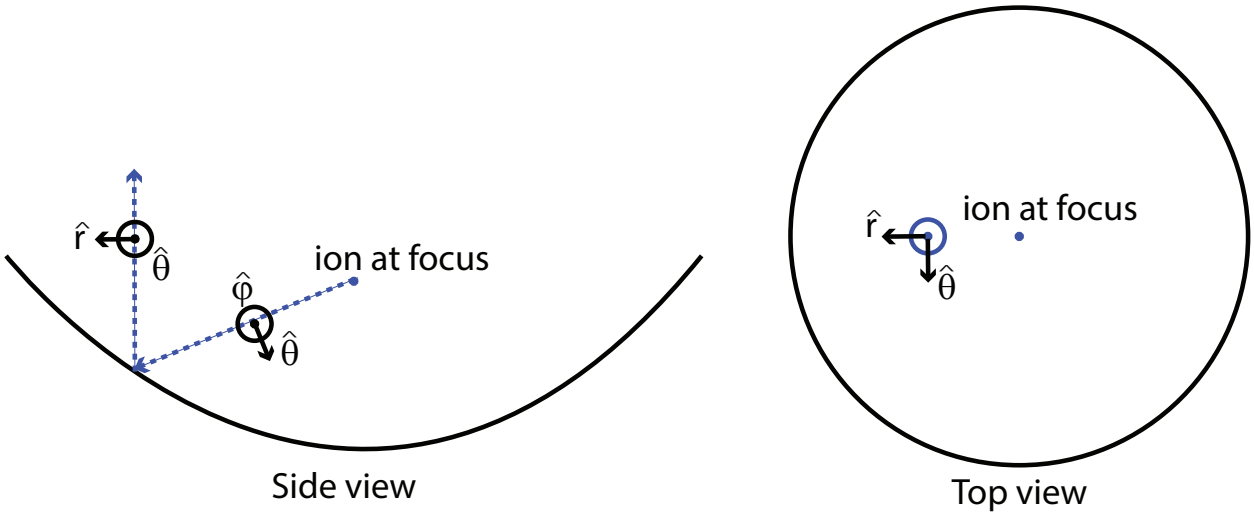


Figure 9.2: A side and top view of the polarization upon reflection off the parabolic mirror. Polarization in the spherical $\hat{\theta}$ and $\hat{\phi}$ directions become the cylindrical $\hat{r}$ and $\hat{\theta}$ directions respectively.

$$|\pi\rangle = -\cos\phi|\hat{\mathbf{x}}\rangle - \sin\phi|\hat{\mathbf{y}}\rangle \tag{9.7}$$

$$|\sigma^-\rangle = \frac{e^{-i\phi}}{\sqrt{1+\cos^2\theta}}((\cos\theta\cos\phi + i\sin\phi)|\hat{\mathbf{x}}\rangle + (\cos\theta\sin\phi - i\cos\phi)|\hat{\mathbf{y}}\rangle) \tag{9.8}$$

To measure the polarization state of each emitted photon, the collected light will be passed through a $\lambda/4$ waveplate followed by a polarizing beam splitter. Thus to calculate the probability that a particular emitted polarization state is measured to have S polarization by the polarizing beam splitter, one must find the absolute square of the coefficient for the resulting normalized eigenstate of the operator corresponding to the polarizer in the following equation:

$$\frac{1}{2}\begin{bmatrix}1 & 1\\ 1 & 1\end{bmatrix}\begin{bmatrix}1 & 0\\ 0 & i\end{bmatrix}|p\rangle = c\begin{bmatrix}\frac{1}{\sqrt{2}}\\ \frac{1}{\sqrt{2}}\end{bmatrix} \tag{9.9}$$

where $|p\rangle$ is the particular polarization state, $\begin{bmatrix} 1 & 0 \\ 0 & i \end{bmatrix}$ is the operator corresponding to the $\lambda/4$ waveplate, $\frac{1}{2}\begin{bmatrix} 1 & 1 \\ 1 & 1 \end{bmatrix}$ is the operator corresponding to the polarizer, and $c$ is the coefficient of interest. Thus one finds the probabilities that the emitted polarization state is measured to have S polarization by the polarizing beam splitter to be:

$$\text{for } \sigma^+: \quad P(\text{S}) = \frac{1}{2} - \frac{\cos\theta}{1+\cos^2\theta} \tag{9.10}$$

$$\text{for } \pi: \quad P(\text{S}) = \frac{1}{2} \tag{9.11}$$

$$\text{for } \sigma^-: \quad P(\text{S}) = \frac{1}{2} + \frac{\cos\theta}{1-\cos^2\theta} \tag{9.12}$$

Now to determine $P(\text{S}|\uparrow)$ and $P(\text{S}|\downarrow)$, one must find a weighted sum of the probabilities in Eqs. 9.10-9.12 based on the angular distribution of the radiation pattern for each polarization, where the angular distribution of $\sigma^\pm$ and $\pi$-polarized light are $\propto 1+\cos^2\theta$ and $\sin^2\theta$ respectively. Since only $\sigma^-$ and $\pi$-polarized photons are measured when the ion is measured to be in state $|\uparrow\rangle$ and only $\sigma^+$ and $\pi$-polarized photons when the ion is measured to be in state $|\downarrow\rangle$, the probabilities of measuring S polarization are as follows:

$$P(\text{S}|\uparrow) = \frac{\int \frac{3}{16\pi}(1+\cos^2\theta)\left(\frac{1}{2}+\frac{\cos\theta}{1+\cos^2\theta}\right)d\Omega + \int \frac{3}{8\pi}\sin^2\theta\frac{1}{2}d\Omega}{\int \frac{3}{16\pi}(1+\cos^2\theta)d\Omega + \int \frac{3}{8\pi}\sin^2\theta d\Omega} \tag{9.13}$$

$$P(\text{S}|\downarrow) = \frac{\int \frac{3}{16\pi}(1+\cos^2\theta)\left(\frac{1}{2}-\frac{\cos\theta}{1+\cos^2\theta}\right)d\Omega + \int \frac{3}{8\pi}\sin^2\theta\frac{1}{2}d\Omega}{\int \frac{3}{16\pi}(1+\cos^2\theta)d\Omega + \int \frac{3}{8\pi}\sin^2\theta d\Omega} \tag{9.14}$$

If the $\pi$-polarized light is filtered out by coupling the emitted photons into a single-mode fiber, then the probabilities of measuring S polarization become:

$$P(\text{S}|\uparrow) = \frac{\int \frac{3}{16\pi}(1+\cos^2\theta)\left(\frac{1}{2}+\frac{\cos\theta}{1+\cos^2\theta}\right)d\Omega}{\int \frac{3}{16\pi}(1+\cos^2\theta)d\Omega} \tag{9.15}$$

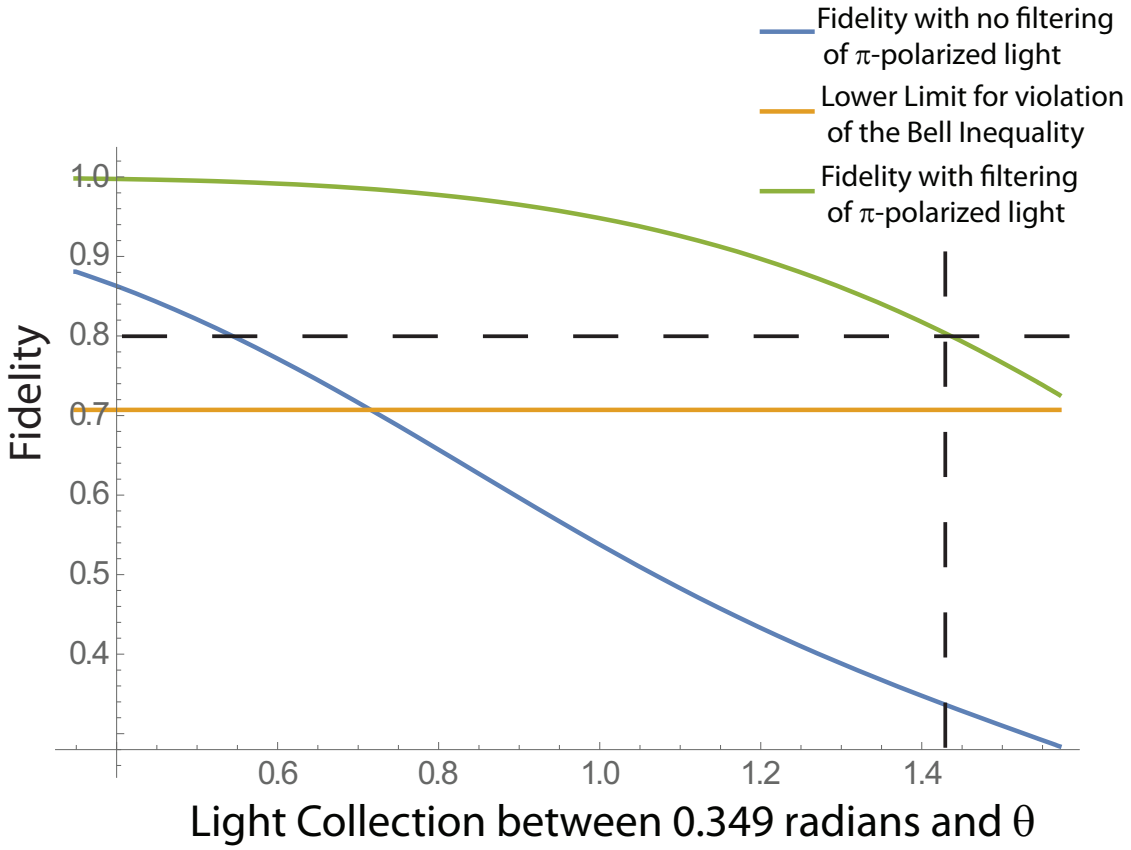


Figure 9.3: As can be seen from the graph above, the fidelity decreases quickly as the amount of light collected increases when the $\pi$-polarized light is not filtered by coupling into a single-mode fiber. In order to demonstrate a violation of the Bell Inequality, the lower limit of the fidelity is $1/\sqrt{2} = .707$. The dashed lines show that we expect the fidelity $F \approx 0.80$ for the maximum collection we have achieved from the parabolic mirror (corresponding to $\approx 40\%$ light collection efficiency).

$$P(\mathrm{S}|\downarrow) = \frac{\int \frac{3}{16\pi}(1+\cos^2\theta)\left(\frac{1}{2} - \frac{\cos\theta}{1+\cos^2\theta}\right)d\Omega}{\int \frac{3}{16\pi}(1+\cos^2\theta)d\Omega} \tag{9.16}$$

Thus fidelity may be calculated from Eq. 9.2 using the expressions found in Eqs. 9.13-9.16 for both when the $\pi$-polarized photons are not filtered and filtered by coupling into a single mode fiber. Fig. 9.3 shows the fidelity versus $\theta$ where $\theta = 0$ corresponds to an emitted photon direction of travel toward the center of the parabolic mirror and all light between

0.349 radians and $\theta$ is collected (this accounts for the fact that the needle will scatter any photons emitted between $\theta = 0$ and $\theta = .349$). As can be seen, it is essential for a Bell Inequality violation utilizing a large solid angle of light collection that the $\pi$-polarized light is filtered out by coupling into a single-mode fiber.

### *9.3 Ion-Photon Correlations*

Initial measurements of ion-photon correlations were made using the entanglement scheme described in section 9.1. After optically pumping to one of the ground state sublevels, an RF resonant $\pi/2$-pulse was applied to coherently transfer the ion state to an equal superposition of the ground state sublevels. The ion was then excited by a single 455 nm pulse from the ultrafast laser which had $\approx 20 - 40\%$ excitation probability. Laser pointing fluctuation and reduction in power necessary to eliminate the continuous wave (CW) component limited the excitation probability. The spontaneously emitted photon was fiber coupled into a single mode fiber to filter $\pi$-polarized light. At the output of the fiber a $\lambda/4$ waveplate converted the circularly polarized light into linearly polarized light and a $\lambda/2$ waveplate was used to rotate the photon state. The 0 angle of the $\lambda/2$ waveplate was set at $45^\circ$ to the fast/slow axis of the $\lambda/4$ waveplate. The light then passed through a PBS and a single photon count was detected on either of the two PMTs. The ion state was measured by applying a Rabi $\pi$-pulse with the 1762 nm shelving laser to shelve one of the two ground state Zeeman sublevels and then detecting fluorescence from the ion with the application of the cooling laser.

The data shown in Fig. 9.4 for the correlations at each $\lambda/2$ setting is an average of 3 sets of 100 runs. The contrast of $\approx 0.7$ in these initial correlations is less than the expected contrast of $\approx 0.8$ (based on the calculations and graph from section 9.2) and is likely limited by the optical pumping and shelving efficiency in addition to the expected reduction due to polarization mixing. Utilizing ARP for detection of the ion state would be expected to increase the contrast in order to compare with the expected value as it is a more robust method for ion state transfer to the shelved state since it is insensitive to laser frequency

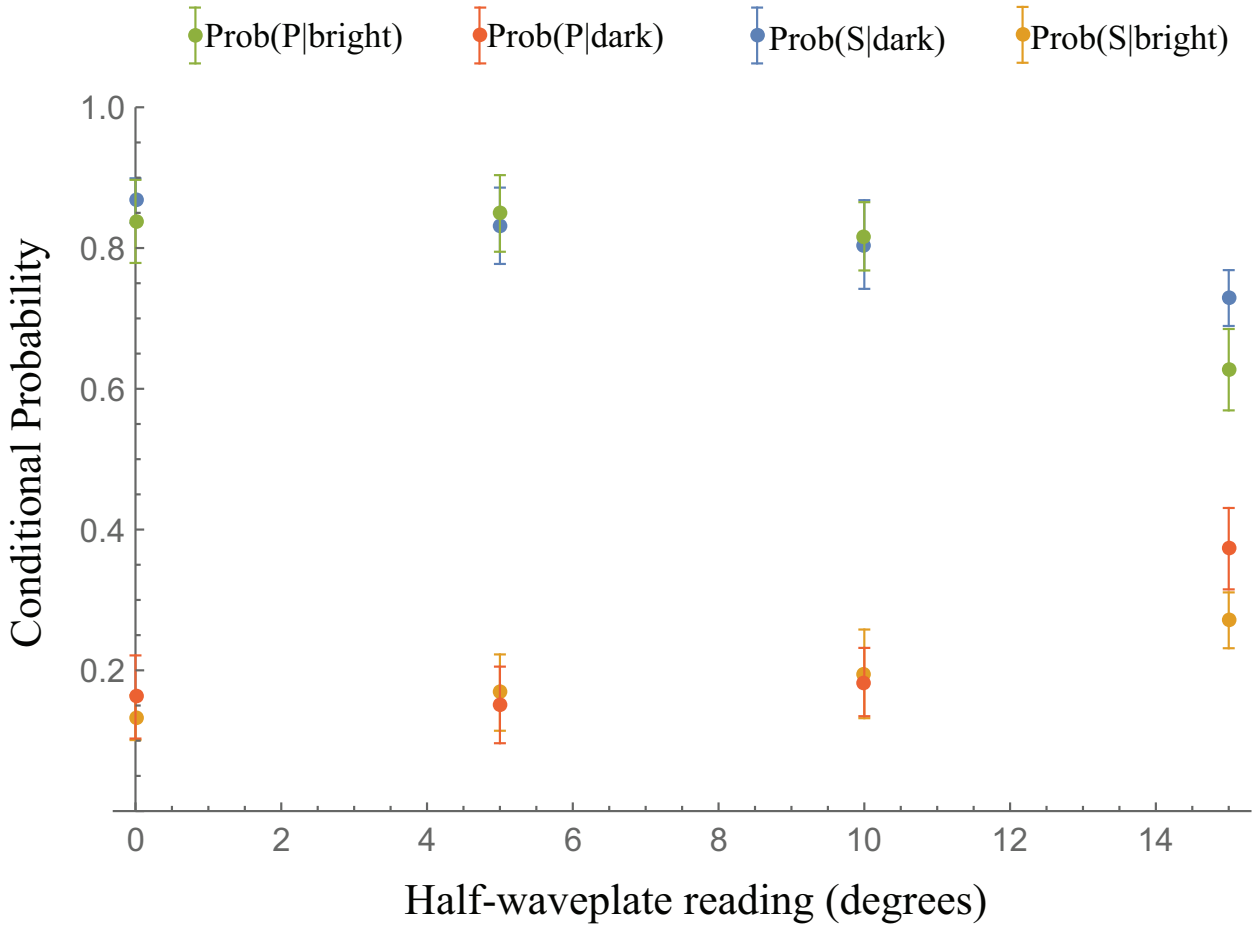


Figure 9.4: Measured conditional probabilities $P$(P|bright), $P$(P|dark), $P$(S|dark), and $P$(S|bright) as a function of the photon qubit measurement basis angle by rotating the half-waveplate while leaving the ion qubit unrotated.

and intensity, magnetic field drifts, and ion temperature. Further work is being done to demonstrate a Bell Inequality violation with the fiber coupled light from the parabolic mirror trap.

### *9.4 Loophole-Free Bell Inequality Test*

The ion-photon entanglement proposed here allows for the construction of a quantum network over a large distance. Especially interesting would be a loophole-free Bell inequality

test using photon mediated entanglement swapping between distant ion-photon entangled pairs proposed by Simon and Irvine [48]. $^{138}Ba^{+}$is especially suited for this due to the high fidelity of ion state detection and the relatively low attenuation of 455 nm light ($\leq$ 30 dB/km) over fiber optic cable compared to most other ion schemes. Highly efficient collection of photons from each ion would significantly increase the experimental rate of ion-ion entanglement generation. Using a parabolic mirror trap, our group has recently attained as much as 40% light collection efficiency from a single trapped ion [9]. For two ions separated by 1 km, there would be 3.3 $\mu$s in which to perform state rotation and detection. Currently we have demonstrated a minimum $\pi$-time of 0.70 $\mu$s for ion-state rotation and a minimum $\pi$-time of 5.0 $\mu$s for shelving with 1 mW of 1762 nm light. This time can be shortened by a combination of increasing the available laser power and achieving a tighter focus. Alternatively, it should also be possible to drive the shelving transition in hundreds of ns via a two photon Raman transition similar to [10]. Either approach leaves approximately 2 $\mu$s for fluorescence detection. In order to attain the 83% detection efficiency necessary to close the detection loophole, Poissonian statistics dictates that the detection time must be long enough to detect two photons on average from a bright ion. For our system, the maximum photon detection rate is given by the product of the maximum scattering rate ($\frac{\Gamma}{2} = 47.65$ MHz), the collection efficiency ($\frac{\Omega}{4\pi} = 0.4$), the photon detection efficiency ($\eta = 0.6$ for an avalanche photodiode [49]), and transmission through all optics ($T = 0.8$), which yields a maximum detection rate of 9 photons per $\mu$s and easily exceeds the 2 photons per 2 $\mu$s that we require.

In order to determine the entanglement generation rate, we need the success probability $P$ in a given trial and the experimental repetition rate, $R$. $P$ depends on the efficiency of generating a single photon from each ion and subsequently detecting the photons in coincidence. For the purposes of this estimation we assume unit excitation (possible with intense ultrafast pulses) from which barium's branching ratio for decay into the ground state is $f = 0.756$. The detection probability of each photon is given by the light collection solid angle $\frac{\Omega}{4\pi} = 0.4$,

fiber coupling efficiency $\xi = 0.8$ [32], transmission through other optical elements T=0.7, and the quantum efficiency of the detectors $\eta = 0.6$. Given the detection speed described above, our ions must be separated by roughly one kilometer, which can reasonably be connected by 1.2 km of fiber. This introduces an additional factor of $T_{fiber} = 10^{-3*1.2}$ to the entanglement rate. Finally, by detecting one of the four Bell states, our success probability would be $P = (1/4)[(\eta)(\xi)(f)(T)(P_{exc})(\frac{\Omega}{4\pi})]^2 T_{fiber} = (0.25)[(0.6)(0.8)(0.756)(0.7)(1)(0.4)]^2 * 10^{-3*1.2} = 6 * 10^{-7}$. With an experiment repetition rate of R=100 kHz, this would result in a heralded entanglement event approximately every 15 sec, certainly reasonable for a loophole-free Bell Inequality test.

# BIBLIOGRAPHY

[1] Markus Ansmann, H. Wang, Radoslaw C. Bialczak, Max Hofheinz, Erik Lucero, M. Neeley, A. D. O'Connell, D. Sank, M. Weides, J. Wenner, A. N. Cleland, and John M. Martinis. Violation of bell's inequality in josephson phase qubits. *Nature*, 461:504, Sep 2009.

[2] J. S. Bell. On the einstein podolsky rosen paradox. *Physics*, 1(3):195, Nov 1964.

[3] J. Benhelm, G. Kirchmair, C. Roos, and R. Blatt. Towards fault-tolerant quantum computing with trapped ions. *Nature Physics*, 4:463, Jun 2008.

[4] Charles H. Bennett, David P. DiVincenzo, John A. Smolin, and William K. Wootters. Mixed-state entanglement and quantum error correction. *Phys. Rev. A*, 54:3824–3851, Nov 1996.

[5] A. J. Berkley, H. Xu, R. C. Ramos, M. A. Gubrud, F. W. Strauch, P. R. Johnson, J. R. Anderson, A. J. Dragt, C. J. Lobb, and F. C. Wellstood. Entangled macroscopic quantum states in two superconducting qubits. *Science*, 300(5625):1548–1550, 2003.

[6] Hannes Bernien, Lilian Childress, Lucio Robledo, Matthew Markham, Daniel Twitchen, and Ronald Hanson. Two-photon quantum interference from separate nitrogen vacancy centers in diamond. *Phys. Rev. Lett.*, 108:043604, Jan 2012.

[7] B. B. Blinov, D. L. Moehring, L.-M. Duan, and C. Monroe. Observation of entanglement between a single trapped atom and a single photon. *Nature*, 428:153, Mar 2004.

[8] C. W. Chou, H. de Riedmatten, D. Felinto, S. V. Polyakov, J. van Enk, and H. J. Kimble. Measurement-induced entanglement for excitation stored in remote atomic ensembles. *Nature*, 438:828, Dec 2005.

[9] Chen-Kuan Chou, Gang Shu, Thomas Noel, John Wright, Richard Graham, and Boris Blinov. Trapping ions in a 2-pi parabolic mirror. *Bull. Am. Phys. Soc.*, 58:157, Jun 2013.

[10] Boon Leng Chuah, Nicholas C. Lewty, and Murray D. Barrett. State detection using coherent raman repumping and two-color raman transfers. *Phys. Rev. A*, 84:013411, Jul 2011.

[11] John F. Clauser, Michael A. Horne, Abner Shimony, and Richard A. Holt. Proposed experiment to test local hidden-variable theories. *Phys. Rev. Lett.*, 23:880–884, Oct 1969.

[12] Kristiaan De Greve, Leo Yu, Peter L. McMahon, Jason S. Pelc, Chandra M. Natarajan, Na Young Kim, Eisuke Abe, Sebastian Maier, Christian Schneider, Martin Kamp, Sven Hofling, Robert H. Hadfield, Alfred Forchel, M. M. Fejer, and Yoshihisa Yamamoto. Quantum-dot spin-photon entanglement via frequency downconversion to telecom wavelength. *Nature*, 491:421, Nov 2012.

[13] C. Eichler, C. Lang, J. M. Fink, J. Govenius, S. Filipp, and A. Wallraff. Observation of entanglement between itinerant microwave photons and a superconducting qubit. *Phys. Rev. Lett.*, 109:240501, Dec 2012.

[14] A. Einstein, B. Podolsky, and N. Rosen. Can quantum-mechanical description of physical reality be considered complete? *Phys. Rev.*, 47:777–780, May 1935.

[15] W. B. Gao, P. Fallahi, E. Togan, J. Miguel-Sanchez, and A. Imamoglu. Observation of entanglement between a quantum dot spin and a single photon. *Nature*, 491:426, Nov 2012.

[16] R. Gerritsma, G. Kirchmair, F. Zhringer, J. Benhelm, R. Blatt, and C. F. Roos. Precision measurement of the branching fractions of the 4p 2p3/2 decay of ca ii. *The European Physical Journal D*, 50(1):13–19, 2008.

[17] Marissa Giustina, Alexandra Mech, Sven Ramelow, Bernhard Wittmann, Johannes Kofler, Jorn Beyer, Adriana Lita, Brice Calkins, Thomas Gerrits, Sae Woo Nam, Rupert Ursin, and Anton Zeilinger. Bell violation using entangled photons without the fair-sampling assumption. *Nature*, 497:227, May 2013.

[18] Marissa Giustina, Marijn A. M. Versteegh, Sören Wengerowsky, Johannes Handsteiner, Armin Hochrainer, Kevin Phelan, Fabian Steinlechner, Johannes Kofler, Jan-Åke Larsson, Carlos Abellán, Waldimar Amaya, Valerio Pruneri, Morgan W. Mitchell, Jörn Beyer, Thomas Gerrits, Adriana E. Lita, Lynden K. Shalm, Sae Woo Nam, Thomas Scheidl, Rupert Ursin, Bernhard Wittmann, and Anton Zeilinger. Significant-loophole-free test of bell's theorem with entangled photons. *Phys. Rev. Lett.*, 115:250401, Dec 2015.

[19] C. Guet and W. R. Johnson. Erratum: Relativistic many-body calculations of transition rates for $ca^+$, $sr^+$, and $ba^+$ [phys. rev. a 44, 1531 (1991)]. *Phys. Rev. A*, 76:039905, Sep 2007.

[20] J. Gurell, E. Biémont, K. Blagoev, V. Fivet, P. Lundin, S. Mannervik, L.-O. Norlin, P. Quinet, D. Rostohar, P. Royen, and P. Schef. Laser-probing measurements and calculations of lifetimes of the $5d\,^2d_{32}$ and $5d\,^2d_{52}$ metastable levels in Ba *ii*. *Phys. Rev. A*, 75:052506, May 2007.

[21] D. Hanneke, S. Fogwell, and G. Gabrielse. New measurement of the electron magnetic moment and the fine structure constant. *Phys. Rev. Lett.*, 100:120801, Mar 2008.

[22] T. W. Hänsch and A. L. Schawlow. *Opt. Commun.*, 13:68, 1975.

[23] Yuji Hasegawa, Rudolf Loidl, Gerald Badurek, Matthias Baron, and Helmut Rauch. Violation of a bell-like inequality in single-neutron interferometry. *Nature*, 425:45, Sep 2003.

[24] Bernien H. Dreau A. E. Reiserer A. Kalb N. Blok M. S. Ruitenberg J. Vermeulen R. F. L. Schouten R. N. Abellan C. Amaya W. Pruneri V. Mitchell M. W. Markham M. Twitchen D. J. Elkouss D. Wehner S. Taminiau T. H. Hensen, B. and R. Hanson. Loophole-free bell inequality violation using electron spins separated by 1.3 kilometres. *Nature*, 526:682, Oct 2015.

[25] Gediminas Juska, Valeria Dimastrodonato, Lorenzo O. Mereni, Agnieszka Gocalinska, and Emanuele Pelucchi. Towards quantum-dot arrays of entangled photon emitters. *Nat Photon*, 7:527, Jul 2013.

[26] A. Kreuter, C. Becher, G. P. T. Lancaster, A. B. Mundt, C. Russo, H. Häffner, C. Roos, W. Hänsel, F. Schmidt-Kaler, R. Blatt, and M. S. Safronova. Experimental and theoretical study of the $3d\,^2d^{\smile}$level lifetimes of $^{40}Ca^+$. *Phys. Rev. A*, 71:032504, Mar 2005.

[27] N. Kurz, M. R. Dietrich, Gang Shu, R. Bowler, J. Salacka, V. Mirgon, and B. B. Blinov. Measurement of the branching ratio in the $6P_{32}$ decay of Ba II with a single trapped ion. *Phys. Rev. A*, 77:060501, Jun 2008.

[28] L. Li, Y. O. Dudin, and A. Kuzmich. Entanglement between light and an optical atomic excitation. *Nature*, 498:466, Jun 2013.

[29] A. A. Madej and J. D. Sankey. Quantum jumps and the single trapped barium ion: Determination of collisional quenching rates for the $5d^2D_{5/2}$ level. *Phys. Rev. A*, 41:2621–2630, Mar 1990.

[30] D. N. Matsukevich, P. Maunz, D. L. Moehring, S. Olmschenk, and C. Monroe. Bell inequality violation with two remote atomic qubits. *Phys. Rev. Lett.*, 100:150404, Apr 2008.

[31] D. L. Moehring, P. Maunz, S. Olmschenk, K. C. Younge, D. N. Matsukevich, L.-M. Duan, and C. Monroe. Entanglement of single-atom quantum bits at a distance. *Nature*, 449:68, Sep 2007.

[32] C. Monroe. Deparment of Physics, University of Maryland, 1117 John S. Toll Building 082, College Park, MD 20742, (personal communication, 2013).

[33] C. Monroe, R. Raussendorf, A. Ruthven, K. R. Brown, P. Maunz, L.-M. Duan, and J. Kim. Large scale modular quantum computer architecture with atomic memory and photonic interconnects. *pre-print*, 2012.

[34] C. Monroe, R. Raussendorf, A. Ruthven, K. R. Brown, P. Maunz, L.-M. Duan, and J. Kim. Large-scale modular quantum-computer architecture with atomic memory and photonic interconnects. *Phys. Rev. A*, 89:022317, Feb 2014.

[35] P. Neumann, N. Mizuochi, F. Rempp, P. Hemmer, H. Watanabe, S. Yamasaki, V. Jacques, T. Gaebel, F. Jelezko, and J. Wrachtrup. Multipartite entanglement among single spins in diamond. *Science*, 320(5881):1326–1329, 2008.

[36] Nilsson, H., Hartman, H., Engstrm, L., Lundberg, H., Sneden, C., Fivet, V., Palmeri, P., Quinet, P., and Bimont, . Transition probabilities of astrophysical interest in the niobium ions $nb^{+}$ and $nb^{2+}$. *A&A*, 511:A16, 2010.

[37] T. Noel, M. R. Dietrich, N. Kurz, G. Shu, J. Wright, and B. B. Blinov. Adiabatic passage in the presence of noise. *Phys. Rev. A*, 85:023401, Feb 2012.

[38] Chad Orzel. Searching for new physics through atomic, molecular and optical precision measurements. *Physica Scripta*, 86(6):068101, 2012.

[39] E. H. Pinnington, R. W. Berends, and M. Lumsden. Studies of laser-induced fluorescence in fast beams of sr+ and ba+ ions. *J. Phys. B.*, 28:2095, June 1995.

[40] Michael Ramm, Thaned Pruttivarasin, Mark Kokish, Ishan Talukdar, and Hartmut Häffner. Precision measurement method for branching fractions of excited $P_{1/2}$ states applied to $^{40}Ca^{+}$. *Phys. Rev. Lett.*, 111:023004, Jul 2013.

[41] T. Rosenband, D. B. Hume, P. O. Schmidt, C. W. Chou, A. Brusch, L. Lorini, W. H. Oskay, R. E. Drullinger, T. M. Fortier, J. E. Stalnaker, S. A. Diddams, W. C. Swann, N. R. Newbury, W. M. Itano, D. J. Wineland, and J. C. Bergquist. Frequency ratio of al+ and hg+ single-ion optical clocks; metrology at the 17th decimal place. *Science*, 319(5871):1808–1812, 2008.

[42] W. Rosenfeld, F. Hocke, F. Henkel, M. Krug, J. Volz, M. Weber, and H. Weinfurter. Towards long-distance atom-photon entanglement. *Phys. Rev. Lett.*, 101:260403, Dec 2008.

[43] M. A. Rowe, D. Kielpinski, V. Meyer, C. A. Sackett, W. M. Itano, C. Monroe, and D. J. Wineland. Experimental violation of a bell's inequality with efficient detection. *Nature*, 409:791, Feb 2001.

[44] C. A. Sackett, D. Kielpinski, B. E. King, C. Langer, V. Meyer, C. J. Myatt, M. Rowe, Q. A. Turchette, W. M. Itano, D. J. Wineland, and C. Monroe. Experimental entanglement of four particles. *Nature*, 404:256, Mar 2000.

[45] U.I. Safronova and M.S. Safronova. Excitation energies, e1, m1, and e2 transition rates, and lifetimes in ca+, sr+, cd+, ba+, and hg+1 1this article is part of a special issue on the 10th international colloquium on atomic spectra and oscillator strengths for astrophysical and laboratory plasmas. *Canadian Journal of Physics*, 89(4):465–472, 2011.

[46] B. K. Sahoo, Md. R. Islam, B. P. Das, R. K. Chaudhuri, and D. Mukherjee. Lifetimes of the metastable $^2d_{32,52}$ states in $ca^+$, $sr^+$, and $ba^+$. *Phys. Rev. A*, 74:062504, Dec 2006.

[47] Lynden K. Shalm, Evan Meyer-Scott, Bradley G. Christensen, Peter Bierhorst, Michael A. Wayne, Martin J. Stevens, Thomas Gerrits, Scott Glancy, Deny R. Hamel, Michael S. Allman, Kevin J. Coakley, Shellee D. Dyer, Carson Hodge, Adriana E. Lita, Varun B. Verma, Camilla Lambrocco, Edward Tortorici, Alan L. Migdall, Yanbao Zhang, Daniel R. Kumor, William H. Farr, Francesco Marsili, Matthew D. Shaw, Jeffrey A. Stern, Carlos Abellán, Waldimar Amaya, Valerio Pruneri, Thomas Jennewein, Morgan W. Mitchell, Paul G. Kwiat, Joshua C. Bienfang, Richard P. Mirin, Emanuel Knill, and Sae Woo Nam. Strong loophole-free test of local realism*. *Phys. Rev. Lett.*, 115:250402, Dec 2015.

[48] Christoph Simon and William T. M. Irvine. Robust long-distance entanglement and a loophole-free bell test with ions and photons. *Phys. Rev. Lett.*, 91:110405, Sep 2003.

[49] L. Slodička, G. Hétet, N. Röck, P. Schindler, M. Hennrich, and R. Blatt. Atom-atom entanglement by single-photon detection. *Phys. Rev. Lett.*, 110:083603, Feb 2013.

[50] I. I. Sobelman. *Introduction to the theory of atomic spectra*. Pergamon Press, Oxford, 1972.

[51] Matthias Steffen, M. Ansmann, Radoslaw C. Bialczak, N. Katz, Erik Lucero, R. McDermott, Matthew Neeley, E. M. Weig, A. N. Cleland, and John M. Martinis. Measurement of the entanglement of two superconducting qubits via state tomography. *Science*, 313(5792):1423–1425, 2006.

[52] A. Stute, B. Casabone, P. Schindler, T. Monz, P. O. Schmidt, B. Brandstatter, T. E. Northup, and R. Blatt. Tunable ion-photon entanglement in an optical cavity. *Nature*, 485:482, May 2012.

[53] P. Taylor, M. Roberts, S. V. Gateva-Kostova, R. B. M. Clarke, G. P. Barwood, W. R. C. Rowley, and P. Gill. Investigation of the $^2S_{1/2}-^2D_{5/2}$ clock transition in a single ytterbium ion. *Phys. Rev. A*, 56:2699–2704, Oct 1997.

[54] E. Togan, Y. Chu, A. S. Trifonov, L. Jiang, J. Maze, L. Childress, M. V. G. Dutt, A. S. Sorensen, P. R. Hemmer, A. S. Zibrov, and M. D. Lukin. Quantum entanglement between an optical photon and a solid-state spin qubit. *Nature*, 466:730, Aug 2010.

[55] Q. A. Turchette, Kielpinski, B. E. King, D. Leibfried, D. M. Meekhof, C. J. Myatt, M. A. Rowe, C. A. Sackett, C. S. Wood, W. M. Itano, C. Monroe, and D. J. Wineland. Heating of trapped ions from the quantum ground state. *Phys. Rev. A*, 61:063418, May 2000.

[56] G. Waldherr, P. Neumann, S. F. Huelga, F. Jelezko, and J. Wrachtrup. Violation of a temporal bell inequality for single spins in a diamond defect center. *Phys. Rev. Lett.*, 107:090401, Aug 2011.

[57] Philip Walther, Markus Aspelmeyer, Kevin J. Resch, and Anton Zeilinger. Experimental violation of a cluster state bell inequality. *Phys. Rev. Lett.*, 95:020403, Jul 2005.

[58] Gregor Weihs, Thomas Jennewein, Christoph Simon, Harald Weinfurter, and Anton Zeilinger. Violation of bell's inequality under strict einstein locality conditions. *Phys. Rev. Lett.*, 81:5039–5043, Dec 1998.

[59] T. Wilk, A. Gaëtan, C. Evellin, J. Wolters, Y. Miroshnychenko, P. Grangier, and A. Browaeys. Entanglement of two individual neutral atoms using rydberg blockade. *Phys. Rev. Lett.*, 104:010502, Jan 2010.

[60] D. J. Wineland and H. Dehmelt. Proposed 1014 dv<v laser fluorescence spectroscopy on tl+ mono-ion oscillator iii (side band cooling). *Bull. Am. Phys. Soc.*, 20:637, 1975.

[61] N. Yu, W. Nagourney, and H. Dehmelt. Radiative lifetime measurement of the $ba^+$ metastable $d_{3/2}$ state. *Phys. Rev. Lett.*, 78:4898–4901, Jun 1997.